3D Resistivity Surveys for Structural Investigations of the Shallow Subsurface at Sadao, Songkhla

Kraipat Petrit

A Thesis Submitted in Partial Fulfillment of the Requirements for the Degree of Master of Science in Geophysics

Prince of Songkla University

2018

3D Resistivity Surveys for Structural Investigations of the Shallow Subsurface at Sadao, Songkhla

Kraipat Petrit

A Thesis Submitted in Partial Fulfillment of the Requirements for the Degree of Master of Science in Geophysics

Prince of Songkla University

2018

Thesis Title	3D Resistivity Surveys for Structural Investigations of the Shallow Subsurface at Sadao, Songkhla
Author	Mr.Kraipat Petrit
Major Program	Geophysics

Major Advisor

……
(Asst. Prof. Dr. Helmut Dürrast)

Examining Committee:

…….Chairperson
(Dr. Boonyarit Chatthong)

……...Committee
(Assoc. Prof. Dr. Loke Meng Heng)

……...Committee
(Asst. Prof. Dr. Helmut Dürrast)

The Graduate School, Prince of Songkla University, has approved this thesis as partial fulfillment of the requirements for the Master of Science Degree in Geophysics

…….
(Prof. Dr. Damrongsak Faroongsarng)
Dean of Graduate School

This is to certify that the work here submitted is the result of the candidate's own investigations. Due acknowledgement has been made of any assistance received

.....Signature

(Asst. Prof. Dr. Helmut Dürrast)

Major Advisor

.....Signature

(Mr. Kraipat Petrit)

Candidate

I hereby certify that this work has not been accepted in substance for any degree, and is not being currently submitted in candidature for any degree

.....Signature

(Mr. Kraipat Petrit)

Candidate

ชื่อวิทยานิพนธ์ การสำรวจสภาพต้านทานไฟฟ้าแบบสามมิติเพื่อการศึกษาโครงสร้างใต้ผิวดินระดับตื้นในพื้นที่อำเภอสะเดา จังหวัดสงขลา

ผู้เขียน นายไกรพัฒน์ เพชรฤทธิ์

สาขาวิชา ธรณีฟิสิกส์

ปีการศึกษา 2560

บทคัดย่อ

ชั้นผิวดินระดับตื้นเป็นบริเวณที่มีความสำคัญอย่างมาก ทั้งได้รับและส่งผลต่อมนุษย์ในหลายด้าน รวมทั้งยังเป็นแหล่งของธรณีพิบัติอีกด้วย ดั้งนั้นการศึกษาโครงสร้างชั้นผิวดินระดับตื้น อย่างเช่น ชั้นหินตะกอน และแนวรอยเลื่อน จึงมีส่วนสำคัญเป็นอย่างมาก การสำรวจสภาพต้านทานไฟฟ้าเป็นวิธีการสำรวจทางธรณีฟิสิกส์ที่ใช้อย่างแพร่หลายในการสำรวจชั้นผิวดินระดับตื้น โดยมีวัตถุประสงค์คือการศึกษาการกระจายตัวของค่าสภาพต้านทานไฟฟ้า เพื่อทำความเข้าใจโครงสร้างใต้ผิวดิน ประเภทของการสำรวจสภาพต้านทานไฟฟ้าเมื่อแบ่งตามมิติที่ใช้ในการสำรวจแล้วมีดังนี้ การสำรวจสภาพต้านทานไฟฟ้าแบบหนึ่งมิติ ใช้ในการศึกษาค่าสภาพต้านทานไฟฟ้าที่เปลี่ยนแปลงตามความลึก การสำรวจสภาพต้านทานไฟฟ้าแบบสองมิติ เป็นการศึกษาการกระจายตัวของค่าสภาพต้านทานไฟฟ้าในแนวราบและแนวดิ่ง และการสำรวจสภาพต้านทานไฟฟ้าแบบสามมิติ เป็นการศึกษาการกระจายตัวของค่าสภาพต้านทานไฟฟ้าในภาคตัดขวางทั้งในแนวราบและแนวดิ่ง วัตถุประสงค์สำหรับงานวิจัยนี้ คือการพัฒนาระบบเก็บข้อมูลสภาพต้านทานไฟฟ้าแบบสามมิติ โดยให้สามารถปรับใช้กับเครื่องมือที่มีอยู่แล้วได้ และให้มีความเหมาะสมในด้านเวลาที่ใช้ในการเก็บข้อมูลอีกด้วย พื้นที่ศึกษาสำหรับงานวิจัยตั้งอยู่ในบริเวณเหมืองดินเก่า ซึ่งสามารถมองเห็นและศึกษาชั้นดินตะกอนและแนวรอยเลื่อนได้จากพื้นดิน พื้นที่การเก็บข้อมูลถูกแบ่งเป็นสามพื้นที่ ซึ่งถูกออกแบบให้ครอบคลุมแนวรอยเลื่อนที่สำรวจพบจากผิวดิน แต่ละพื้นที่ใช้ขั้วไฟฟ้าในการวัด 100 ขั้ว จัดเรียงแบบจัตุรัส 10×10 ระยะห่างระหว่างขั้วไฟฟ้าคือ 3 เมตร และใช้รูปแบบการวางขั้วแบบไดโพล-ไดโพล ข้อมูลที่ได้จากการสำรวจจะถูกประมวลผลโดยโปรแกรม Res3DInv ผลการสำรวจถูกแสดงในรูปแบบการกระจายตัวของค่าสภาพต้านทานไฟฟ้าในภาคตัดขวางแนวราบ และภาคตัดขวางแนวดิ่ง ความลึกจากการสำรวจประมาณ 8 ม. ผลการสำรวจแสดงให้เห็นถึงแนวการวางตัวของชั้นหินตะกอน และแนวรอยเลื่อนใต้ผิวดิน ซึ่งสอดคล้องกับข้อมูลทางธรณีวิทยา โดยสรุปแล้ว การสำรวจสภาพต้านทานไฟฟ้าแบบสามมิติมีศักยภาพในการศึกษาโครงสร้างทางธรณีวิทยาใต้ผิวดิน สามารถทำให้ศึกษาและตีความข้อมูลเชิงลึกของโครงสร้างใต้ผิวดินได้มากขึ้น

Thesis Title	3D Resistivity Surveys for Structural Investigations of the Shallow Subsurface at Sadao, Songkhla
Author	Kraipat Petrit
Major Program	Geophysics
Academic year	2017

Abstract

The shallow subsurface is subject to various human activities, and the place of occurrence of geohazards, e.g. shallow active faults. The identification of the shallow subsurface structure such as sedimentary layers and faults can be vital for infrastructure development. Resistivity survey is one type of geophysical method, which is widely used for shallow subsurface investigations. General objectives of resistivity surveys are to study the distribution of resistivity values in the subsurface to identify and understand subsurface structures. There are many types of resistivity surveys classified by survey dimensions: 1D vertical electrical sounding (VES) is mainly for studying changes of resistivity in vertical direction; 2D electrical resistivity tomography (ERT) is for studying the distribution of resistivity values in horizontal and vertical directions; whereas 3D resistivity survey is for studying the distribution of resistivity values in horizontal sections and along vertical directions. The aim of this study was to develop a low-cost 3D resistivity survey system, with reasonable survey time for shallow subsurface investigations. The study area is in Songkhla Province, Thailand, located in an old quarry where faults could be identified in outcrops. The study area consists of Area 1, Area 2 and Area 3. All three areas were designed to cover the expected faults. For each area, 100 electrodes arranged in a 10×10 square grid with an electrode spacing of 3 meters along x- and y-axis. Each electrode in turn was used as a current and potential electrode using a dipole-dipole array. Field data have been processed and interpreted using Res3DINV. Results, presented in horizontal depth slices and vertical xz- and yz-cross sections, revealed through differences in resistivity down to 8 m depths a complex structural setting with four shallow faults and dipping sedimentary rock layers. In conclusion, this study has shown that a 3D resistivity survey can image complex tectonic structures, thus providing a far more insight into the shallow subsurface.

ACKNOWLEDGEMENT

The work in this thesis has been an inspiring, often exiting, sometimes challenging, but always an interesting experience. I would deeply thank my advisor, Asst. Prof. Dr. Helmut Dürrast for continuous support, advice, encouragement, and patience during this study.

I would like to thank the Science Achievement Scholarship of Thailand (SAST) for financial support. Part of the field work was supported by Graduate School and the Department of Physics, both at Prince of Songkla University.

I would like to thank my friends in Geophysics and Physics Program for their help during the field work. Finally, I am deeply grateful to my family for their moral support and their encouragement during a challenging time.

Kraipat Petrit

CONTENTS

CONTENT	PAGE
ABSTRACT (IN THAI)	v
ABSTRACT (IN ENGLISH)	vi
ACKNOWLEDGEMENTS	vii
CONTENTS	viii
LIST OF TABLE	x
LIST OF FIGURE	xi
Chapter 1 Introduction	**1**
1.1 Introduction	1
1.1.1 Importance and benefit	1
1.1.2 Objective	1
1.1.3 Expected outcome	1
1.2 Literature review	1
1.2.1 Resistivity method	1
1.2.2 Basic theory	2
1.2.3 Resistivity of rocks	6
1.2.4 Sensitive function and depth of investigation	7
1.2.5 Array types for resistivity survey	12
1.2.6 3D Resistivity survey	17
1.2.7 4D Resistivity survey (time-lapse survey)	21
1.2.8 Sedimentary and sedimentary rock	22
1.2.9 Rock deformations	24
1.3 Applications of various types of resistivity survey	27
Chapter 2 Research methodology	32
2.1 Equipment preparation	32
2.1.1 Switch box	32
2.1.2 Cable assembly	33
2.1.3 Equipment set up and measuring	34
2.2 Testing of acquisition system	35
2.2.1 Measuring on testing area	35
2.2.2 Data processing	36
2.3 Study area	37
2.3.1 Location of study area	37
2.3.2 Structural geology in study area	38
2.4 Geological structure survey	39
2.4.1 Equipment	39
2.4.2 Surveying	39

CONTENTS (CONTINUED)

CONTENT	PAGE
2.5 Resistivity survey	40
2.5.1 Survey design	40
2.5.2 Data acquisition	41
Chapter 3 Results	**43**
3.1 Testing result	43
3.1.1 7×7 square grid with spacing 2 m	43
3.1.2 10×10 square grid with spacing 2 m	43
3.1.3 10×10 square grid with spacing 3 m	44
3.2 Results from study area	47
3.2.1 Area 1	47
3.2.2 Area 2	49
3.2.3 Area 3	49
Chapter 4 Discussion and Conclusions	**52**
4.1 Discussions	52
4.1.1 Sedimentary layering	52
4.1.2 Faults	52
4.1.3 Comparison between geology and resistivity data	55
4.1.4 Compare to large scale of geological structure (Hat Yai Basin)	57
4.1.5 Forward Modeling	58
4.1.6 Error of inversion results	61
4.2 Conclusions	61
4.2.1 Modeling of geological structure	61
4.2.2 Data acquisition system	62
REFFERENCES	65
APPENDIX	69
Appendix A: Raw data	70
Appendix B: Publication	90
VITAE	99

LIST OF TABLES

TABLE		PAGE
1.1	Parameters and properties of geophysical methods	2
1.2	The median depth of investigation (Ze) for the different arrays. Parameter "a" is electrode spacing and "L" total length of the array	11
1.3	Classification detrital sediments and rocks	23
2.1	Equipment list for 3D resistivity survey	32
2.2	Data input format used to input into RES3DINV software.	36
2.3	Location and information of geological survey in study area.	39
2.4	Corner location for each square grid	41
4.1	Dip direction and dip angle of sedimentary layer boundary	55
4.2	Dip direction and dip angle of fault lines	55

LIST OF FIGURES

Figure		Page
1.1	Parameters used in defining resistivity	3
1.2	Current flows radially away from the electrode	3
1.3	Current flow from electrode A to electrode B and potential electrodes between M and N	4
1.4	Arrangement of electrodes give different geometric factors	5
1.5	Resistivity range of rock, mineral and some chemical materials	7
1.6	Parameters for the sensitivity function calculation at a point (x, y, z) within a half-space	8
1.7	Plot of the 1-D sensitivity function. (a) Sensitivity function for the Pole-Pole array. (b) The sensitivity function and median depth of investigation for the Wenner array. Blue arrow is maximum sensitivity and Red arrow is median depth of investigation	9
1.8	Set of Wenner array with sensitivity plotting contour	12
1.9	Set of array with sensitivity plotting contour for the dipole-dipole array. The sections with n=1, n=4 and n=6	13
1.10	Set of array with sensitivity plotting contour for the Wenner-Schlumberger array. Sections here are for n=1, n=4, and n=6	14
1.11	Sensitivity plot contours for pole-pole array	15
1.12	Wenner-Schlumberger array sensitivity plots for n=1, 4, and 6	16
1.13	Horizontal coverage of each array (a) Wenner, (b) Pole-pole, (c) Dipole-dipole	16
1.14	Simple arrangements of the electrodes for a 3-D survey	18
1.15	Two possible measurement sequences for 3-D surveys. The location of potential electrodes corresponding to a single current electrode in the arrangement used by (a) a survey to measure the complete data set and (b) a cross-diagonal survey	18
1.16	3D sensitivity plots of pole-pole array. Plots shown in horizontal slices at different depths	19
1.17	Example of dipole–dipole configurations oriented along x and y directions or inter cardinal directions x-y and x+y	20
1.18	3D sensitivity plots of dipole-dipole array with n=1 in horizontal slices at different depths	20
1.19	3D sensitivity plots for dipole-dipole array with n=4 in the horizontal slices at different depths	21
1.20	Resistivity ratio method used for interpretation of 4D ERT	22

LIST OF FIGURES (CONTINUED)

Figure		Page
1.21	Processes of detrital sedimentary rocks made up from solid particles while chemical sedimentary rocks consist of interlocking mosaics of crystals derived from dissolved compounds	24
1.22	1.22 Type of applied stress on rocks (A) and Type of rock deformation under difference condition (B)	25
1.23	Major types of fault, (A) normal fault, (B) reverse fault, and (C) strike-slip	26
1.24	Depiction of the strike and dip of some tilted sedimentary beds partially covered with water. The notation for expressing strike and dip on a map is shown	26
1.25	(a) Arrangement of survey lines measured in x and y direction building up the measurement grid. (b) 3D model obtained from the inversion of the survey data set	28
1.26	1.26 (a) 3D resistivity model used to simulate the filling material and the tombs that are buried inside the tumulus. (b) Forward model using pole-dipole array	29
1.27	27 Inversion model from field work, investigated by pole-dipole array	29
1.28	Resistivity responds after the rainfall shown as the percentage change of resistivity	30
1.29	Horizontal depth slices of 3D profile investigated on karst structure	31
2.1	Diagram of switch box and sequent of cable moving of dipole-dipole array, Black is current electrode C1 and C2, Red is potential electrode P1 and P2	33
2.2	Cable assembly consists of ten single cables assembled together	33
2.3	Example of equipment setup, consist of resistivity meter, connecting cables, switch box, cable assembly and 12V battery	34
2.4	Overview map of testing area at Faculty of Science courtyard, Prince of Songkla University	35
2.5	Study area (a) Location of study area in northern part of Sadao district, Songkhla province, southern Thailand, (b) Boundaries of the survey area with the direction of the x-axis 50 degrees from north over west, (c) Square grid of 10×10 electrodes with x-, y- and z-direction, and (d) Equipment set up consisting of resistivity meter, 12 V battery, switch box, and cable assembly	37

LIST OF FIGURES (CONTINUED)

Figure		Page
2.6	Geology map of Songkhla province in southern part	38
2.7	Surface condition of study area	38
2.8	Structural geology of study area (a) Fault, looking into NW, dip direction/dip angle of the fault plane is 222/64 and of the sedimentary layering 333/20, (b) Study area, looking into SE, (c) Sedimentary layer in the quarry nearby the study area, looking into SE, and measurement of sedimentary layering is 310/18, (d) Sedimentary layering seen at the cliff locate in the southern part of the study area, (e) Fault, looking into SE, with an orientation of 222/64, and (f) Sedimentary layering near the study area, looking into NW; measurement of layering plane gives 288/15	40
2.9	Resistivity survey square grids; there is one electrode spacing (3 m) overlap in between Area 1-Area 2 and Area 2-Aare 3	41
2.10	Survey design and equipment (a) Diagram of equipment set up consisting of 100 electrodes arranged in a 10×10 square grid, cable, switch box (1), resistivity meter (2) and 12 V battery (3), (b) Arrangement of electrodes in dipole-dipole array, C1-C2 is current electrode pair, P1-P2 is potential electrode pair, a is 3 m inline spacing and n is the ratio varied from 1 to 7 for 10 nodes of electrodes, and (c) Measurement lines, x, y, and both diagonal directions	42
3.1	Horizontal section result of 7×7 grid with spacing 2 m on testing area	44
3.2	X-section result of 7×7 grid with spacing 2 m on testing area	44
3.3	Y-section result of 7×7 grid with spacing 2 m on testing area	44
3.4	Horizontal section result of 10×10 grid with spacing 2 m on testing area	45
3.5	X-section result of 10×10 grid with spacing 2 m on testing area	45
3.6	Y-section result of 10×10 grid with spacing 2 m on testing area	45
3.7	Horizontal section result of 10×10 grid with spacing 3 m on testing area	46
3.8	X-section result of 10×10 grid with spacing 3 m on testing area	46
3.9	Y-section result of 10×10 grid with spacing 3 m on testing area	46
3.10	Horizontal section result of 10×10 grid with spacing 3 m on Area 1	48

LIST OF FIGURES (CONTINUED)

Figure		Page
3.11	X-section result of 10×10 grid with spacing 3 m on Area 1	48
3.12	Y-section result of 10×10 grid with spacing 3 m on Area 1	48
3.13	Horizontal section result of 10×10 grid with spacing 3 m on Area 2	50
3.14	X-section result of 10×10 grid with spacing 3 m on Area 2.	50
3.15	Y-section result of 10×10 grid with spacing 3 m on Area 2	50
3.16	Horizontal section result of 10×10 grid with spacing 3 m on Area 3	51
3.17	X-section result of 10×10 grid with spacing 3 m on Area 3	51
3.18	Y-section result of 10×10 grid with spacing 3 m on Area 3	51
4.1	Resistivity range is separated into three zones. Low resistivity area (L) with resistivity values varying from 20 to 200 ohm-m, indicated by blue colors. A medium resistivity area (M) that has a resistivity range of 200 to 1,500 ohm-m, indicated by green and yellow colors, and a high resistivity area with resistivity value varying from 1,500 to 5,000 Ohm-m	53
4.2-1	Horizontal section result Layer 1, 2, and 3. Black solid lines are fault lines and dotted lines are sedimentary layers	53
4.2-2	Horizontal section result Layer 4, 5, and 6. Black solid lines are fault lines and dotted lines are sedimentary layers	54
4.3	X-section result of section 1 to 9. Black solid lines are fault lines and dotted lines are sedimentary layers	54
4.4	Y-section results of section 1 to 9. Black lines are fault lines and dotted lines are sedimentary layers	55
4.5	Data correlation between geological and resistivity: Low resistivity is siltstone mixed with sandstone, medium resistivity is sandstone, and high resistivity is conglomerate	56
4.6	Overview map of the study area including geological information and resistivity data	56
4.7	Geological structure of Hat Yai basin with horst and graben, A; Bouguer anomaly contour map in $\mu m/s^2$, B; and C shows the information of sedimentary layers and faults in the study area	57
4.8	4.8 Procedures of forward modeling, consisting of making a resistivity model, calculate apparent resistivity, and export file to operate with inversion software	58

LIST OF FIGURES (CONTINUED)

Figure		Page
4.9	(A) resistivity model of two dipping layers; (B) inversion results displayed in horizontal section; (C) inversion result displayed in x-section, and (D) inversion result displayed in y-section	59
4.10	(A) resistivity model of two dipping layers including one fault; (B) inversion result displayed in horizontal section; (C) inversion result displayed in x-section, and (D) inversion result displayed in y-section	60
4.11	Comparison between surface conditions and first layer of horizontal resistivity result.	62
4.12	Co-interpretation between resistivity data and geological data (a), and (b) identification of sedimentary layers and faults from resistivity results, (c) resistivity range including geological information, and (d) model of subsurface structure in study area	63
4.13	Resistivity model of the study area including information of sedimentary layers and faults, sedimentary layers indicated by black strike-dip symbols and faults indicated by red strike-dip symbols	64

CHAPTER 1

INTRODUCTION

1.1 Introduction

1.1.1 Importance and benefit

The shallow subsurface is the uppermost layer beneath Earth's surface (few hundred meters) and mainly consists of sediment materials and soil. This area effected and impacted by human activities such as building foundations, excavating, tunneling, waste site, landfill and exploitation of groundwater resources. Geophysical methods are used to find the best location (subsurface structure) that fit with the purpose on the surface because of many reasons, e.g. geophysics is cheaper than drilling/excavation, it can cover large areas faster and can penetrate deeper than drilling/excavation. Various types of geophysical method were used to investigate the shallow subsurface for different objectives, for example, seismic survey to estimate shear wave velocity, magnetic survey to find buried targets, ground penetrating radar survey to detect cable or tunnel and electrical survey to find groundwater. This work focuses on shallow subsurface investigation by using resistivity survey. Electrical surveys are mostly carried out at area with higher water or moisture content to study and determine the distribution of resistivity in the subsurface.

1.1.2 Objective

The objective of this work is to develop a fully functioning system for 3D resistivity measurements using the available technology at the department. Then the system and the data processing will be tested using data from a site with known subsurface environment.

1.1.3 Expected outcome

After finishing this project, it is expected that with the equipment at hand a fully functioning 3D measurement system will be available, demonstrated by test measurements and an application of the system at a real study site.

1.2 Literature review

1.2.1 Resistivity method

Geophysics methods apply physics' principles combined with physical properties of Earth material to study the inside of the Earth. During geophysical surveys measurements are taken usually on the Earth surface, thus revealing changes in selected physical properties with depth, vertically, and along survey lines, horizontally (Kearey et al., 2002).

Currently, various types of geophysical methods are established, which can be used to determine changes in different physical properties (Table 1.1). The type of physical property relates to the appropriate technique used and also determines the range of that method. For example, magnetic methods are suitable for locating buried bodies comprising of magnetite ore because of the minerals high magnetic susceptibility. In a similar way, seismic or electrical methods are favorable in determining the location of groundwater and water table because saturated rocks can be distinguished from not saturated, dry rocks by their higher seismic velocities and lower electrical resistivity values (Kearey et al., 2002).

The main objective of electrical surveys is to determine the distribution of the subsurface resistivity with measurements done on the surface. From these data, the true resistivity of the subsurface, e.g. different layers can be determined. The resistivity of a layer depends on various geological parameters, e.g. mineral and fluid composition, porosity, and the degree of water saturation. Because of that electrical resistivity surveys have been applied for many 10^{th} of years in hydrogeological, mining, environmental, and geotechnical investigations (Loke, 2000).

Table 1.1 Parameters and properties of geophysical methods (Kearey et al., 2002).

Method	**Measured parameter**	**Operative physical property**
Seismic	Travel times of reflected/refracted seismic waves	Density and elastic moduli, which determine the propagation velocity of seismic waves
Gravity	Spatial variations in the strength of the gravitational field of the Earth	Density
Magnetic	Spatial variations in the strength of the geomagnetic field	Magnetic susceptibility
Electrical		
Resistivity	Earth resistance	Electrical conductivity
Induce Potential	Polarization voltages	Electrical capacitance
Self-Potential	Electrical potentials	Electrical conductivity

1.2.2 Basic theory

The resistivity of an Earth material is defined as the resistance in ohms between the opposite faces of a geometrical shaped sample holder filled with that material. For a conducting cylindrical shaped container of resistance dR, with length dL and cross-sectional area dA (Figure 1.1) the resistivity ρ is given as following

$$\rho = \frac{\mathrm{dRdA}}{\mathrm{dL}} \quad \text{..... (1)}$$

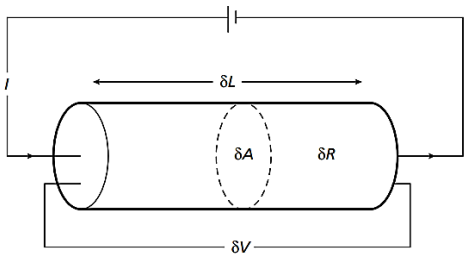

Figure 1.1 Parameters used in defining resistivity (Kearey et al., 2002).

Considering a body of homogeneous material as shown in Figure 1.1 (e.g. Kearey et al., 2002) a current (I) passed through the cylinder resulting in a potential drop -dV between the ends of the cylinder. Ohm's law relates the current, potential difference and resistance such that –dV = dRI and from Equation 2 the potential gradient (dV/dL) is given by

$$\frac{\mathrm{dV}}{\mathrm{dL}} = -\frac{\rho \mathrm{I}}{\mathrm{dA}} = -\rho \mathrm{J} \quad \text{..... (2)}$$

where dV/dL represents the potential gradient through the cylinder in Vm^{-1} and J is the current density in Am^{-2}. The current density in any direction within a material is therefore given by the negative partial derivative of the potential in that particular direction divided by the resistivity (Kearey et al., 2002).

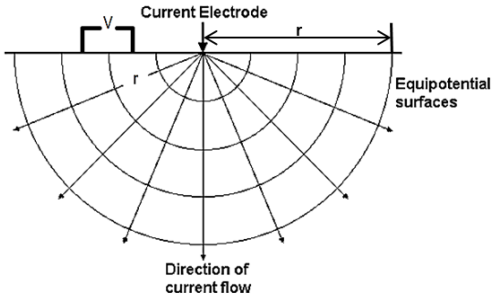

Figure 1.2 Current flows radially away from the electrode (Loke, 2000).

When considering a single current electrode on the surface of an Earth of uniform resistivity (Figure 1.2) the circuit is completed by a current sink at a further distance from the electrode. Current flows in a radial direction away from the electrode so that the current distribution is uniform over hemispherical shells that are centered on the current source (Kearey et al., 2002). At a distance R from the electrode the surface area of this shell is $2\pi r^2$, so the current density J is given by

$$\mathrm{J} = \frac{\mathrm{I}}{2\pi \mathrm{r}^2} \quad \text{..... (3)}$$

From Equation 3, the potential gradient associated with this current density is

$$\frac{dV}{dr} = -\rho J = \frac{-\rho I}{2\pi r^2} \quad \text{..... (4)}$$

The potential V_R at distance r is then obtained by integration (e.g. Kearey et al., 2002)

$$V_r = \int_r^\infty dV = -\int_r^\infty \frac{\rho I}{2\pi r^2} dr = \frac{\rho I}{2\pi r} \quad \text{..... (5)}$$

Equation 5 allows the calculation of the potential at any point on or below the surface of a homogeneous half space (Kearey et al., 2002). The hemispherical shells in Figure 1.2 mark a surface of constant voltage; they are named equipotential surfaces.When a current sink is at a finite distance from the source (Figure 1.3) the potential V_M at an internal electrode M is the sum of the potential contributions V_A and V_B from the current source at A and B, the electrical current flow from A to B+ (Kearey et al., 2002).

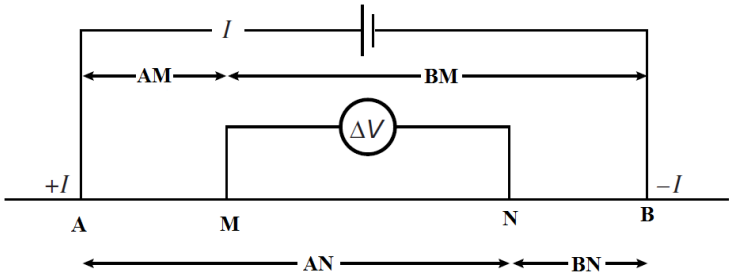

Figure 1.3 Current flow from electrode A to electrode B and potential electrodes between M and N (Loke, 2000).

$$V_M = V_{AM} + V_{BM} \quad \text{..... (6)}$$

From Equation 5

$$V_M = \frac{\rho I}{2\pi}\left(\frac{1}{AM} - \frac{1}{BM}\right) \quad \text{..... (7)}$$

Similarly

$$V_N = \frac{\rho I}{2\pi}\left(\frac{1}{AN} - \frac{1}{BN}\right) \quad \text{..... (8)}$$

Now ΔV (V_{MN}) can be calculated by

$$\Delta V = V_M - V_N = \frac{\rho I}{2\pi}\left(\frac{1}{AM} - \frac{1}{BM} - \frac{1}{AN} + \frac{1}{BN}\right) \quad \text{..... (9)}$$

Thus

$$\rho = \frac{dV}{I}\left(\frac{2\pi}{\frac{1}{AM} - \frac{1}{BM} - \frac{1}{AN} + \frac{1}{BN}}\right) = k\frac{V}{I} \quad \text{..... (10)}$$

where k is the geometric factor which depends on the surface arrangement, here distance from each other, of the four electrodes (Kearey et al., 2002). Resistivity meters normally give a resistance value, R = V/I. In practice the apparent resistivity value (resistivity of inhomogeneous materials) is then calculated by

$$\rho_a = kR \quad \text{..... (11)}$$

Figure 1.4 shows some common array arrangements used in resistivity surveys as well as their related geometric factors (Kearey et al., 2002).

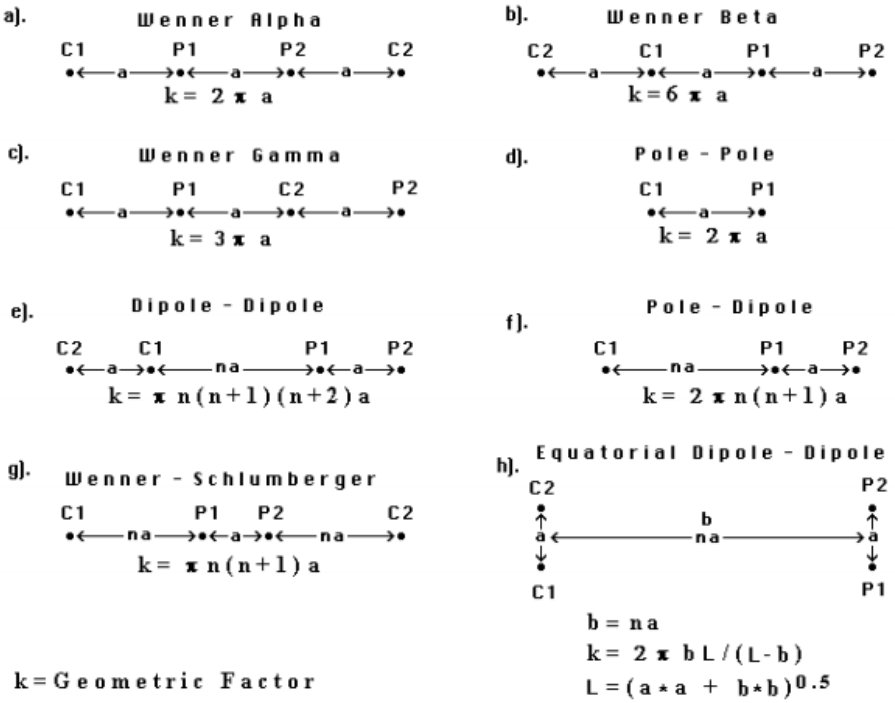

Figure 1.4 Arrangement of electrodes give different geometric factors (Loke, 2000).

Resistivity values calculated from the measured values are not true resistivity values of the subsurface layer; they are rather "apparent" values (Kearey et al., 2002). Apparent resistivity is the resistivity of a homogeneous Earth which will give the same resistance values for the same electrode arrangements. The relationship between "apparent" and "true" resistivity is quite complex (Kearey et al., 2002). To determine

the true subsurface resistivity distribution, an inversion of the measured apparent resistivity values using a computer program has to be done (Loke, 2000).

1.2.3 Resistivity of rocks

Resistivity of rocks depends on many parameters, e.g. porosity, permeability, type of pore fluid and mechanism of electrical conductivity of mineral and rock. These factors affect the resistivity of the rock that can vary in a large range as show in Figure 1.5.

Porosity

When describing porous media, porosity is the most important rock property. It is the ratio of pore volume to bulk volume of a rock or sediment sample. Porosity is a dimensionless quantity, and it can be written either in decimal or percentage. Fluid inside the pore can be the oil, gas, or water. Therefore, a primary application of porosity is to quantify the storage capacity of the rock, and subsequently define the volume of hydrocarbons available to be produced (Bowen, 1986).

Permeability

The permeability of a rock is a measure of the ease with which the rock will permit the passage of fluids. If it takes a lot of pressure to squeeze fluid through a rock, that rock has low permeability. A high permeability rock is found when a fluid passes through a rock easily. The unit of permeability is "Darcy", which is the passage of one cm^3 of fluid of one centipoises viscosity in one second under a pressure gradient of one atm/sec, across an area of one cm^2 of porous substance (Schön, 1996).

Electrical conductivity of minerals and rocks

There are three types of the electrical conductivity mechanisms in sediments and rocks, (1) electronic conduction in metal minerals, (2) ionic conduction in pore fluids of porous rocks or sediments, and (3) colloidal conduction in clay minerals (Kearey et al., 2002). Electronic conduction occurs mainly in metallic minerals and graphite. In metals electrons are the charge carriers which can move free through the crystalline lattice of such minerals. In comparison to rocks, sediments, and soils the conductivities are very high (Schön, 1996). Ionic conduction occurred in most rocks, sediments, and soils where the current is carried by ions, cations and anions, in the pore fluid. The value of the resistivity depends on various rock properties; porosity (inter-granular and fracture), pore fluid resistivity (salinity), temperature, pore fluid saturation, clay content pressure and the computation of bulk resistivity as a function of porosity, pore fluid salinity and temperature (Schön, 1996). In clay containing soil, the electrical charges located at the surface of the clay particles lead to greater electrical conductivity than in coarse-textured soils because of the magnitude of the specific surface. Whereas the electrical resistivity in sands and gravels without clay

occurs primarily in fluids filling the pores, in clays the electrical conduction occurs in the pores and on the surfaces of electrically charged clay particles, so called colloidal conductivity (Schön, 1996).

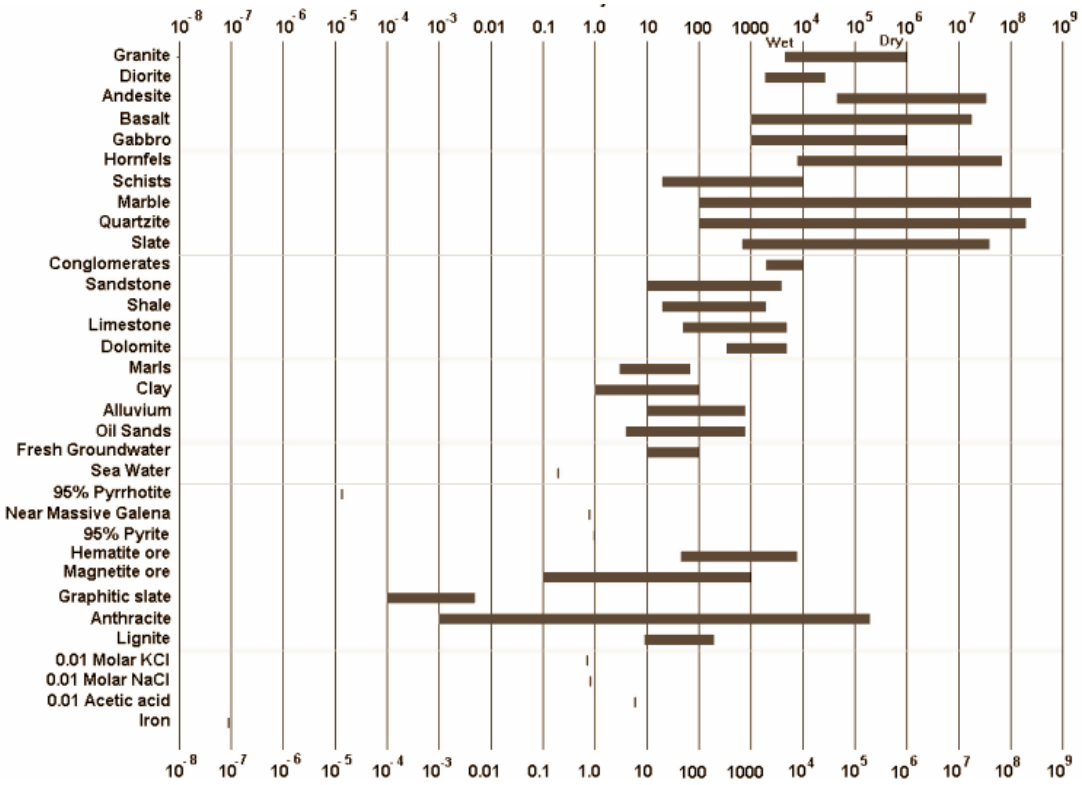

Figure 1.5 Resistivity range of rock, mineral and some chemical materials (from Loke, 2015).

1.2.4 Sensitive function and depth of investigation

For plotting data from a 2D imaging survey, the pseudosection contouring method is usually used. In such case, the horizontal locations of data are placed at the mid-point of the set of electrodes, which are placed to make the measurement. The vertical location is plotted at the median depth of investigation, so called pseudodepth; this depends on the electrode array. This pseudodepth is based on the sensitivity function (Loke, 2015).

The sensitivity function basically is the degree to which a change in the resistivity of a section of the subsurface will influence the potential measured by the array. Mathematically, the sensitivity function is given by the Frechet derivative for a homogeneous half-space. A simple array configuration displayed in Figure 1.6. One current electrode is located at the origin (0,0,0) and one potential electrode at (a,0,0), and it is approximated that is electrode spacing a. One Ampere of electric current was passed into the ground through the C1 current electrode that results in a potential "Ø"

observed at the P1 potential electrode. The resistivity changes within a small volume of the Earth located at (x,y,z) by a small amount (δρ). The potential "δØ" measured at P1 is given by

$$\delta\emptyset = \frac{\delta\rho}{\rho^2}\int \nabla\emptyset \cdot \nabla\emptyset' d\tau \quad \text{..... (12)}$$

where the change the resistivity is a constant value for a small volume element dτ and it is of zero value elsewhere. The parameter Ø' is the potential, which comes from a current electrode which is positioned at the potential electrode P1 (Loke, 2015).

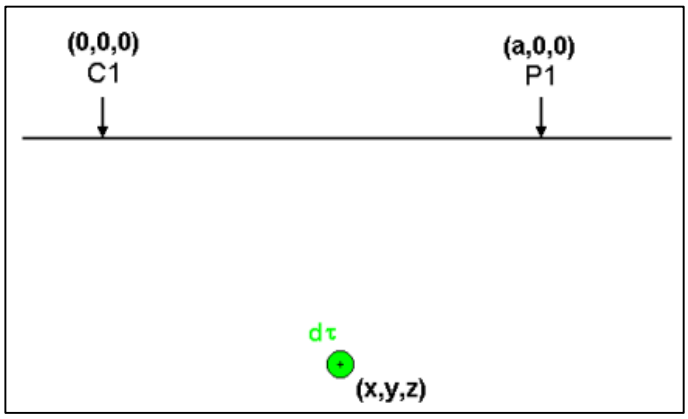

Figure 1.6 Parameters for the calculation of the sensitivity function at a point (x, y, z) within a half-space of the Earth (from Loke, 2015).

From the equation above we get

$$\frac{\delta\emptyset}{\delta\rho} = \int \frac{1}{4\pi^2} \cdot \frac{x(x-a)+y^2+z^2}{[X^2+y^2+z^2]^{1.5}[(x-a)^2+y^2+z^2]^{1.5}} dxdydz \quad \text{..... (13)}$$

The 3D Frechet derivative is then shown by following term within the integral

$$F_{3D}(x,y,z) = \frac{1}{4\pi^2} \cdot \frac{x(x-a)+y^2+z^2}{[x^2+y^2+z^2]^{1.5}[(x-a)^2+y^2+z^2]^{1.5}} \quad \text{..... (14)}$$

Equation 14 shows for a pole-pole configuration the Frechet derivative or sensitivity function. This consists of a current and a potential electrode. To get the Frechet derivative for a general four electrode configuration contributions were added from two current–potential pairs (Loke, 2015). The depth of investigation can be determined by 1D sensitive function. In resistivity sounding (1D resistivity survey), the subsurface is assumed to consist of horizontal layers of different thickness. For a horizontal layer, x and y limits of the layer extends from -∞ to +∞. Therefore, the

sensitivity function for a horizontal layer is obtained by integrating the 3D sensitivity function (Loke, 2015). It can be rewritten as following

$$F_{1D}(z) = \frac{1}{4\pi^2}\int_{-\infty}^{+\infty}\int_{-\infty}^{+\infty}\frac{x(x-a)+y^2+z^2}{[x^2+y^2+z^2]^{1.5}[(x-a)^2+y^2+z^2]^{1.5}}\,dxdy \quad \text{..... (15)}$$

The above equation has a simple analytical solution, which is given by

$$F_{1D}(z) = \frac{2}{\pi}\cdot\frac{z}{(a^2+4z^2)^{1.5}} \quad \text{..... (16)}$$

Equation 16 is also termed the depth investigation characteristic. It has been applied by many authors to investigate properties of various array types in resistivity sounding surveys (see Loke, 2015). The vertical location of plotted data point is located on the "median depth of investigation". The depth at the half of the total area under the curve, which is the area under the curve above this depth, is equal to the area under the curve below this depth (Figure 1.7, Loke, 2015).

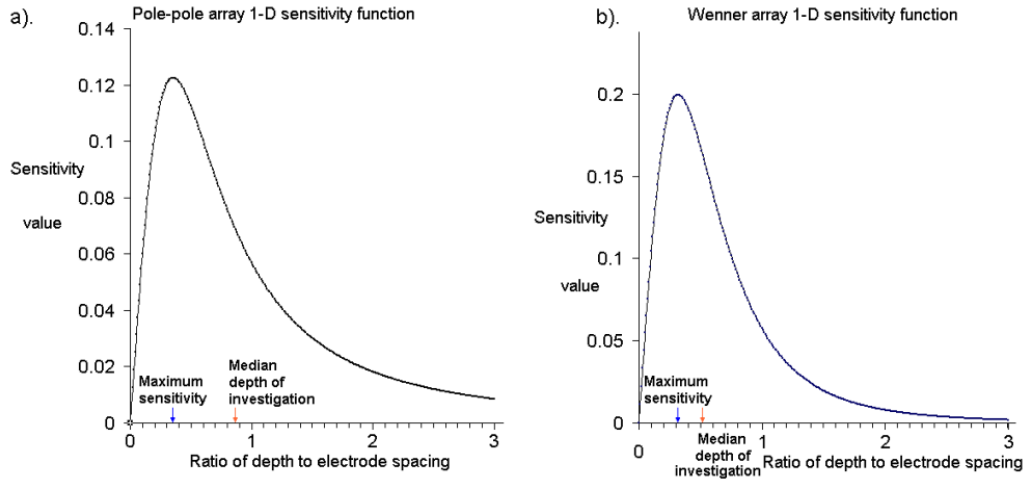

Figure 1.7 Plot of the 1-D sensitivity function. (a) Pole-Pole array sensitivity function. (b) Wenner array sensitivity function and median depth of investigation. Blue arrow is maximum sensitivity and Red arrow is median depth of investigation (from Loke, 2015).

Sensitivity functions for other arrays can be determined by adding up the contributions from the two pairs of the arranged current and potential electrodes. In Figure 1.7 the sensitivity function plot for a pole-pole array and a Wenner array is shown. The curve shape around the maximum value is narrower for Wenner array in comparsion with a pole-pole array. This suggests that the Wenner array has a preferred vertical resolution than the pole-pole array. Table 1.2 presents the median depth of investigation for these different arrays. To find the maximum depth measured by a particular survey type, the

maximum “a” electrode spacing, or maximum array length “L“, has to multiplied by the appropriate depth factor given in Table 1.2 (Loke, 2015).
For the 2D sensitivity function, particular for (x, z) location, all measurements have to be added up from all points for the y-values ranging from -∞ to +∞. This involves the integration of the 3D sensitivity function with respect to y, which is

$$F_{2D}(x,z) = \frac{1}{4\pi^2}\int_{-\infty}^{+\infty} \frac{x(x-a)+y^2+z^2}{[x^2+y^2+z^2]^{1.5}[(x-a)^2+y^2+z^2]^{1.5}}\,dy \quad \text{..... (17)}$$

This integral has an analytic solution that is presented in terms of elliptic integrals. The complete solution for this is

$$F_{2D}(x,z) = \frac{2}{\alpha\beta^2}\left[\frac{\alpha^2E(k)-\beta^2K(k)}{(\alpha^2-\beta^2)} - \frac{\gamma[(\alpha^2-\beta^2)E(k)-2\beta^2K(k)]}{(\alpha^2-\beta^2)^2}\right] \quad \text{..... (18)}$$

where

$$k = \frac{(\alpha^2-\beta^2)^{0.5}}{\alpha}$$

The sensitivity function provides the degree to which a change in the resistivity values of a section of the subsurface Earth will influence the potential measured by a certain array. When the sensitivity function has a higher value, then the influence of the subsurface region on the measurement is greater. For arrays, the highest sensitivity values are usually found near the electrodes at the surface. At further distances from these electrodes the contour patterns for the different arrays are different. Differences in the contour patterns of the sensitivity function plots are used to explain the response of the different arrays to different types of structures (Loke, 2015).

Table 1.2 the median depth of investigation (Ze) for the different arrays. Parameter "a" is electrode spacing and "L" total length of the array (from Loke, 2015).

Array	**Ze/a**	**Ze/L**	**Geometric factor**
Wenner	0.519	0.173	6.2832
Dipole-dipole			
n=1	0.416	0.139	18.850
n=2	0.697	0.174	75.398
n=3	0.962	0.192	188.50
n=4	1.220	0.203	376.99
n=5	1.476	0.211	659.73
n=6	1.730	0.216	1055.6
Wenner - Schlumberger			
n=1	0.519	0.173	6.2832
n=2	0.925	0.186	18.850
n=3	1.318	0.189	37.699
n=4	1.706	0.190	62.832
n=5	2.093	0.190	94.248
n=6	2.478	0.191	131.95
n=7	2.863	0.191	175.93
n=8	3.247	0.191	226.19
n=9	3.632	0.191	282.74
n=10	4.015	0.191	345.58
Pole-dipole			
n=1	0.519	0.260	12.566
n=2	0.925	0.308	37.699
n=3	1.318	0.330	75.398
n=4	1.706	0.341	125.66
n=5	2.093	0.349	188.50
n=6	2.478	0.354	263.89
n=7	2.863	0.358	351.86
n=8	3.247	0.361	452.39
Pole-Pole	0.867		6.28319

1.2.5 Array types for resistivity survey

Wenner array

For the Wenner array the current electrode pair is located outside while the potential electrodes are located inside (Figure 1.8). Distance between four electrodes is the same length; called electrode spacing "a". The Wenner Alpha array sensitivity plot (Figure 1.8) has almost horizontal contours beneath the arrays center. Due to this distribution, the Wenner array has a relatively higher sensitive to vertical changes in the Earth resistivity below the arrays center point. But it is not so sensitive to changes in the horizontal direction of the subsurface resistivity. From Table 1.2, the depth of investigation of this is approximately 0.5 times the "a" spacing used. Compared to other arrays, the Wenner Alpha array has a moderate depth of investigation. Wenner array has the strongest signal strength compared with other arrays. This might be an important factor if the survey is carried in areas with high background noise. One disadvantage of this array is the relatively poor horizontal coverage for 2D surveys as the electrode spacing is increased (Figure 1.13, Loke, 2015).

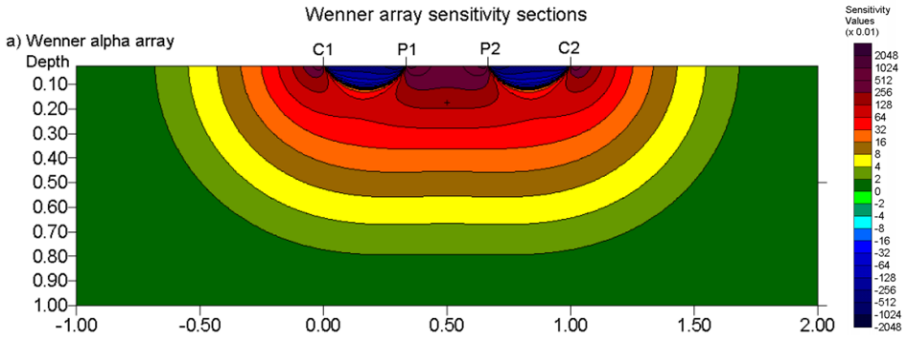

Figure 1.8 Set of Wenner array with sensitivity plotting contour (from Loke, 2015).

Dipole-dipole array

For Dipole-dipole array, the arrangement of this electrode is show in Figure 1.9, the spacing between the current electrodes pair, C2-C1, is given as "a" which is the same as the distance between the potential electrodes pair P1-P2 (Loke, 2015). The other factor this array is "n", ratio of the distance between the C1 and P1 electrodes to the C2-C1 (or P1-P2). For such arrangements the "a" spacing is initially kept unchanged at the smallest unit electrode spacing. The "n" factor is increasing from 1 to 2 to 3 until up to about 6 to get an increase in the depth of investigation. From the sensitivity plot in Figure 1.9 it can be seen that the highest sensitivity values are generally found between the dipole pair C2-C1and also between the P1-P2 pair. From that it can be seen that this array is most sensitive to changes in resistivity below the electrodes in each dipole pair. The sensitivity contour pattern becomes almost vertical for "n" values greater than a value of 2. Thus the dipole-dipole array is very sensitive to horizontal changes in resistivity values. However, it is relatively insensitive to vertical

resistivity changes. Because of this this array is preferred in mapping vertical structures, e.g. dykes and cavities. The median depth of investigation of this array depends on both the "a" spacing and the "n" factor. In general, this array has a shallower depth of investigation compared to the Wenner array. From field surveys, the median depth of investigation might underestimate the depth of structures measured by such array for large "n" factors by a value of about 20-30%. For 2D surveys, this array here is advantageous in terms of horizontal data coverage in comparison to the Wenner array (Loke, 2012). However, a possible disadvantage is the very low signal strength for large values of "n" factor. For the same current, the resistivity meters measured voltage drops by about 56 times when "n" increased from 1 to a value of 6 (Loke, 2015).

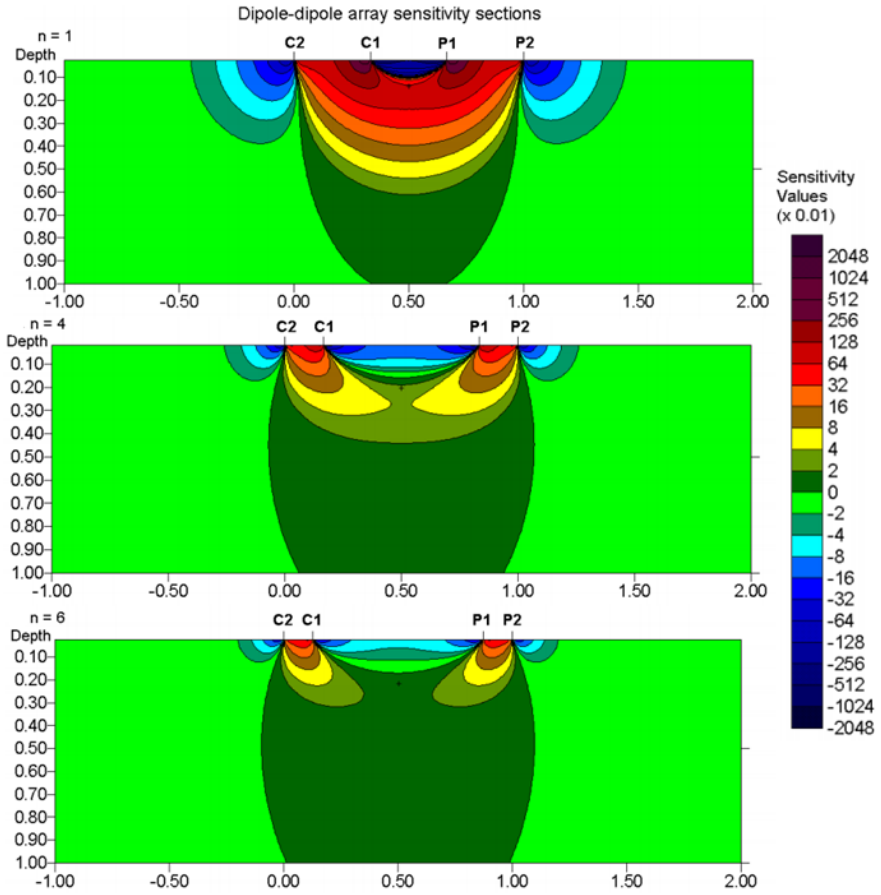

Figure 1.9 Set of array with sensitivity plotting contour for the dipole-dipole array. The sections with n=1, n=4 and n=6 (from Loke, 2015).

Wenner-Schumberger array

This is a hybrid between the Wenner and Schlumberger arrays arising out of electrical imaging surveys with multi-electrode systems (Figure 1.10). The "n" factor for this array can be expressed as the ratio of the distance between electrodes C1-P1 (or P2-

C2) to the spacing between the P1-P2 potential electrode pair. From the sensitivity plot in Figure 1.10 the area of highest positive sensitivity below the arrays center gets more concentrated beneath the central P1-P2 electrodes as the "n" factor increased (Loke, 2015).

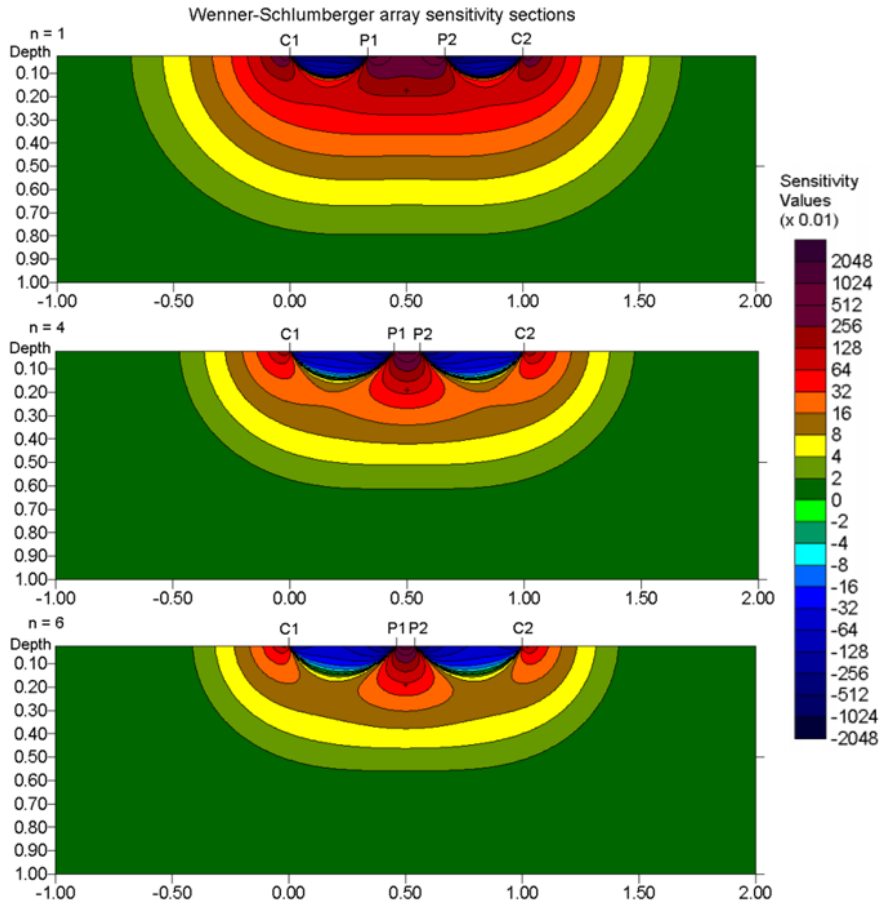

Figure 1.10 Set of array with sensitivity plotting contour for the Wenner-Schlumberger array. Sections here are for n=1, n=4, and n=6 (from Loke, 2015).

Close to the location of the plotting point of the median value of the depth of investigation, the sensitivity contour lines show a slight vertical curvature in the area below the center of the array. At n=6, a high positive sensitivity part beneath electrodes P1-P2 becomes more disconnected from high positive sensitivity values near electrodes C1 and C2 (Loke, 2015). This shows that this array is moderately sensitive to both, horizontal (low "n" values) as well as vertical structures (high "n" values). Median depth of investigation is about 10% larger for this array than for the Wenner array using the same distance between the C1 and C2 electrodes for values of "n" greater than 3. Further, signal strength is lower than for Wenner array, but it is higher compared to dipole-dipole array and twice of the pole-dipole value (Loke, 2015).

Pole-pole array

The pole-pole array is done with one current and one potential electrode (Loke, 2012; Figure 1.11). The second current and potential electrodes C2 and P2 are then placed at a distance which is more than 20 times the maximum of the separation between C1 and P1 electrodes used in the survey. If effects of C2 and P2 electrodes are not considered, the distance of these electrodes from the survey line must be at least 20 times the largest C1-P1 spacing to keep the error value less than 5%. This array has a disadvantage. Because of the large distance between the P1 and P2 electrodes, a survey with this array can measures a large amount of telluric noise that can decrease the quality of the measurements significantly. Therefore this array is often applied in investigations where relatively small electrode spacing (less than a few meters) can be used. It is quite accepted in certain applications such as archaeological surveys where small electrode spacing is feasible. This array exhibits the largest horizontal coverage and has the deepest depth of investigation. However, it has a poor resolution, which is related to the comparatively large spacing between the contours in the sensitivity function plot shown in Figure 1.11 (Loke, 2012).

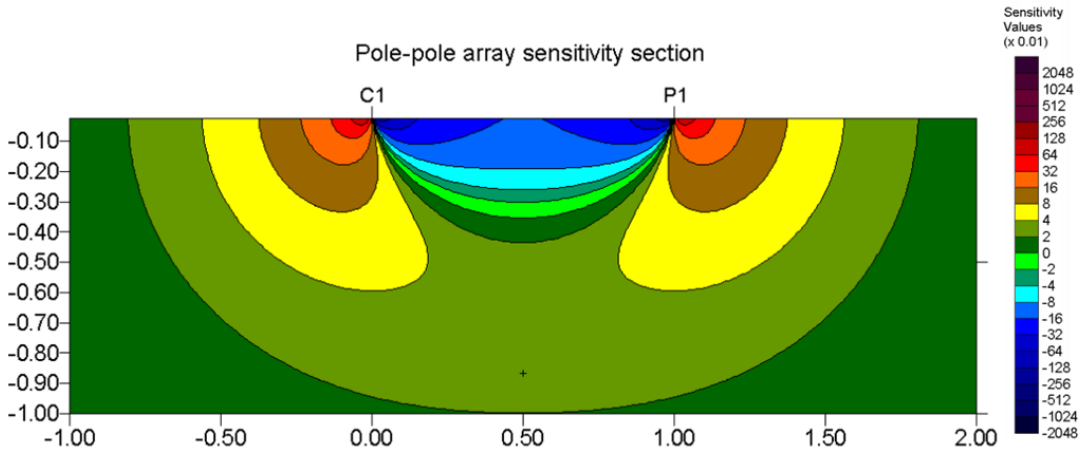

Figure 1.11 Sensitivity plot contours for pole-pole array (from Locke, 2015).

Pole-dipole

Pole-dipole array (Figure 1.12) requires a remote electrode, the C2 electrode, which must be placed far from the survey line. The sensitivity plot presented in Figure 1.12 show that the area with the highest sensitivity can be found beneath the dipole pair P1-P2, especially for large “n” factors. With values of n=4 and higher, the high positive sensitive part found under the P1-P2 dipole becomes increasingly vertical. Thus, this array is probably more sensitive to vertical structures similar to the dipole-dipole array, and it has a relatively good horizontal coverage. It also has significantly higher signal strength in comparison to the dipole-dipole array and it is not as sensitive to telluric noise as explained for the pole-pole array (Loke, 2015).

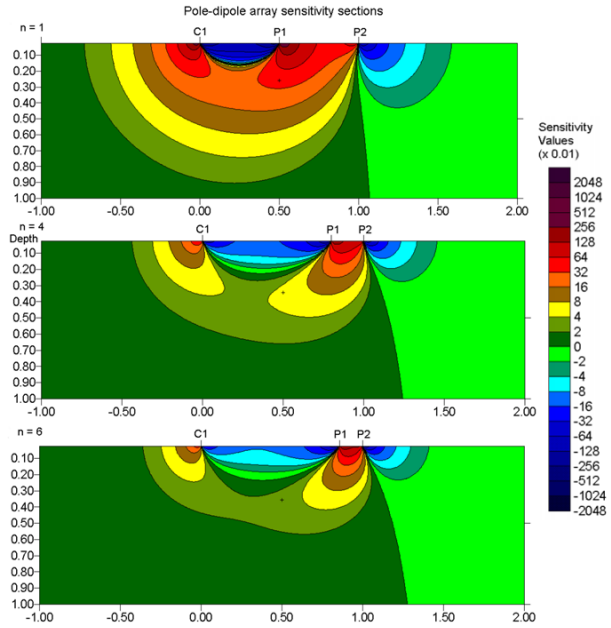

Figure 1.12 Wenner-Schlumberger array sensitivity plots for n=1, 4, and 6 (from Locke, 2015).

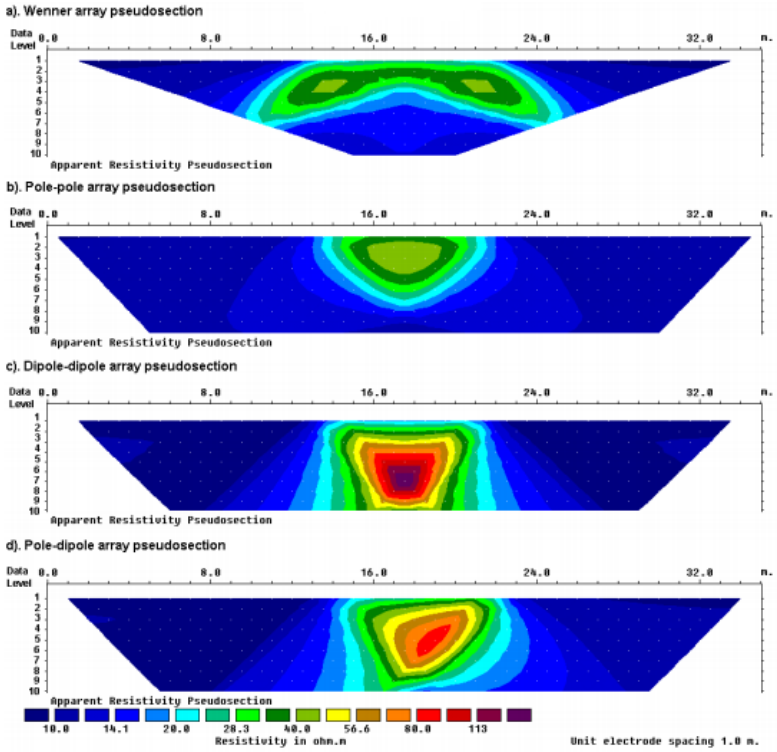

Figure 1.13 Horizontal coverage of each array (a) Wenner, (b) Pole-pole, (c) Dipole-dipole, (d) Pole-dipole (from Locke, 2015).

1.2.6 3D Resistivity survey

Geology of the subsurface is usually in 3D setting. Therefore, 3D resistivity surveys using a 3D interpretation models give the most accurate results. On the other hand,

survey costs are relatively high. Researchers developed a 3D resistivity survey system to reduce survey costs and make it more convenient for survey. One of developments is a multi-channel resistivity meter that allows more than one reading at a time. By this the survey time can be reduced. A second development provides faster computing power which enables the inversion of quite large data sets (Loke, 2015).

Array type and data acquisition of 3D survey

The pole-pole, pole-dipole and dipole-dipole arrays are often used for carrying out 3D electrical resistivity surveys. The reason is that other arrays have poorer data coverage close to the edges of the survey grid. Advantages and disadvantages of the three arrays discussed in above sections are also valid for 3D surveys (Loke, 2015).

Pole-pole array

A possible arrangement of electrodes is shown in Figure 1.14 that connects to a multi-electrode system with 25 nodes (5×5) (Loke, 2015). For convenience, the electrodes are usually arranged in a square grid with the same unit electrode spacing in the x and y directions. In this case, each electrode is in turn used as a current electrode and the potential at all the other electrodes are measured by multi-channel resistivity meter. It is can be quite time-consuming (several hours) to make such a large number of measurements. The “cross diagonal” survey are used to reduce the number of measurements required without seriously decreasing the quality of the model obtained (Figure 1.15). Measurements of the electrical potential are made only at the electrodes along the x- and y-direction and the 45° diagonal lines going through the current electrode. Figure 1.16 shows the sensitivity values on horizontal slices. Near the surface, there is an approximately circular region with negative sensitivity values. The zone with the largest sensitivity extends in the y-direction to slightly over half the electrode spacing. This means to get a complete 3D profile with 2D parallel lines, the spacing between the 2D lines should has to larger than the smallest electrode spacing used (Loke, 2015). The pole-pole array has two main disadvantages. First, it has a quite poor resolution compared to other arrays. Structures in the Earth are often being smeared out in the final inversion model. The second disadvantage is that for particularly large electrode spacing the second current and potential electrode has to be placed sufficiently far from the survey grid (Loke, 2015).

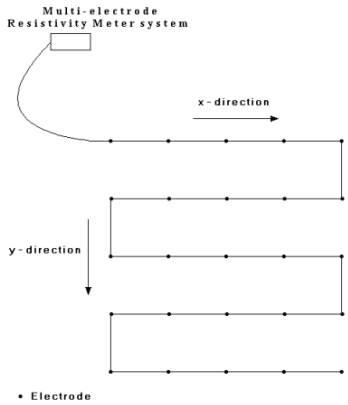

Figure 1.14 Simple arrangements of the electrodes for a 3-D survey (from Loke, 2015).

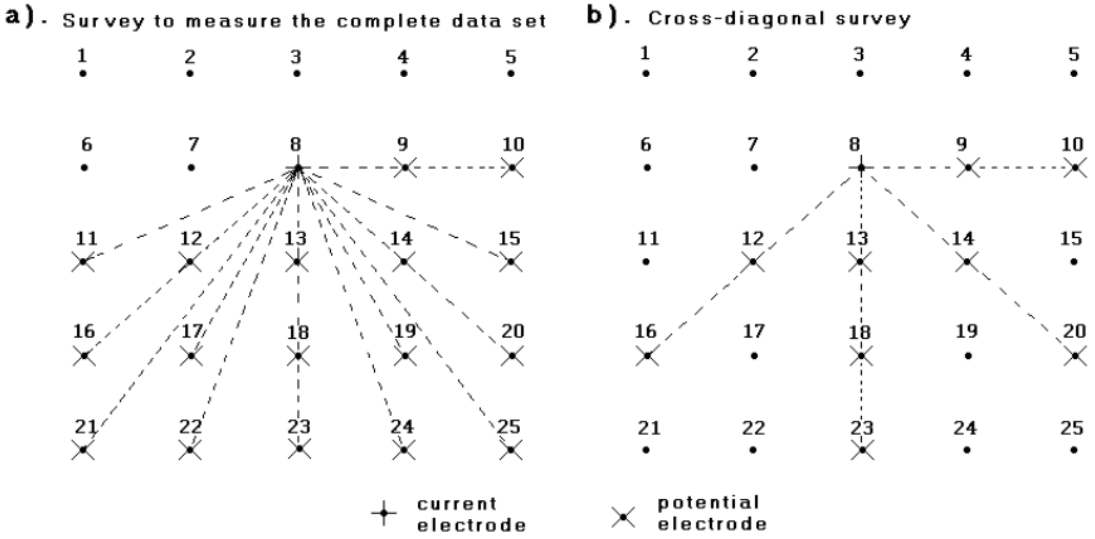

Figure 1.15 Two possible 3-D survey measurement sequences shown. Potential electrode position corresponds to a single current electrode in the setup used by (a) for a survey to measure the complete data set and (b) for a cross-diagonal survey (from Loke, 2015).

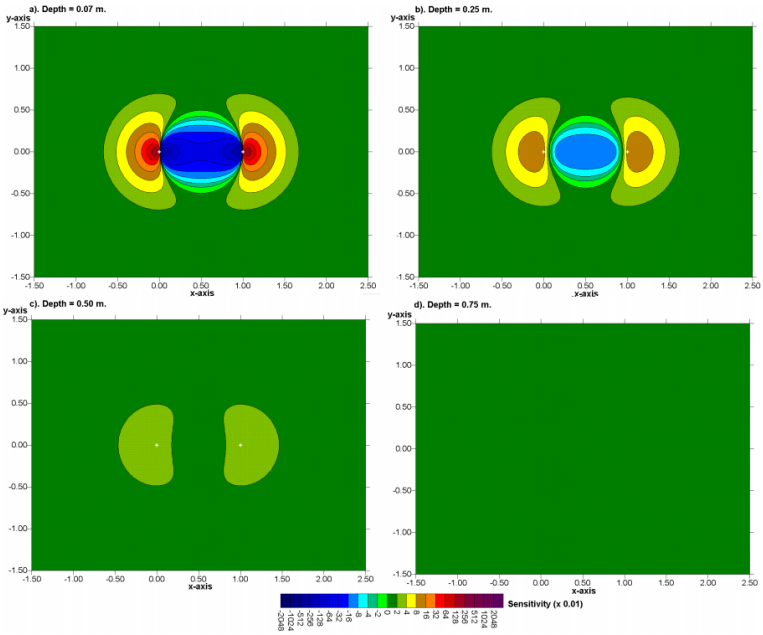

Figure 1.16 3D sensitivity plots of pole-pole array. Plots shown in horizontal slices at different depths (from Loke, 2015).

Pole-dipole array

This array appropriates for medium and large survey grid (12×12 and larger). One of current electrode (C1) and both of potential electrodes (P1 and P2) are kept within survey grid. The remote electrode (C2) must be placed far from the survey line. By this arrangement, this array has better resolution than pole-pole array, less susceptible to telluric noise and it has significantly stronger signal compared with dipole-dipole array. As the pole-dipole array is an asymmetrical array, measurements should be made with the "forward" and "reverse" arrangements of the electrodes (Loke, 2015).

If a 3D survey is done with only a number of parallel lines (without cross-line measurements), the distance between these lines is within 2-3 times of the in-line electrode spacing. By this it is ensured that the subsurface material between the lines is mapped adequately by the in-line measurements (Loke, 2015).

Dipole-dipole array

This array actually used for grid larger than 12×12 (Figure 1.17) due to poorer horizontal data coverage. Figure 1.18 and Figure 1.19 show sensitivity patterns for the dipole-dipole array when the "n" factor is equal to 1 and 4 respectively. The pattern of off-axis elongation of the sensitivity contours show that the dipole-dipole array is more sensitive to 3D effects compared to other common arrays. In many cases, 3D data sets for the dipole-dipole arrays are constructed from parallel 2D survey lines. Due to the elongated shape of the sensitivity pattern, a larger spacing between the lines

of the dipole-dipole array can be used (about three times the inline electrode spacing). The data set would still contain significant 3D information (Loke, 2015).

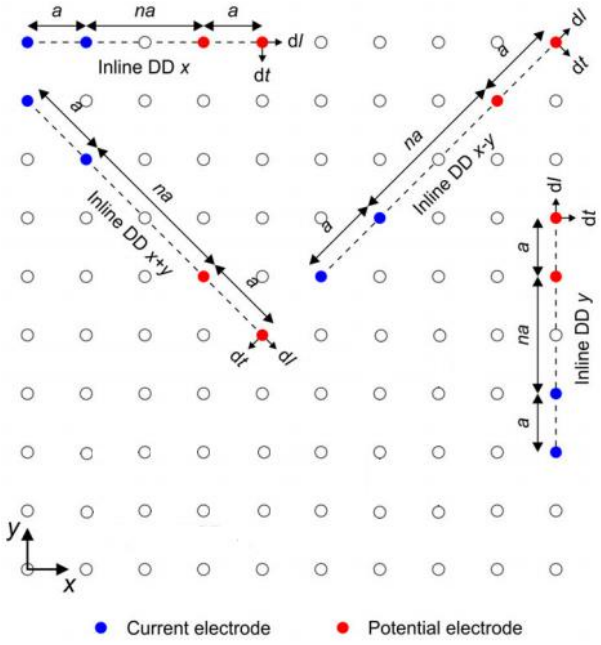

Figure 1.17 Example of dipole–dipole configurations oriented along x and y directions or inter cardinal directions x−y and x+y (from Loke, 2015).

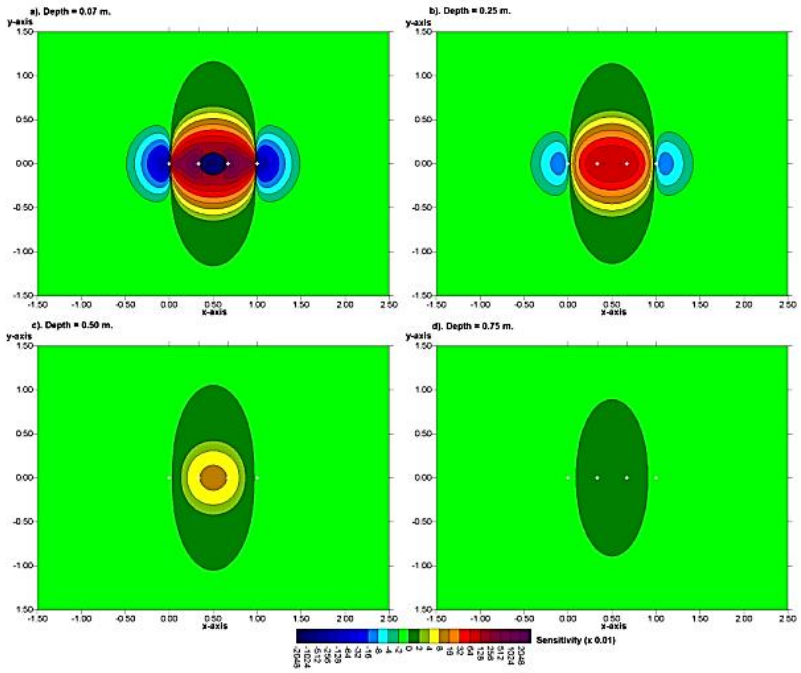

Figure 1.18 3D sensitivity plots of dipole-dipole array with n=1 in horizontal slices at different depths (from Loke, 2015).

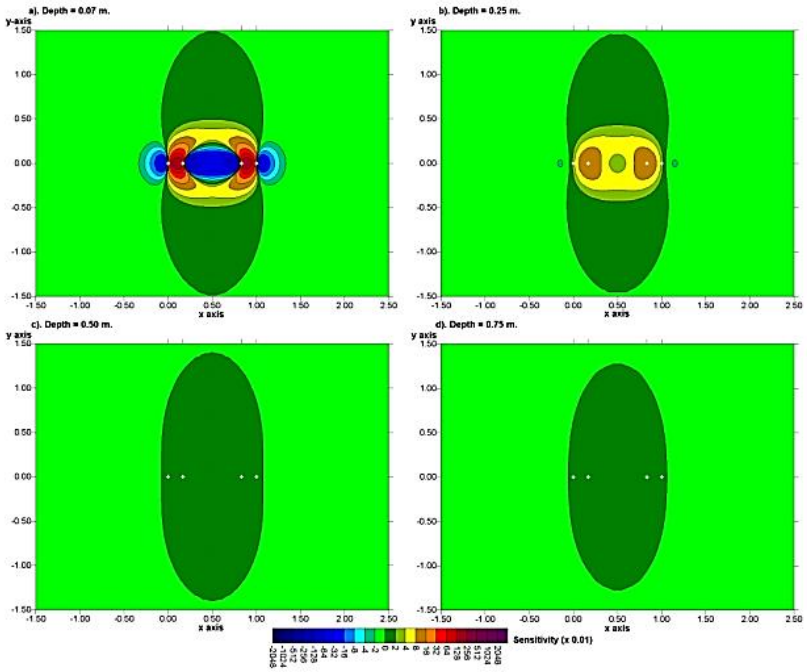

Figure 1.19 3D sensitivity plots for dipole-dipole array with n=4 in the horizontal slices at different depths (from Loke, 2015).

1.2.7 4D Resistivity survey (time-lapse survey)

Despite the 3D resistivity surveys are useful tools for study the structure of shallow subsurface but they only provide static information. Some geological information rapidly changes over time (in order of days, months) such as landslide and groundwater aquifer. Understanding, monitoring, and prediction of such unstable structures researcher developed new acquisition procedure known as time-lapse ERT (tl-ERT, 4D-ERT), to see changes of resistivity over time (Perrone et al., 2014).

Time-lapse ERT surveys are in general done using multi-channel systems which allow the simultaneous measurement of the potential values on many channels using a single pair of current electrodes. As it takes some time to study the structure with 4D ERT system, a set of instruments is permanently installed on the ground over a certain period of time, and multi-electrodes system are buried about 10-20 cm beneath the surface to avoid surface accidents. This system can be operated with telemetric control (Gance et al., 2016).

The resistivity ratio method is used to determine the resistivity change over time (Figure 1.20). Generally, comparison of resistivity at the same site with different time can determine how the fluid flow under the subsurface is changing. This is an important tool for predicting unstable structures such as landslides (Uhlemann et al, 2015).

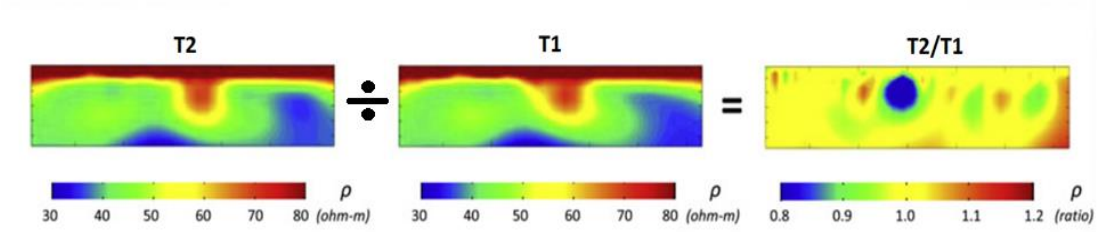

Figure 1.20 Resistivity ratio method used for interpretation of 4D ERT (from Uhlemann et al, 2015).

1.2.8 Sedimentary and sedimentary rock

Sedimentary rocks are made up only the thin layers of the Earth's near surface, 5% of Earth's crust. However, sediment and sedimentary rock compose 75% of all the rocks exposed at Earth's land surface (Chernicoff, 1999).

Mechanical and chemical weathering made solid particles, ion and compound in solution from original rocks. These materials are the source of sediment and sedimentary rock. Sediments are transported by running water, wind, glacier and wave from the place where they were weathered to some suitable area where the sediment can be deposited, called the depositional environment. Generally, geologist separate depositional environments into three areas: continental, transitional between continental and marine, and marine environment (Chernicoff, 1999).

The process that is turning sediments into sedimentary rock is called lithification, which involves compaction, cementation, or both. Compaction is the process by which the volume of the sediment is reduced. When sediment layers were deposited for a long time, pressure from increased weight of the overlying sediment squeezes water and air out from the pore space between deeply buried sediment grains and pack the grain more closely together, converting sediment grains into sedimentary rocks. Cementation is the process where material dissolved during chemical weathering precipitate from water circulating in the space between the sediment grains creating chemical cements that bind the sediment grains together (Monroe et al., 2007). The most common cements in sedimentary rock are calcium carbonate ($CaCO_3$), silicon oxide (SiO_2), iron oxide, and iron hydroxide, such as hematite (Fe_2O_3) and limonite [$FeO(OH)\cdot nH_2O$].

Geologists classify sedimentary rocks as either detrital or chemical ones, depending on their source of materials. Generally, detrital sedimentary rocks are made up from solid particles, while chemical sedimentary rock consists of interlocking mosaics of crystals derived from dissolved compounds made from chemical weathering processes (Chernicoff, 1999).

Detrital sedimentary rocks are made up from solid particle such as gravel, sand, silt and clay. They have clastic texture, composed of particles or fragments known as "clasts". Classification of detrital sedimentary rocks depends on their particle size.

Table 1.3 shows the classification of detrital sedimentary rocks based on grain size. Grain size of sand is 0.0064-2 mm, gravel is larger than sand, and mud is smaller than sand (Chernicoff, 1999; see Figure 1.21, Table 1.3).

Table 1.3 Classification detrital sediments and rocks (Chernicoff, 1999).

Particles size (mm)	**Particle name**		**Name of rock formed**	
<0.004	Clay	Mud	Shell	Mudstone
0.004-0.0634	Silt		Silt	
0.064-2	Sand		Sand	
2-4	Granule	Gravel	Breccia (if particles are angular) Conglomerate (if particles are rounded)	
4-64	Pebble			
64-265	Cobble			
>265	Boulder			

Conglomerates and sedimentary breccia are made up of gravel-sized particle, larger than 2 mm. The difference between the two is that the gravel in the conglomerate is round, while sedimentary breccia have angular particles. There are various types of gravel in the conglomerate and breccia; it may be rock fragments or large pieces of individual minerals.

Sandstone is made up of sand-sized particles with sizes between 0.0064 to 2 mm and accounts for approximately 25% of all sedimentary rocks. There are three major types of sandstone separated by their composed particles. Quartz-sandstone composed mostly of quartz grains (90%) with very little surrounding grains. Arkoses are distinctive pinkish sandstone, containing more than 25% of feldspar. Graywackes are dark, gray to green sandstones that contain a mixture of quartz and feldspar grain, dark rock fragments and fine-grained clay and mica matrix.

Mudrock is a general term that used for detrital sedimentary rock composed of silt- and clay-sized particles. Siltstone is composed of mostly silt-sized particle, mudstones are a mixture of silt and clay and claystone are made up of mostly clay-sized particles. Some mudstone and claystones are classified as shale if they are break along closely space planes. About 40% of all sedimentary rocks are mudrocks. Thus, they are more abundant than conglomerates and sandstones. Because silt- and clay-sized particles are so small, they are transported by weak current and kept suspended in water. Thus, depositional environment of mudstone is the place where the current and turbulence are at minimum such as in lake, in lagoon, in deep ocean basin and in river floodplains (from Chernicoff, 1999 and Monroe et al., 2007).

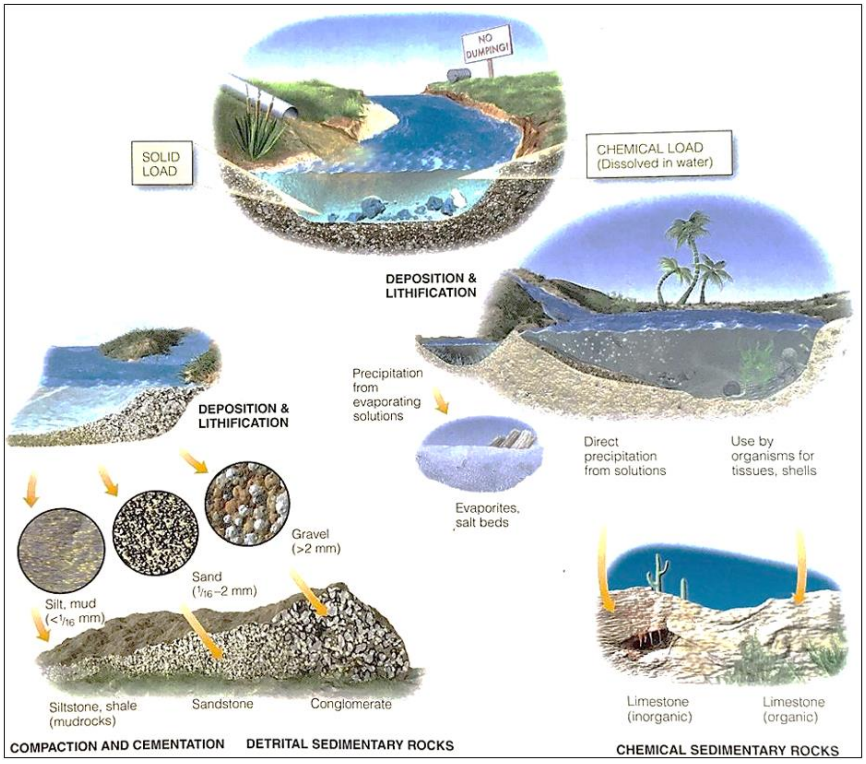

Figure 1.21 Processes of detrital sedimentary rocks made up from solid particles while chemical sedimentary rocks consist of interlocking mosaics of crystals derived from dissolved compounds (from Monroe et al., 2007).

1.2.9 Rock deformations

Effects of plate tectonics make a powerful force to rocks, called stress, force applied to rock per unit area. If the rock is stressed, it become deformed, changing in shape and often volume, called strain. Generally, there are three types of stress applied to rocks depend on type of plate-boundary movements (Chernicoff, 1999). Rocks at converging plate boundaries are pushed together; this type of stress is called compression. General effects of compression on rocks are thickened vertically and shortened laterally. Rocks at diverging plate boundaries are pulled apart; this type of stress is called tension. Effects of tension are thinning vertically and lengthen laterally. Rocks at transform plate boundaries are forced pass one another in parallel with opposite direction; this type of stress is called shearing stress. Shear stress slices rocks into parallel blocks, breaking, and displacing rocks and structures, see Figure 1.22A.

When rocks are stressed, strain can be seen in different ways. Figure 1.22B shows the relationship between stress and strain for different types of rock deformation. When stress on rocks is minor, rock will return to their original shape and volume after stress is removed. This temporary deform is called elastic deformation. However, if the larger force is applied to rocks, it may not be a temporary deformation. The maximum stress that rocks can hold before becoming permanently deformed is called yield point,

or elastic limit. When the rock is stressed under conditions of low temperature and pressure, rocks may crack or rupture when the applied stress is more than the yield point. This process is brittle failure. Under high temperature and pressure, if a rock experiences larger stress than the yield point, the rock will permanently change in shape and volume. This process is called plastic deformation. There are many factors affecting rock deformation such as lithostatic pressure, heat, time and composition of rock (Chernicoff, 1999).

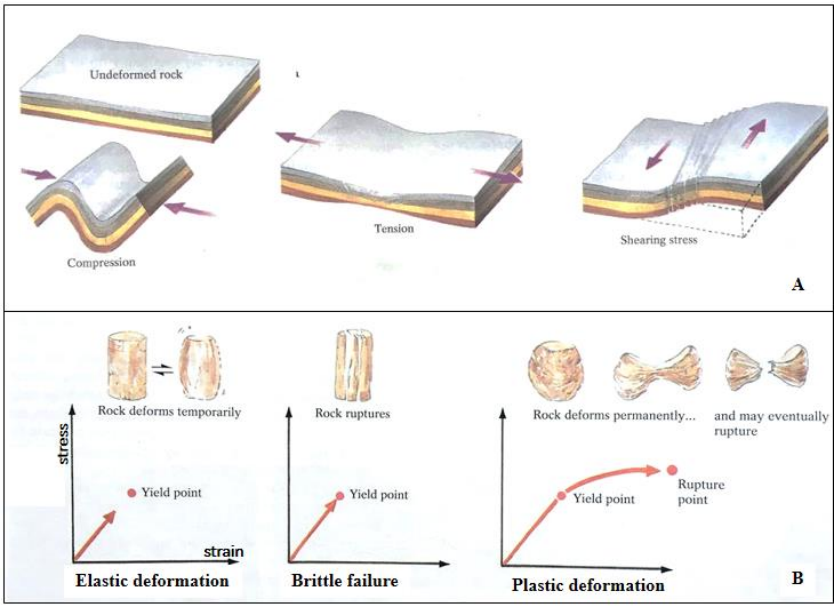

Figure 1.22 Type of applied stress on rocks (A) and Type of rock deformation under difference condition (B) (from Chernicoff, 1999)

When rocks deform under high temperature and pressure at the region of converging plate boundaries, they will fold down and up, forming a shape of troughs and arches. This deformed structure is called folds. There are two common types of folded rock, the trough-like structure is called syncline and the arch-like structure is called anticline. Rocks are brittle under low temperature and pressure condition, near Earth's surface. Results of brittle deformation under these conditions are faults and fractures. Figure 1.23 show that there are three major types of faults in rocks and the structures correspond to the type of applied stress. If the type of stress is tension the hanging wall (body of rock above the fault) moves downwards relative to the footwall (body of rock below the fault), called normal fault. If the type of stress is compassion, the hanging wall moves upwards relative to footwall, called reverse fault. If the type of stress is shearing stress, the rock slides laterally relative to one another, called strike-slip fault (Chernicoff, 1999).

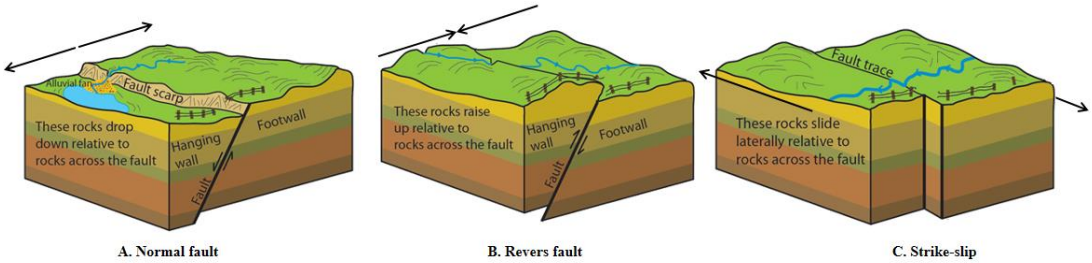

Figure 1.23 Major types of fault, (A) normal fault, (B) reverse fault, and (C) strike-slip (from Earl, 2015)

Determining geological structures in the field can be used for understanding the geological history of a certain area or region (Earl, 2015). Generally, sedimentary rocks are deposited in horizontal layers. In case layers are not horizontal, then it can be assumes that they have been affected by tectonic forces and have become tilted, folded, or fractured. Geologist in general measure the orientation of a plane, e.g. layering, with two values (Earl, 2015; Figure 1.24): First, the orientation of the intersecting line between the surface and the dipping plane, called strike direction. Second, the angle between the surface of the dipping plane and horizontal (perpendicular to strike) is measured, the dip angle. Another parameter is the dip direction, which is perpendicular to the strike direction into the direction of the maximal dip angle. Strike, dip direction, and dip angle are also used to describe any other planar feature, including joints, faults, dykes, sills, and even the foliation planes of metamorphic rocks (Earl, 2015).

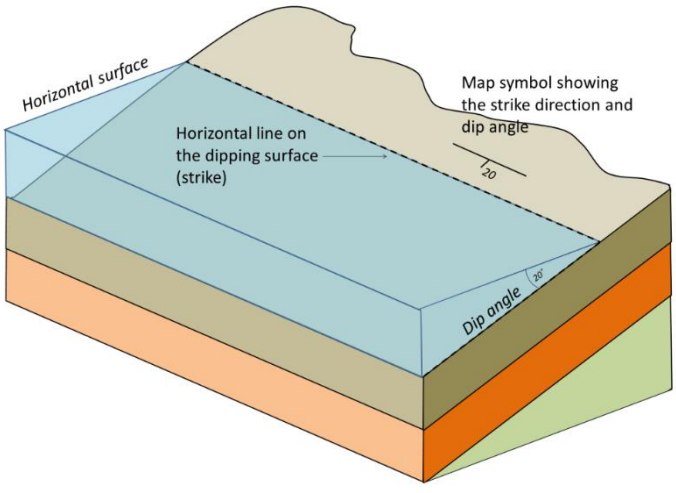

Figure 1.24 Depiction of the strike and dip of some tilted sedimentary beds partially covered with water. The notation for expressing strike and dip on a map is shown (Earl, 2015).

1.3 Applications of various types of resistivity survey

Resistivity surveys are widely used in various types of work depending on survey objective. The main factors and parameters related to resistivity is fluid/water and that is the reason why many researchers using resistivity surveys in groundwater exploration (Muchingami et al., 2012, Khalil and Santos, 2013, Asfahani, 2016, Anomohanran et al., 2017, Chabaane et al., 2017 and Mohamaden and Ehab, 2017). 2D, 3D, and time-lapse resistivity surveys have the potential to investigate geohazards such as landslide (Lebourg et al., 2010, Chambers et al., 2011, Travelletti et al., 2012, Chambers et al., 2014, Sebastian et al., 2015, Ling et al., 2016 and Wilkinson et al., 2016) and sinkholes (Ayolabi et al., 2012, Youssef et al., 2012 and Giampaolo et al., 2016). Moreover, 3D resistivity surveys are used to in investigate structures and water contamination in landfill sites (Bichat et al., 2016, Park et al., 2016, Manzur et al., 2016, Maurya et al., 2017 and Di Maio et al., 2018). In soil science and agriculture, researchers use 2D and 3D resistivity surveys to monitor structures and conditions of soil before and while growing plants (Amato et al., 2009, Séger et al., 2009, Boaga et al., 2013 and Séger et al., 2014). Time-lapse electrical resistivity surveys are used to monitor moisture and pattern of fluid moving/flowing in soils (Christopher et al., 2014 and Tildy et al., 2017). As geological structures are set in three dimensions 3D resistivity surveys are used for investigating and identifying subsurface structure (Zeyen et al., 2011, Badmus et al., 2012, Kneisel et al., 2014 and Cardarelli et al., 2017). In forensic science, researcher use 3D resistivity surveys for monitoring and identifying clandestine graves (Pringle et al., 2012).

Kneisel et al. (2014) investigated periglacial landscapes (frozen ground) using resistivity survey, two-dimensional electrical resistivity tomography (2D ERT) and three-dimensional electrical resistivity imaging (3D ERI). They proved that the 3D ERI approach allows the spatial imaging of the resistivity distribution of the subsurface. This approach improves the delineation and characterization of subsurface structures in comparison to 2D ERT, which is limited to data along a single profile or extrapolation between parallel profiles.

At one study site, 22 profile lines of 2D ERT Wenner-Schlumberger surveys with 5 m electrode spacing were carried out; they comprise of 12 parallel profiles along the x-direction and 10 perpendicular lines along y-direction. All were combined to a grid (175 m × 175 m) for making a 3D model (Figure 1.25). The distance between each survey line is 10 m, which is double of the electrode spacing. Results show that the 3D ERI has been successfully applied for permafrost mapping and the characterization of the subsurface, as especially frozen ground often exhibit small-scale spatial heterogeneities related to surface and subsurface conditions (Kneisel et al., 2014).

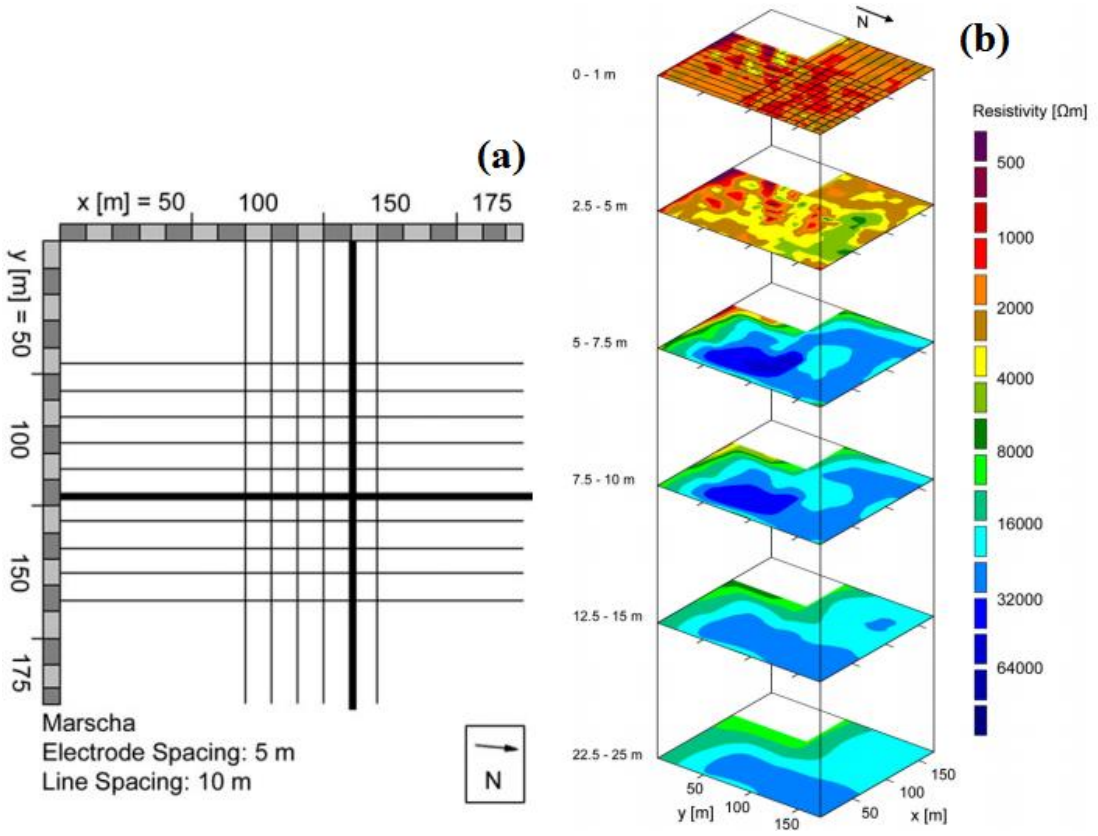

Figure 1.25 (a) Arrangement of survey lines measured in x and y direction building up the measurement grid. (b) 3D model obtained from the inversion of the survey data set (from Kneisel et al., 2014).

Papadopoulos et al. (2010) carried out 3D ERT at a tumuli area, artificially erected small hills that cover monumental tombs or graves. 3D ERT composed of parallel profile lines of 2D ERT, was used to characterize the properties of the tumuli filling material and to resolve buried archaeological structures inside the tumuli. Before field work, forward modeling was used to estimate the efficiency of each array type; dipole–dipole (DD), pole–dipole (PD), pole–pole (PP), gradient (GRAD), midpoint-potential-referred (MPR), and Schlumberger reciprocal (SCR) (Figure 1.26a). Generally, the forward model showed that PD and the GRAD arrays comprise the optimum choices to investigate such area (Figure 1.26b). The field work data collected employing the PD array along a small tumulus, 38 parallel 2D lines in total along a single survey direction (y-axis), inter-line distance was 0.6 m, 33 electrodes along each line were installed with electrode spacing (a) of 0.6 m. Inversion models showed that there are a number of archaeological structures that exhibit a high possibility to correlate with graves (Figure 1.27). Overall, 3D ERT method can provide a valuable tool in the non-destructive archaeological exploration (Papadopoulos et al., 2010).

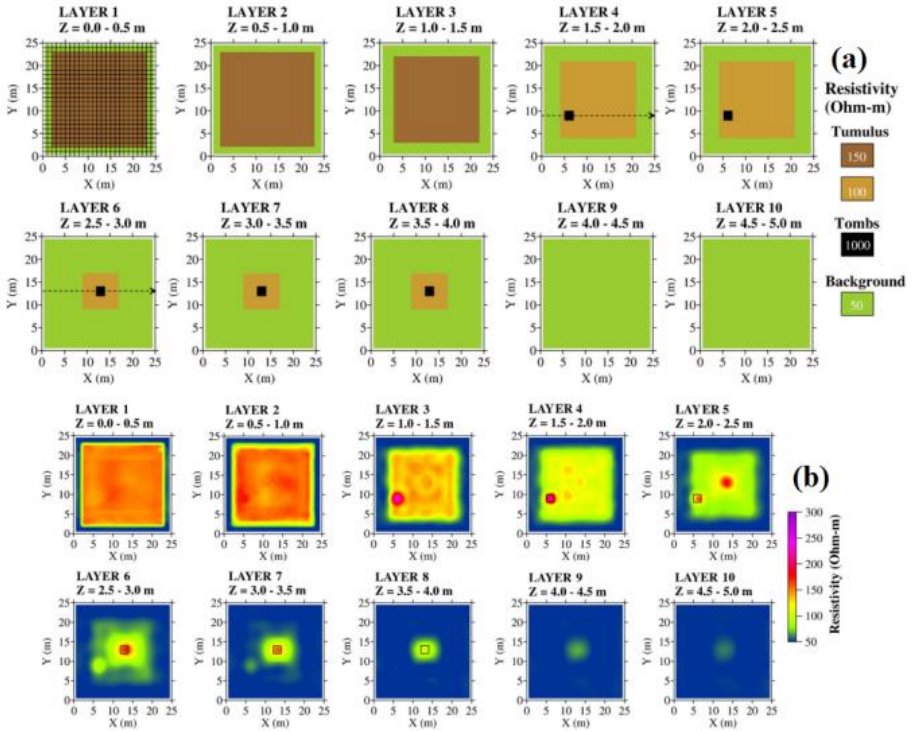

Figure 1.26 (a) 3D resistivity model used to simulate the filling material and the tombs that are buried inside the tumulus. (b) Forward model using pole-dipole array (from Papadopoulos et al. 2010).

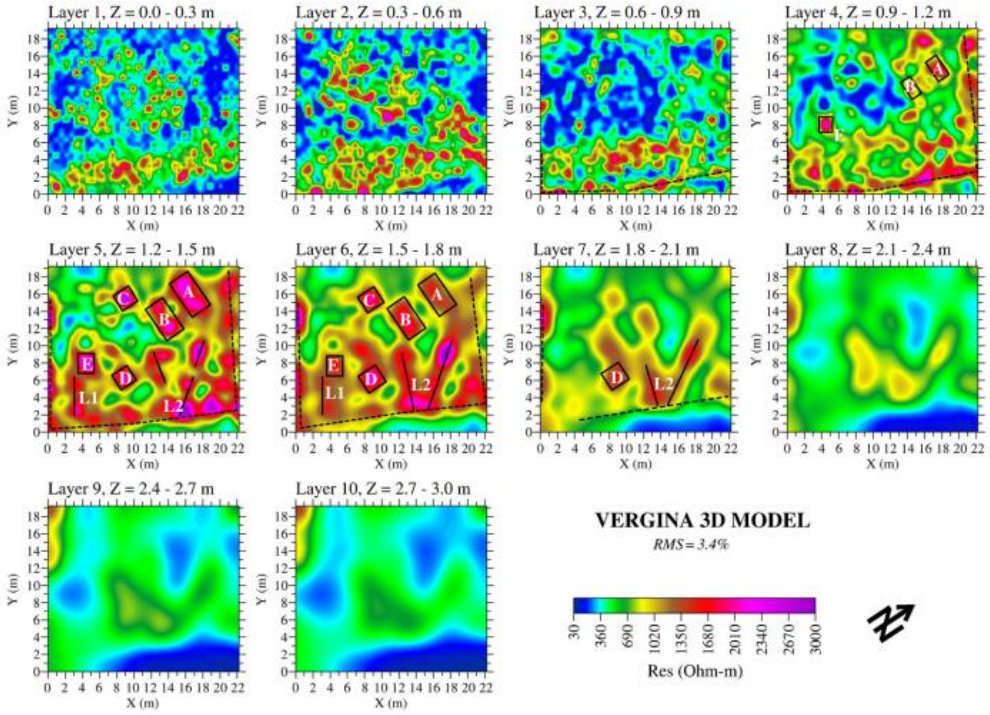

Figure 1.27 Inversion model from field work, investigated by pole-dipole array (from Papadopoulos et al. 2010).

Gance et al. (2016) observed changes in electrical resistivity monitored at the Super-Sauze clayey landslide with the GEOMON4D, as time-lapse electrical resistivity tomography (tl-ERT) is often used to measure, map, and monitor water circulation in the soil. With instruments permanently installed on study for a period of one year, resistivity of the subsurface was measured two times per day (period of 12 hours), together with other hydrological process detectors, like groundwater level, surface temperature, and global positioning coordinates. Results show infiltration and movement of water in the subsurface after rainfall event expressed as the percentage change of resistivity (Figure 1.29, Gance et al., 2016).

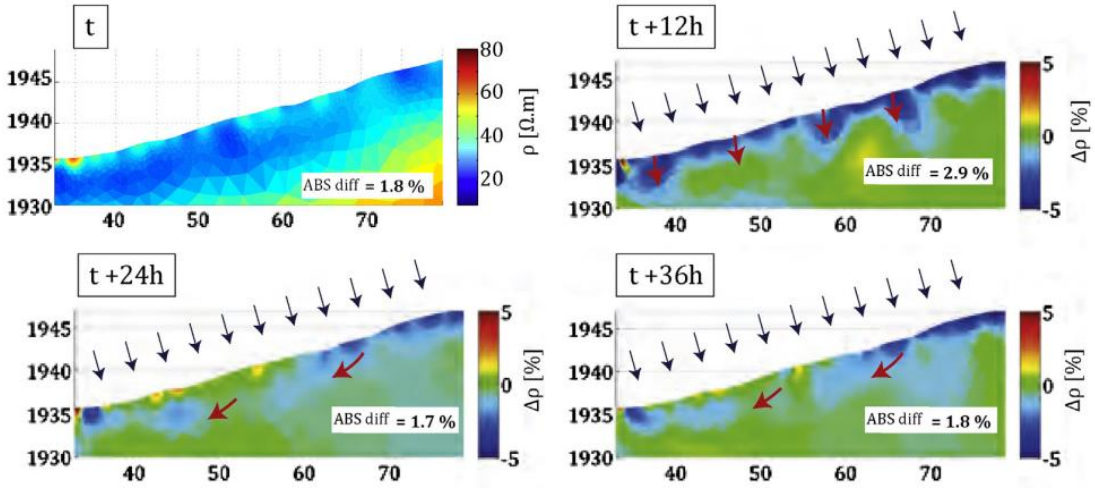

Figure 1.28 Resistivity responds after the rainfall shown as the percentage change of resistivity (from Gance et al., 2016).

Bermejo et al. (2016) carried out 2D and 3D to identify karst structures, landscape formed from the dissolution of soluble rocks such as limestone, dolomite, and gypsum. It is characterized by underground drainage systems with sinkholes and caves. 8 parallel profile lines of 2D ERT with Wenner-Schlumberger array, 72 electrodes for each profile line, electrode spacing was 2 m and inter-line spacing distance was 2 m. Res3Dinv software was used to combine the data of the eight 2D survey lines into a 3D data set and create depth slices. 3D profiles were arranged in deep horizontal slices to a depth of 20 m (Figure 1.28). This work shows the suitability of the ERT technique for prospecting karst structures, as it provides the possibility to map the morphology of caves (Bermejo et al., 2016).

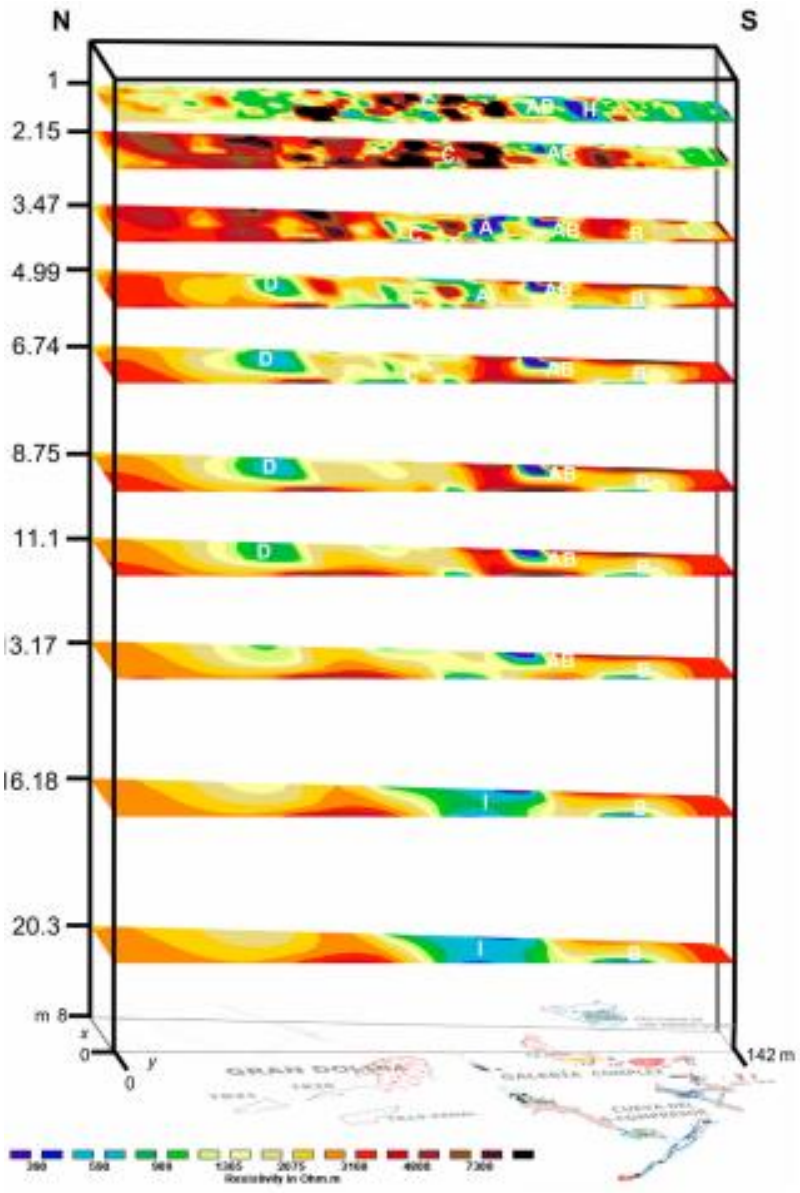

Figure 1.29 Horizontal depth slices of 3D profile investigated on karst structure (Bermejo et al., 2016).

CHAPTER 2

RESEARCH METHODOLOGY

2.1 Equipment preparation

Before carrying out the resistivity surveys, the equipment required were first prepared. The equipment for resistivity survey mainly consists of ABEM SAS1000 resistivity meter, steel electrodes, cable, and battery. Moreover, other necessary equipment such as hammer, measuring tape, duct tape, cutter and cutting tool were prepared to use with the main equipment. Table 2.1 shows the equipment list that was actually brought to the study area.

In this work, a switch box and a cable assembly were developed to use with the single-channel resistivity meter to get full 3D resistivity data. Both are designed for convenience in data measuring and reduction in survey time.

Table 2.1 Equipment list for 3D resistivity survey.

Equipment	**Amount**
ABEM SAS1000 resistivity meter	1
Steel electrodes	120
Cable	Assembly cable
12V Battery	2
Hammer	4
Measuring tape	10
Cutting tool	2
Cutter	4
Duct tape	

2.1.1 Switch box

Figure 2.1 show a picture and diagram of the switch box. This equipment is made up from a plastic box, cables, and cable connectors. The switch box is designed to connect to ten electrodes at the same time. Thus, the maximum number of electrodes that can be connected with the switch is ten per measurement line. There are two connecting side on the switch box, one side for connecting to the resistivity meter and one side for connecting to the cable assembly. The switch box is connected to the resistivity meter by four cables, C1, C2, P1 and P2. In addition, it is connected to all electrodes by the cable assembly.

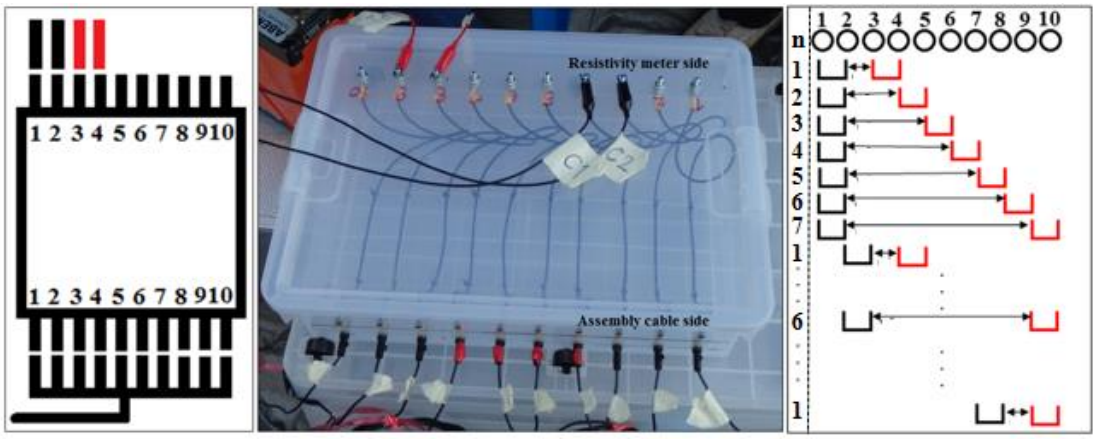

Figure 2.1 Diagram of switch box and sequent of cable moving of dipole-dipole array, Black is current electrode C1 and C2, Red is potential electrode P1 and P2

2.1.2 Cable assembly

The cable assembly connects the switch box and electrodes. In this work, ten cables were assembled together to make the cable assembly. There are two lengths of cables, 130 m for cable number 1, 2, 3, 8, 9 and 10 and 110 m for cable number 4, 5, 6 and 7. Thus, 20 m is the maximum electrode spacing that can be used with this cable assembly. Figure 2.2 shows a picture of the cable assembly. One side of the assembly use to connect with the switch box and another side use to connect with electrodes along the measurement line.

Figure 2.2 Cable assembly consists of ten single cables assembled together.

2.1.3 Equipment set up and measuring

Figure 2.3 shows the equipment setup. The equipment setup starts by making a square grid using measuring tapes in the study area and then planting electrodes into the ground with the designed electrode spacing. All corner locations of the square grid are measured by global positioning system (GPS) in UTM coordinates (WGS-84). The orientation of the grid is measured by a compass in azimuthal angles. In addition, surface conditions in study area are observed. Then, each electrode gets a label according to an x, y coordinate system. After finishing making the grid and putting the electrodes, the 12V battery is connected to the ABEM SAS1000 single-channel resistivity meter. The resistivity meter then is connected to the switch box by four connecting cables C1, C2, P1 and P2. Finally, the switch box is connected to 10 electrodes along one measurement line by the cable assembly.

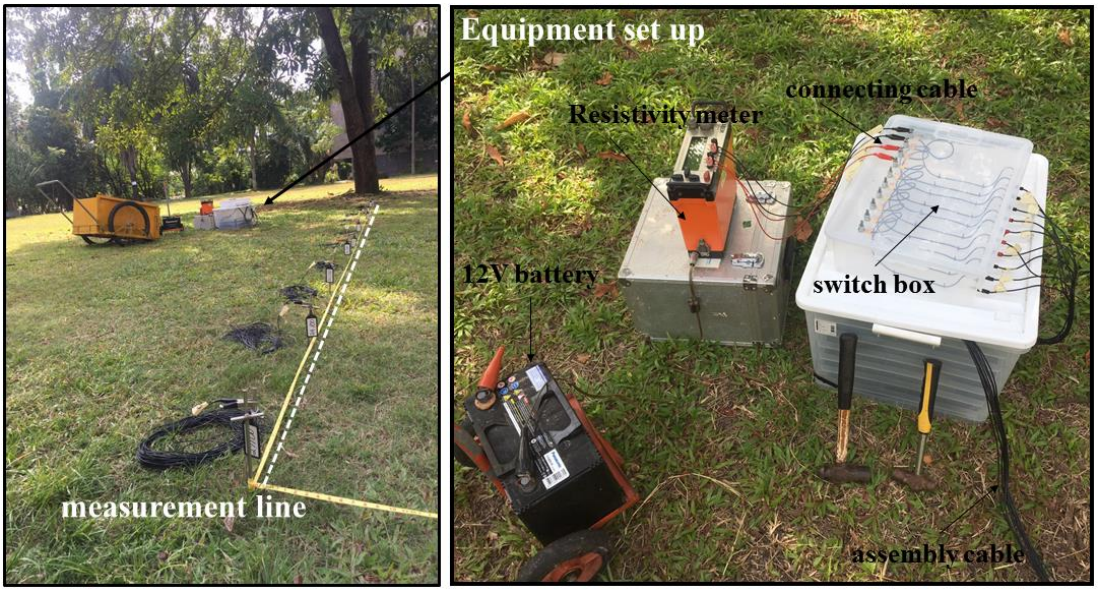

Figure 2.3 Example of equipment setup, consist of resistivity meter, connecting cables, switch box, cable assembly and 12V battery.

All data in a measurement line are measured by moving the position of the connecting cables. For measurement of the resistivity in dipole-dipole array, the first position of the four cables on the switch box start from channel 1 to 4 with n=1, where n is the ratio between distance from C1 to P1 and electrode spacing, show in Figure 2.10b. After that, the next data point is measured by moving P1 and P2 cable to position n=2 until n=7 (maximum for 10 electrodes per one measurement line). After finishing measuring data at n=7, four connecting cables are moved to channel 2-5. Data are measured again from n=1 until maximum n=6. These steps of measuring are continued until maximum n is 1, show in Figure 2.1. By this the number of measured data per one measurement line which measured by dipole-dipole array should be 28 data

points. After all data in a measurement line are measured, the cable assembly was disconnected from all electrodes and reconnect with electrodes in the next measurement line. Normally, the number of measurement lines of a 10×10 square grid is 46 lines (840 data), 10 lines on x-axis, 10 lines on y-axis and 26 lines on both diagonal axes.

2.2 Testing of acquisition system

2.2.1 Measuring on testing area

The 3D acquisition system was tested before going into the study area. The purpose of testing is to study the procedure of survey making, survey time, and to get data to process with the inversion software. Testing area is located at the Faculty of Science courtyard, Prince of Songkla University. The approximate size of this area is 50×40 m^2. In the northern part of courtyard is the chemistry building, in the eastern part is the cafeteria, in the western part is the biology building, and in the southern part is the physics building.

There are three measurements in testing process. The first measurement is a square grid with 7×7 electrodes with an electrode spacing of 2 m; area size is 12×12 m^2. Second measurement is a square grid with 10×10 electrodes with the same electrode spacing of 2 m; area size is 18×18 m^2. Finally, the third measurement is a square grid with 10×10 electrodes with an electrode spacing of 3 m; area size 27×27 m^2. Figure 2.4 shows an overview map of the testing area. All measurements have the same location of the origin point (0, 0). Orientation of the survey grid is 90 degrees from north to x-axis. The resistivity data of all surveys are measured by dipole-dipole array in all directions; x-direction, y-direction, and both diagonal directions.

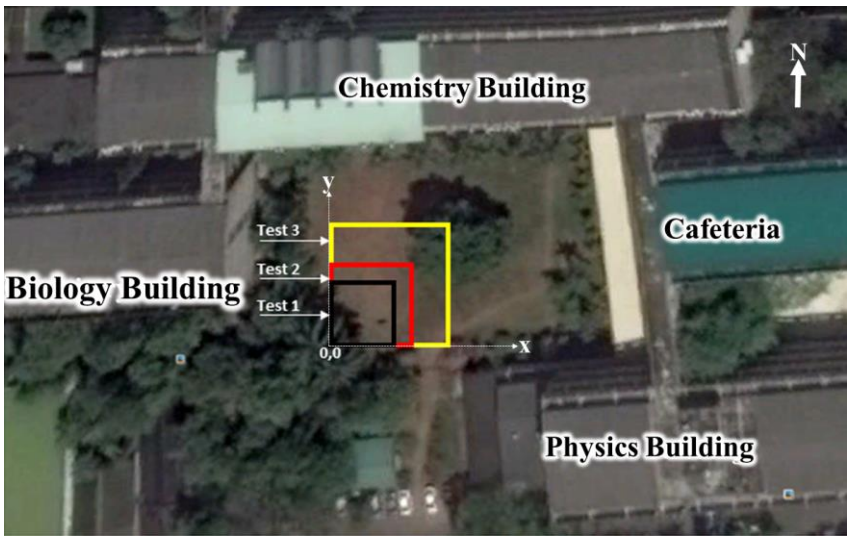

Figure 2.4 Overview map of testing area at Faculty of Science courtyard, Prince of Songkla University.

2.2.2 Data processing

Measured data from the survey is resistance value in Ohm (Ω). These data are converted to be apparent resistivity (ρ_a) in Ohm-m (Ω-m) as multiplied with the geometric factor (k) which depends on the electrode arrangement and spacing. The apparent resistivity data are processed by RES3DINV inversion software which carries out an inversion of the apparent resistivity data to a resistivity model of the subsurface (Demo version is used in this work). Table 2.2 shows the format of the data that are used as input to the software. Results from this software are images of resistivity distribution in various sections; horizontal-, X-, and Y- section. Data used to process with the software are saved in DAT file.

Table 2.2 Data input format used to input into RES3DINV software.

Field Test 1									**Title**
10									Number of electrodes in x-direction
10									Number of electrodes in y-direction
3.0									x unit electrode spacing
3.0									y unit electrode spacing
3									Array type, 3 for dipole-dipole
840									Number of data
3	0	0	0	6	0	9	0	84.5	Location of four electrodes (C1, C2, P1 and P2) on x- and y-axis And apparent resistivity value.
3	0	0	0	9	0	12	0	76.0	
3	0	0	0	12	0	15	0	108.7	
3	0	0	0	15	0	18	0	121.2	
.									
.									
.									
3	21	0	18	6	24	9	27	51.5	
0									End with a few zeroes
0									
0									
0									

2.3 Study area

After testing the data acquisition system, this system was used to carry out measurements in a study area. An appropriate area should be an area that has some geological structures which we already know or can be seen from the surface. By this way, results from the resistivity survey can used to compare with geological data in order to prove the quality of the geophysical survey.

2.3.1 Location of study area

A study area in Songkhla province was chosen as information about the subsurface for this site is already available, including resistivity data (Denke and Dürrast, 2010). The study area was in an old quarry located in the northern part of Sadao district, Songkhla province, Southern Thailand (Figure 2.5a). The northern part is a flat area because rocks and soils have been taken out. In the southern part still remain parts of a hill and sediment layers can be seen from cliffs marking the quarry boundary. All formations in the quarry are sedimentary rocks with conglomerates, conglomeratic sandstone, and sandstone. In some parts of the area sandstone interbedded with siltstone occurred (Figure 2.6).

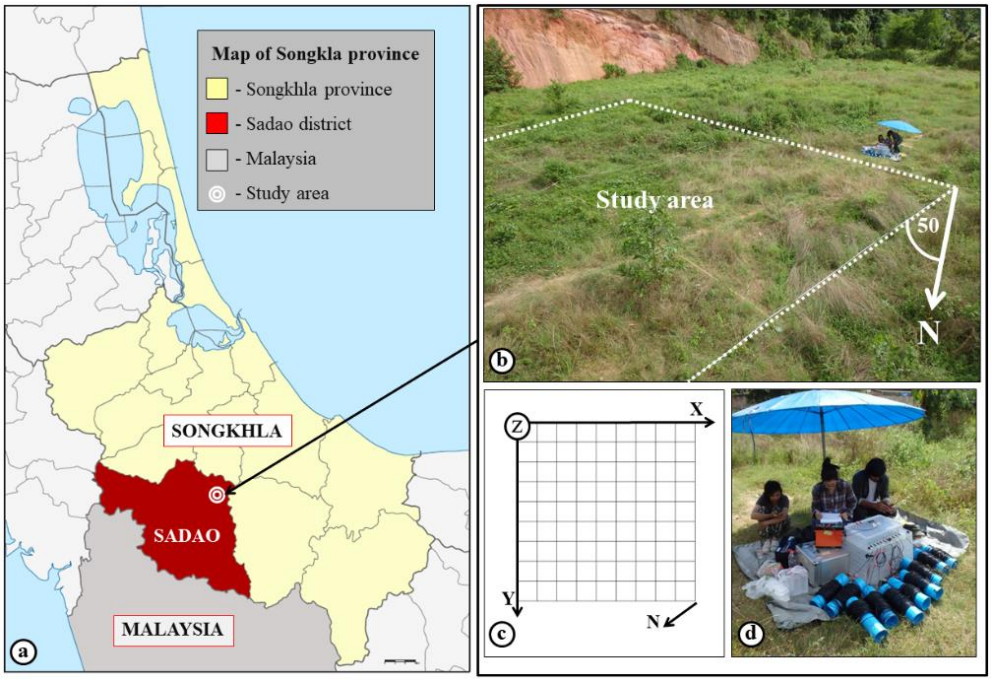

Figure 2.5 Study area (a) Location of study area in northern part of Sadao district, Songkhla province, southern Thailand, (b) Boundaries of the survey area with the direction of the x-axis 50 degrees from north over west, (c) Square grid of 10×10 electrodes with x-, y- and z-direction, and (d) Equipment set up consisting of resistivity meter, 12 V battery, switch box, and cable assembly.

Figure 2.7 shows the surface condition of the study area. There are some big trees located in the eastern part and in the middle of study area. Almost all of the area is covered by high grasses and bushes. There is a slope located in eastern part; slope elevation is approximately 1.5 m. An expected fault is located in middle of area. Some trenches are found located in the western part of area.

2.3.2 Structural geology in study area

Structural geological surface investigations in the study area revealed dipping sedimentary layers and faults (Figure 2.8). Figure 2.8d shows sediment layers dipping into north-west direction (288, dip direction) with dip angles of 15-20 degrees. The upper layer is conglomerate and the lower layer is sandstone and siltstone. Figure 2.8a and 2.8e show a fault that can be found in this area. Measurements of the fault plane show that the fault is dipping into south direction with a dip angle of 64 degrees (dip direction/dip angle, 222/64).

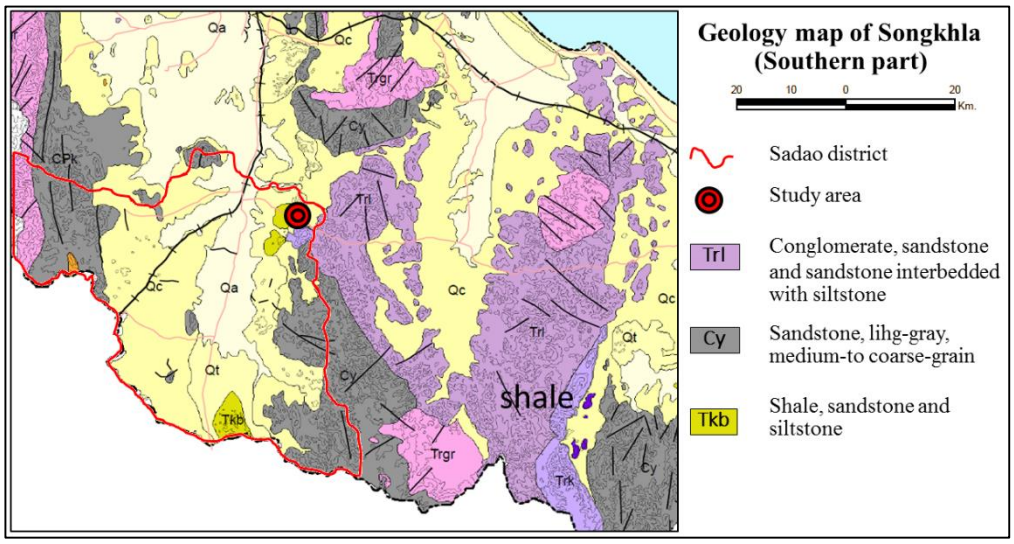

Figure 2.6 Geology map of Songkhla province in southern part (DMR).

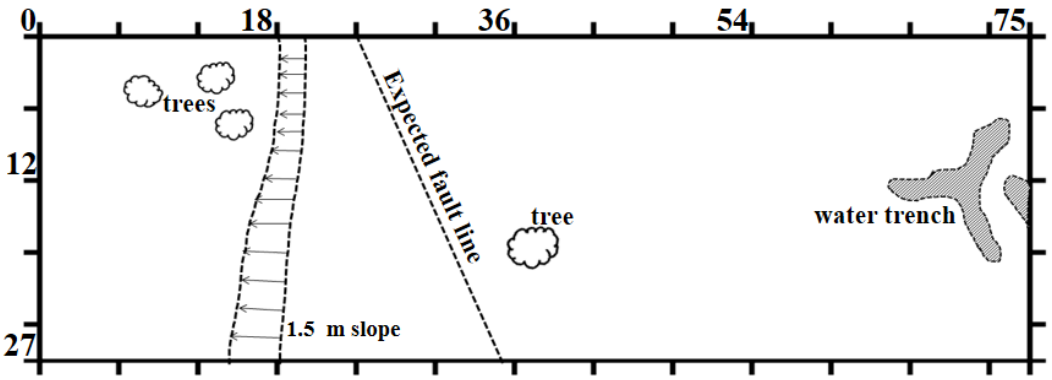

Figure 2.7 Surface condition of study area.

2.4 Geological structure survey

A geological survey is an investigation of the geology beneath the study area for creating a geological map or model. Many techniques are used in geological surveying such as walk-over survey, study outcrops and landform, intrusive methods such as hand auguring and machine driven borehole and use of geophysics technique such as remote sensing method, aerial photography and satellite imaging.

2.4.1 Equipment

Geological survey technique used in this work is walk-over survey for study available outcrops, existing faults, and sedimentary layering. GPS is used for mark locations. Geology compass is used for measuring direction and dip angle of faults and sedimentary layers. Geology hammer is used for take some rock samples.

2.4.2 Surveying

Location, direction, and dip angle of outcrop and sedimentary layering around study area are measured to make a geological model. Information of the geological model consists of expected faults and sedimentary layering. Figure 2.8 show that there are five measurement points of sedimentary layering around the study area. Faults can be seen from the surface. Fault in Figure 2.8a and 2.8b are expected to be the same fault line. Thus, the expected fault line is drawn based on information of these faults. This information also used to compare and co-interpret with results from resistivity survey. Table 2.3 shows the location and information of the geological survey in the study area.

Table 2.3 Location and information of geological survey in study area.

Station	**UTM Location (WGS-84)**		**Dip direction/Dip angle**
	East	**North**	
S1	0665744	0748988	333/20 P Layering, 222/64 P Fault
S2	0665736	0748926	310/18 P Layering, 078/84 P Fault
S3	0665833	0749108	288/15 P Layering
S4	0665846	0749069	260/20 P Layering
S5	0665869	0749021	300/28 P Layering

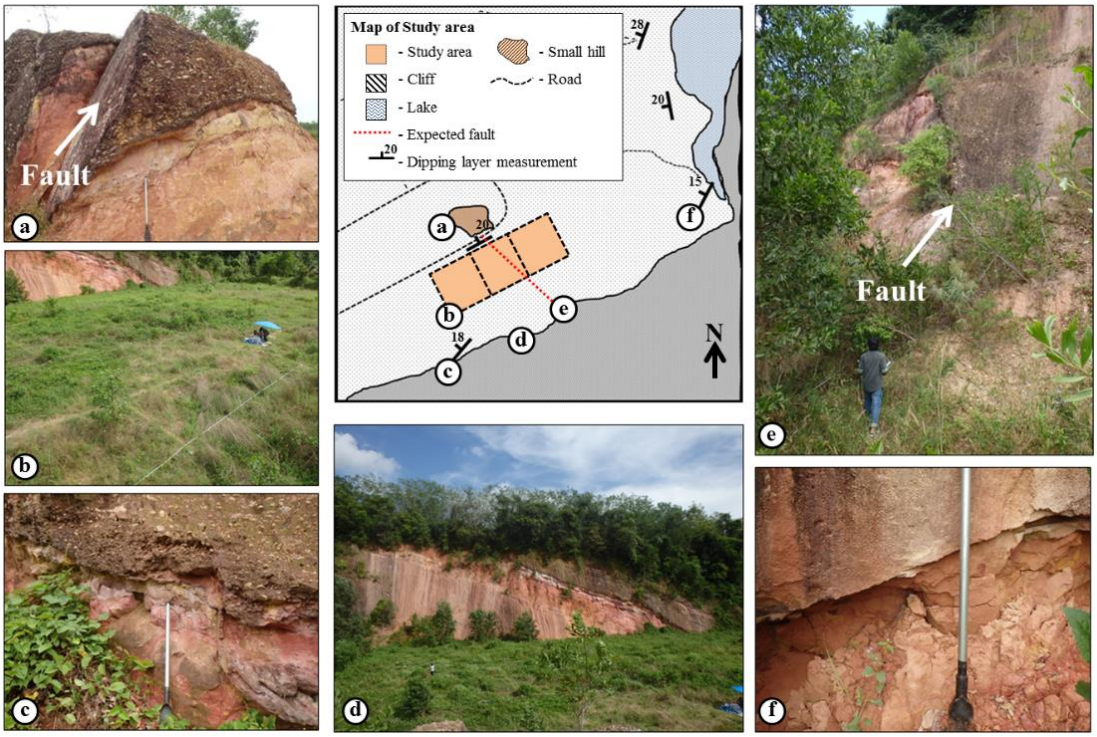

Figure 2.8 Structural geology of study area (a) Fault, looking into NW, dip direction/dip angle of the fault plane is 222/64 and of the sedimentary layering 333/20, (b) Study area, looking into SE, (c) Sedimentary layer in the quarry nearby the study area, looking into SE, and measurement of sedimentary layering is 310/18, (d) Sedimentary layering seen at the cliff locate in the southern part of the study area, (e) Fault, looking into SE, with an orientation of 222/64, and (f) Sedimentary layering near the study area, looking into NW; measurement of layering plane gives 288/15.

2.5 Resistivity survey

2.5.1 Survey design

Figure 2.8 is an overview map of the study area. Resistivity survey areas are located on a flat area in the quarry. Survey areas are separated into three square grids, as the survey area is designed to cover expected faults. Grid size is 10×10 electrodes with 3 m electrode spacing. Thus, area size is 27×27 m^2 for each square grid. From Figure 2.9 it can be seen that the grid is designed to overlap with nearby grids to get continuous results. Thus, the size of the resistivity survey area is 75×27 m^2. The orientation of the survey grid is 50 degrees from north to x-axis. Corner location for each square grid is shown in Table 2.4.

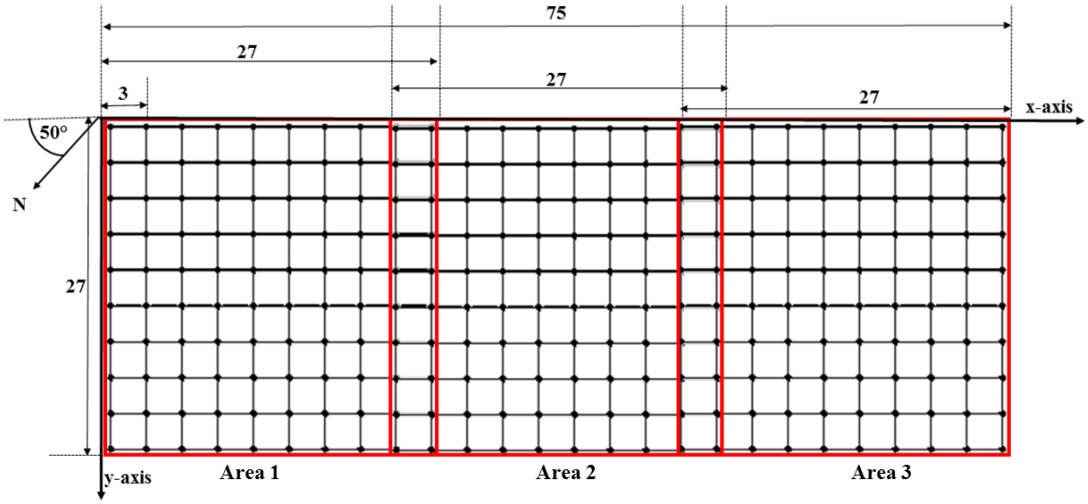

Figure 2.9 Resistivity survey square grids; there is one electrode spacing (3 m) overlap in between Area 1-Area 2 and Area 2-Aare 3.

Table 2.4 Corner location for each square grid.

Area	Corner	UTM (WGS-84)	
		East	North
Area1	0,0	0665795	0748997
	0,27	0665776	0749006
	27,0	0665771	0748971
	27,27	0665757	0748997
Area2	0,0	0665773	0748971
	0,27	0665753	0748993
	27,0	0665752	0748955
	27,27	0665735	0748978
Area3	0,0	0665755	0748958
	0,27	0665736	0748977
	27,0	0665731	0748942
	27,27	0665716	0748965

2.5.2 Data acquisition

Resistivity data are measured by using dipole-dipole array with electrode spacing of 3 m in x- and y-axis and 4.24 m in diagonal axis. Approximately depth of electrodes used for installed into the ground is 15-20 cm. From a 10×10 square grid the maximum n ratio is 7 and the deepest depth of investigation is about 8 m. From Figure 2.10, 840 data are measured in all direction, 280 data in x-axis, 280 data in y-axis and 280 data in both diagonal directions. Measuring time for each area is one to two days.

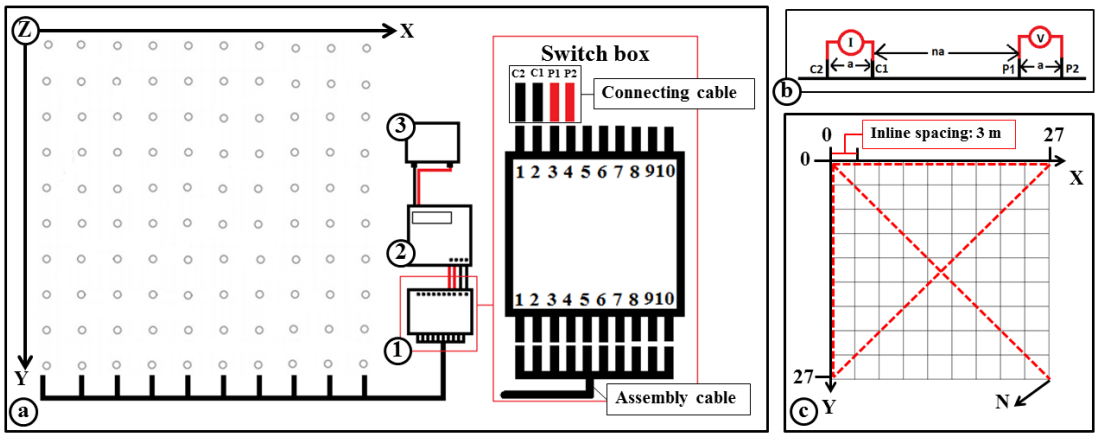

Figure 2.10 Survey design and equipment (a) Diagram of equipment set up consisting of 100 electrodes arranged in a 10×10 square grid, cable, switch box (1), resistivity meter (2) and 12 V battery (3), (b) Arrangement of electrodes in dipole-dipole array, C1-C2 is current electrode pair, P1-P2 is potential electrode pair, a is 3 m inline spacing and n is the ratio varied from 1 to 7 for 10 nodes of electrodes, and (c) Measurement lines, x, y, and both diagonal directions.

CHAPTER 3

RESULTS

Results of this work are displayed as images of resistivity inversion model. These images show the distribution of resistivity values in different sections, horizontal, x-, and y-sections. From the results, higher resistivity areas, lower resistivity areas, and discontinuities in resistivity values are considered to be interesting areas. Higher resistivity area is an area that resistivity value is higher than the surrounding area. Lower resistivity area is an area that resistivity value is lower than the surrounding area. Discontinuity in resistivity values is an area where the resistivity values change siginficantly over a shorter distance. In this work, locations of interesting areas are defined by the location x- and y-axis of the square grid. For example "location 9, 3 on grid" means the interesting area is located at 9 m on x-axis and 3 m on y-axis.

3.1 Testing result

3.1.1 7×7 square grid with spacing 2 m

Figure 3.1, 3.2, and 3.3 show the horizontal, x-, and y-section results of the 3D resistivity test survey on campus of the 7×7 grid with spacing 2 m. Maximum depth of investigation is approximately 3.5 m and resistivity range is in between 30 to 150 Ohm-m. Result show that there is a thin layer of low resistivity located in the upper part at depth from 0 to 0.7 m. Horizontal section show that the trends of resistivity value is higher while getting deeper. The main high resistivity areas located at location 11, 2 on the grid in deeper part at depth 2 to 3 m. Smaller high resistivity areas are found located at location 1, 1 on the grid in the upper part and another one located at location 11, 1 on the grid in a deeper part. Location of the low resistivity area is 9, 3 on the grid at a depth of 1.5 to 3.5 m.

3.1.2 10×10 square grid with spacing 2 m

Figure 3.4, 3.5, and 3.6 show the horizontal, x-, and y-section results of the 3D resistivity test survey on campus of the 10×10 grid with spacing 2 m. Maximum depth of investigation is approximately 6 m and resistivity range is in between 20 to 190 Ohm-m. From the result, a thin layer of lower resistivity is located in the upper part at a depth from 0 to 0.8 m. Results from the horizontal sections show that the trend of resistivity is higher while getting deeper. There is high resistivity area located at the center of the area at location 12, 9 on grid at a depth 0.8 to 1.9 m. Result from x-section show that the lower resistivity layer located at a depth of around 2 to 4 m with a resistivity range between 26 to 45 Ohm-m. Higher resistivity layers are found located in deeper parts, start from a depth of 4 m.

3.1.3 10×10 square grid with spacing 3 m

Figure 3.7, 3.8, and 3.9 show the horizontal, x-, and y-section results of the 3D resistivity test survey on campus of the 10×10 grid with spacing 3 m. Maximum depth of investigation is approximately 9 m and resistivity range is in between 32 to 1,200 Ohm-m. Result show that the trend of resistivity is higher while getting deeper. Result show that the lower resistivity layer is located in the upper part of the area at a depth from 0 to 4 m, while the range of lower resistivity layers is in between 32 to 90 Ohm-m. Higher resistivity layers at deeper parts start from 4 m depth, and the range of higher resistivity layers is between 100 to 1,000 Ohm·m. There are higher resistivity areas located at location 25, 1 on the grid at a depth 1 to 9 m. Another one is located at location 1, 24 on the grid at depth 3 to 9 m.

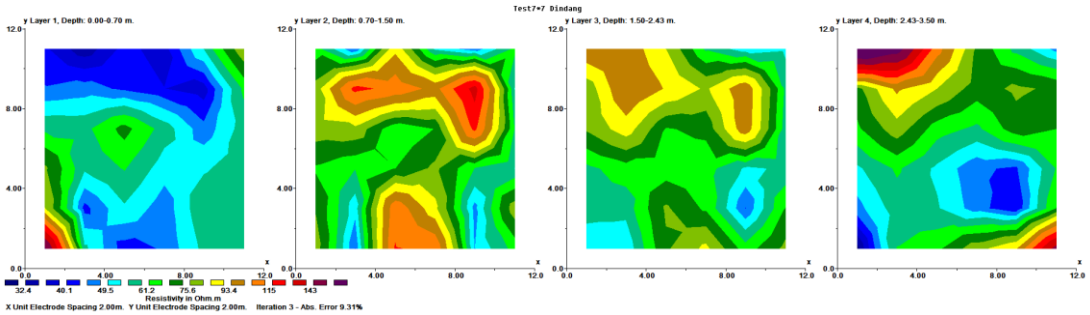

Figure 3.1 Horizontal section result of 7×7 grid with spacing 2 m on testing area.

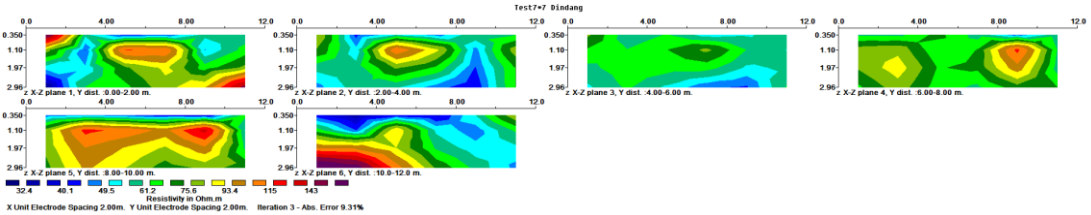

Figure 3.2 X-section result of 7×7 grid with spacing 2 m on testing area

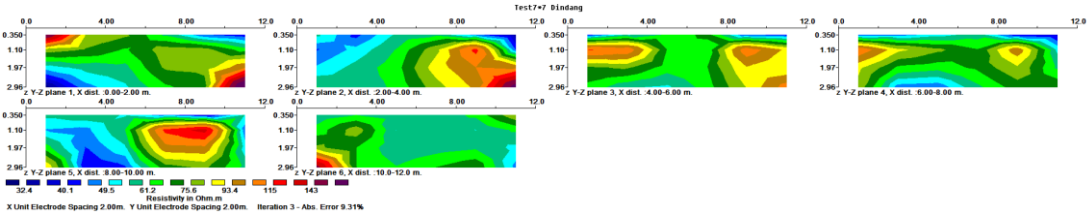

Figure 3.3 Y-section result of 7×7 grid with spacing 2 m on testing area.

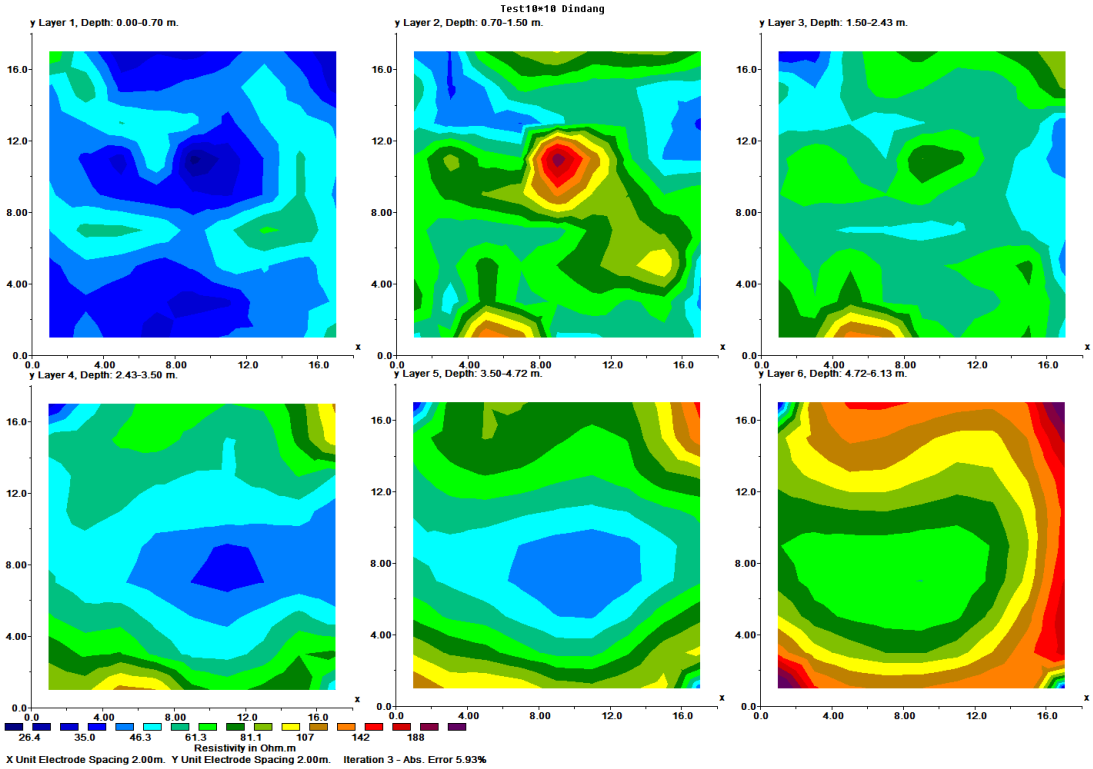

Figure 3.4 Horizontal section result of 10×10 grid with spacing 2 m on testing area.

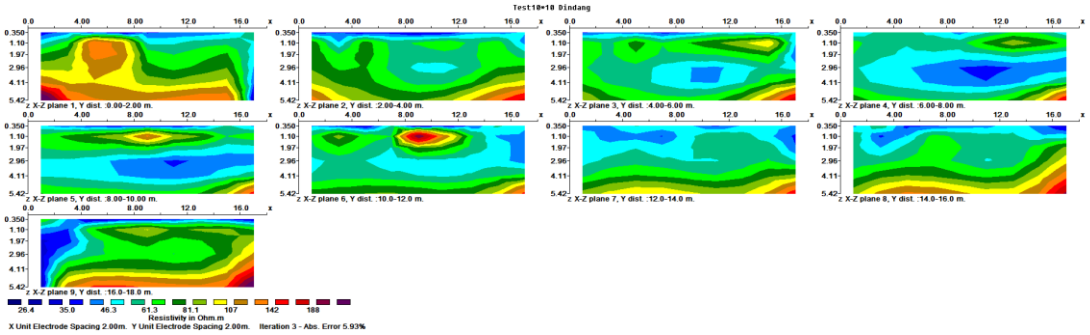

Figure 3.5 X-section result of 10×10 grid with spacing 2 m on testing area.

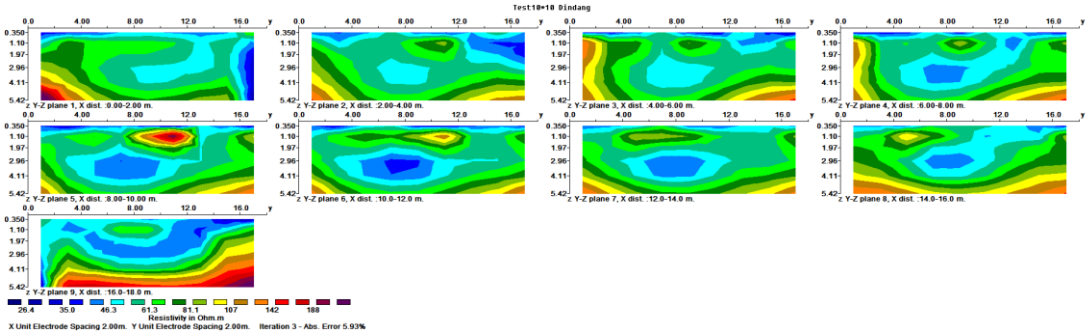

Figure 3.6 Y-section result of 10×10 grid with spacing 2 m on testing area.

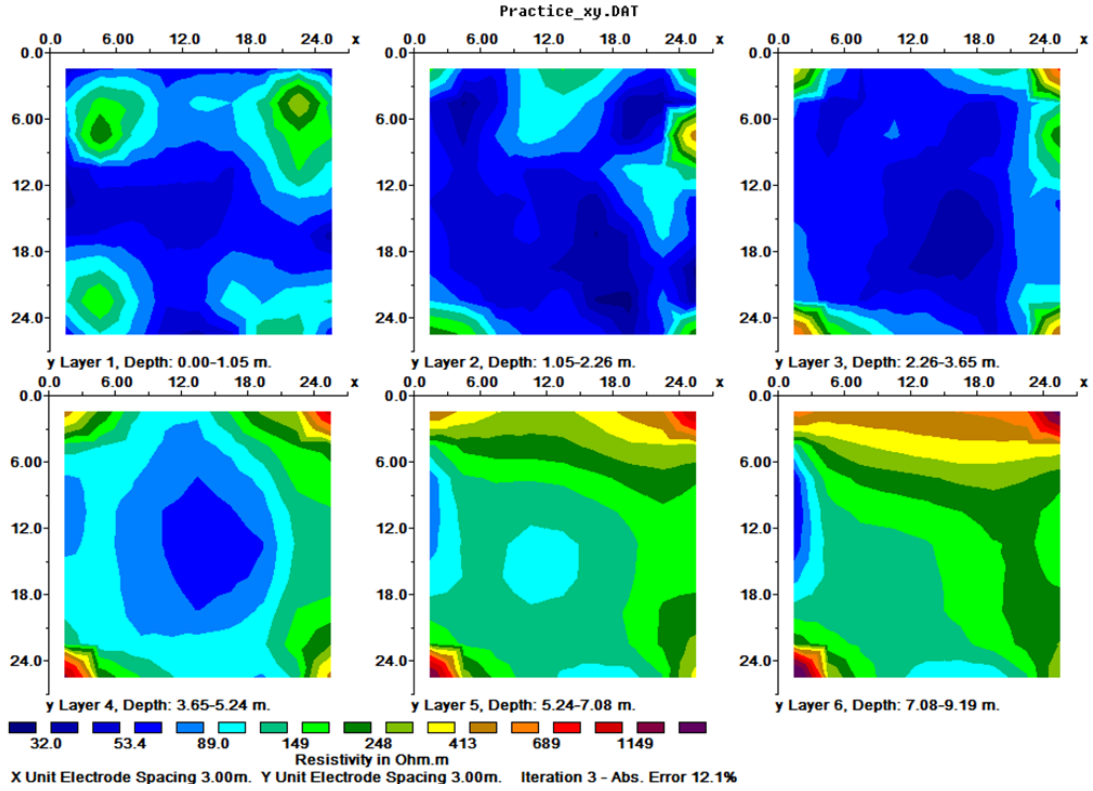

Figure 3.7 Horizontal section result of 10×10 grid with spacing 3 m on testing area.

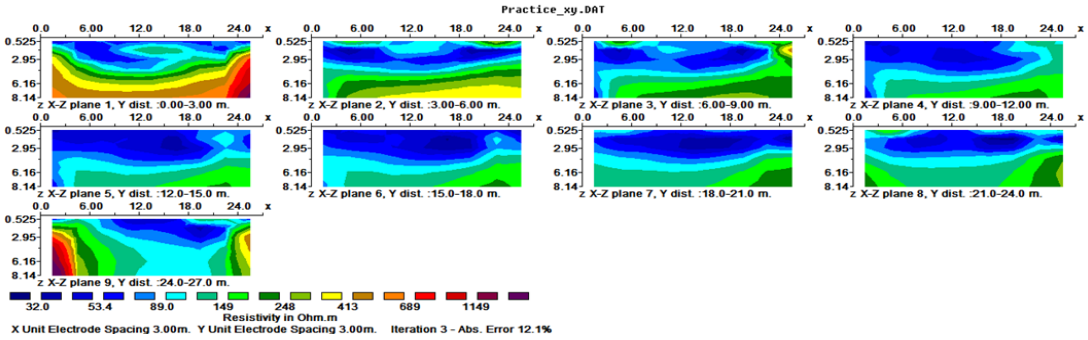

Figure 3.8 X-section result of 10×10 grid with spacing 3 m on testing area.

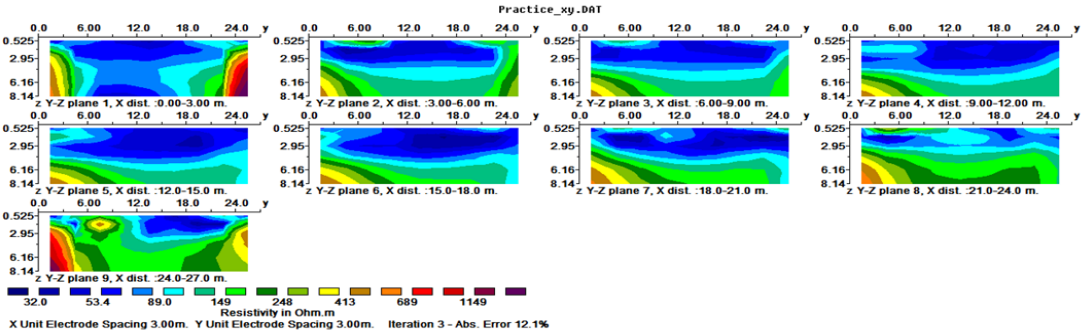

Figure 3.9 Y-section result of 10×10 grid with spacing 3 m on testing area.

In summary, all results from the testing area show the same resistivity pattern; low resistivity area located in the upper part and higher resistivity areas located in deeper part at depth 4 to 5 m. Measure time for 10×10 grid (840) is approximate two days. Data from field can be operated with RES3DINV software. Thus, this acquisition system was ready to be used at the study area.

3.2 Results from study area

Figure 3.10 to 3.18 show the inversion results of the resistivity model of the study area located in an old quarry in the northern part of Sadao district, Songkhla province. The study site is separated into three areas that consist of Area 1, Area 2, and Area 3. All result show the maximum depth of investigation is approximately 9 m and resistivity range is between 20 to 5,000 Ohm-m. In generally, resistivity values can be separated into three areas. A low resistivity areas with resistivity values varying from 10 to 200 Ohm-m, indicated by blue color. Medium resistivity areas with resistivity values varying from 200 to 1,500 Ohm-m, indicated by green and yellow color, and a higher resistivity area that has a resistivity range of 1,500 to 5,000 Ohm-m, indicated by red and purple colors.

3.2.1 Area 1

Figure 3.10, 3.11, and 3.12 show the inversion results of the resistivity survey of Area 1. Horizontal results show that the trend of resistivity values is lower while getting deeper. Result from x- and y-sections show that there are three layers with different resistivity values, medium resistivity layers located in the upper part at depth 0 to 4.5 m and lower resistivity layers located in deeper parts at depth 4.5 to 9 m. A small area of high resistivity layers is found located on top of the medium resistivity layers. Dip direction of the layering is dipping into y-axis direction and a slightly dipping into x-axis direction

Result from Area 1 show that there are three main higher resistivity areas. First area is located at location 1, 1 on the grid at depth 0 to 4 m, second area is located at location 25, 6 on the grid at depth 0 to 4 m, and third area is located at location 21, 20 m on the grid at depth 0 to 4 m. Some discontinuities in the resistivity values are found in the high resistivity layers. First one is located at location 12, 12 on the grid at depth 1 to 3.6 m. Another one is located at location 18, 19 on the grid at depth 1 to 4 m.

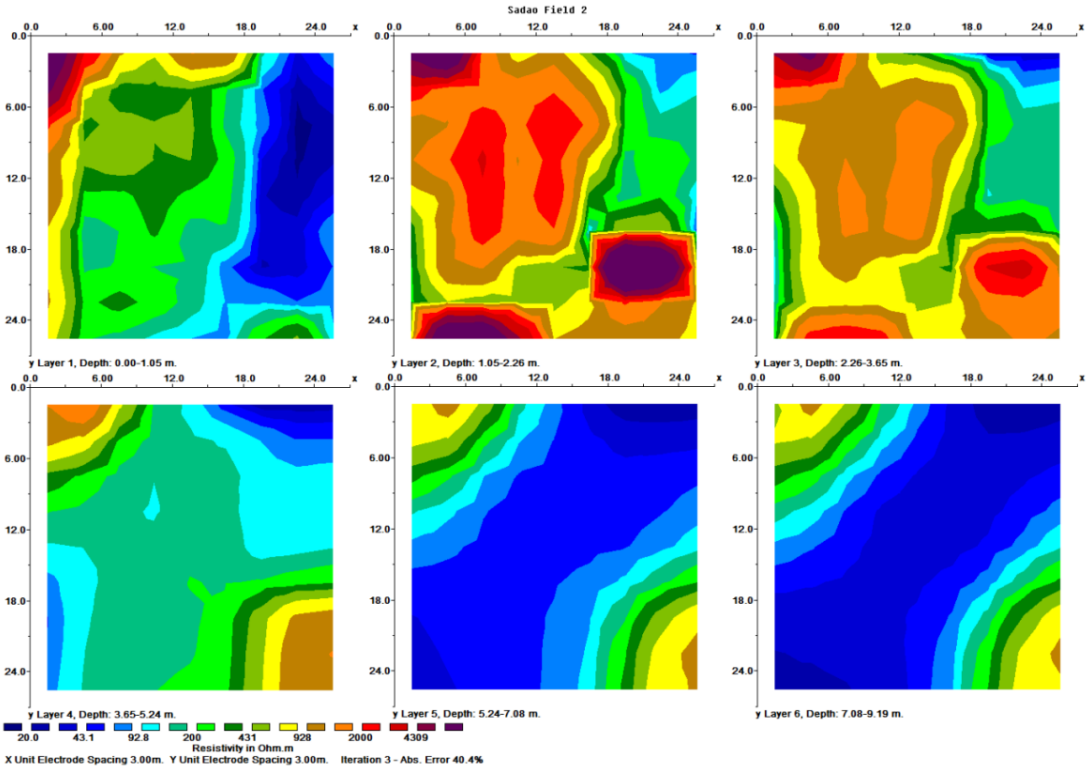

Figure 3.10 Horizontal section result of 10×10 grid with spacing 3 m on Area 1.

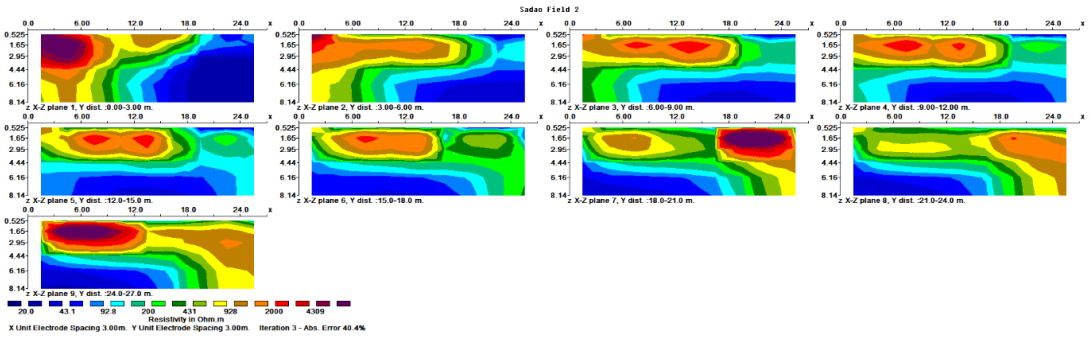

Figure 3.11 X-section result of 10×10 grid with spacing 3 m on Area 1.

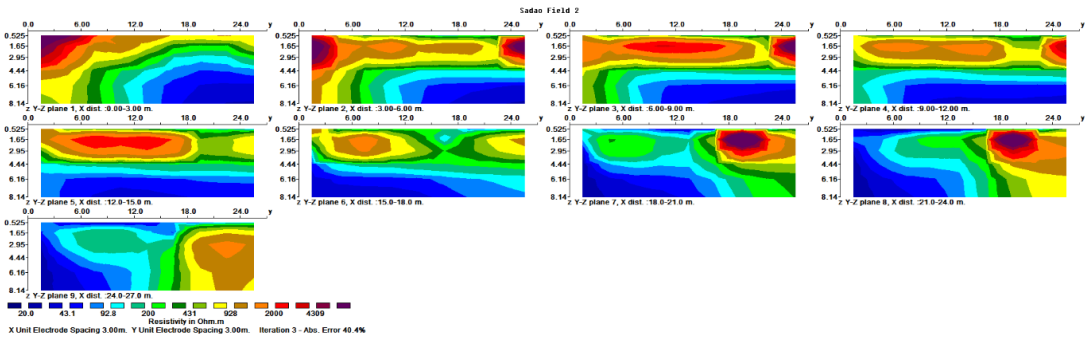

Figure 3.12 Y-section result of 10×10 grid with spacing 3 m on Area 1.

3.2.2 Area 2

Figure 3.13, 3.14, and 3.15 show the inversion results of the resistivity survey of Area 2. Results show that there is a thin layer of low resistivity located in the upper part at depth 0 to 0.7 m. The trend of resistivity value is lower while getting deeper. Similar to result from Area 1, resistivity values can be separated into three areas. Medium resistivity layers located in the upper part and low resistivity layers located in deeper parts. Small areas of high resistivity layers are found located on top of the medium resistivity layers in plane 8 and plane 9 of the x-sections. Results show that layers are dipping into the y-axis direction and slightly dipping into the x-axis direction.

Result revealing that there are two main higher resistivity areas in Area 2. First area is located at location 5, 25 on the grid at depth 1.6 to 3 m and second area is located at location 18, 25 on the grid at depth 1 to 4 m. Some discontinuity in the resistivity values were found in higher and lower resistivity areas. First one is located in the lower resistivity area at location 9, 6 on the grid at depth 1 to 3 m. Second one is located at location 21, 21 on the grid at depth 1 to 4m. Third one is located in higher resistivity areas at location 12, 25 on the grid at depth 1 to 4 m. Finally, the forth is located at location 22, 25 on grid at depth 2 to 5 m.

3.2.3 Area 3

Figure 3.16, 3.17, and 3.18 show the inversion results of the resistivity survey of Area 3. Resistivity values of Area 3 are between 20 to 2,500 Ohm-m. Thus, the resistivity of Area 3 is relatively lower when compared with Area 1 and 2. If considering horizontal results, resistivity values of Area 3 are relatively higher then Area 1 and 2. Result revealing that there is a thin layer of low resistivity located in the upper part at depth 0 to 0.5 m. The trend of resistivity value is lower while getting deeper. Resistivity areas are separated into three layers. High resistivity layers located in the upper part. Medium resistivity layers located in the middle part, and low resistivity layers located in deeper parts. Result from the x-section show that layers are dipping into y-axis direction.

These results show that there are three main higher resistivity areas. First area is located at location 25, 4 on the grid at depth 0.5 to 2.5 m. Second area is located at location 8, 23 on the grid at depth 1 to 3 m. Third area is located at location 19, 25 on the grid at depth 1 to 3 m. There is an area considered to be low resistivity area located at location 22, 18 on the grid at depth 0 to 3 m. Two discontinuities in resistivity values were found in Area 3. First one is located at location 24, 9 on the grid at depth 1 to 2 m, and the second is located at location 15, 24 on grid at depth 1 to 3 m.

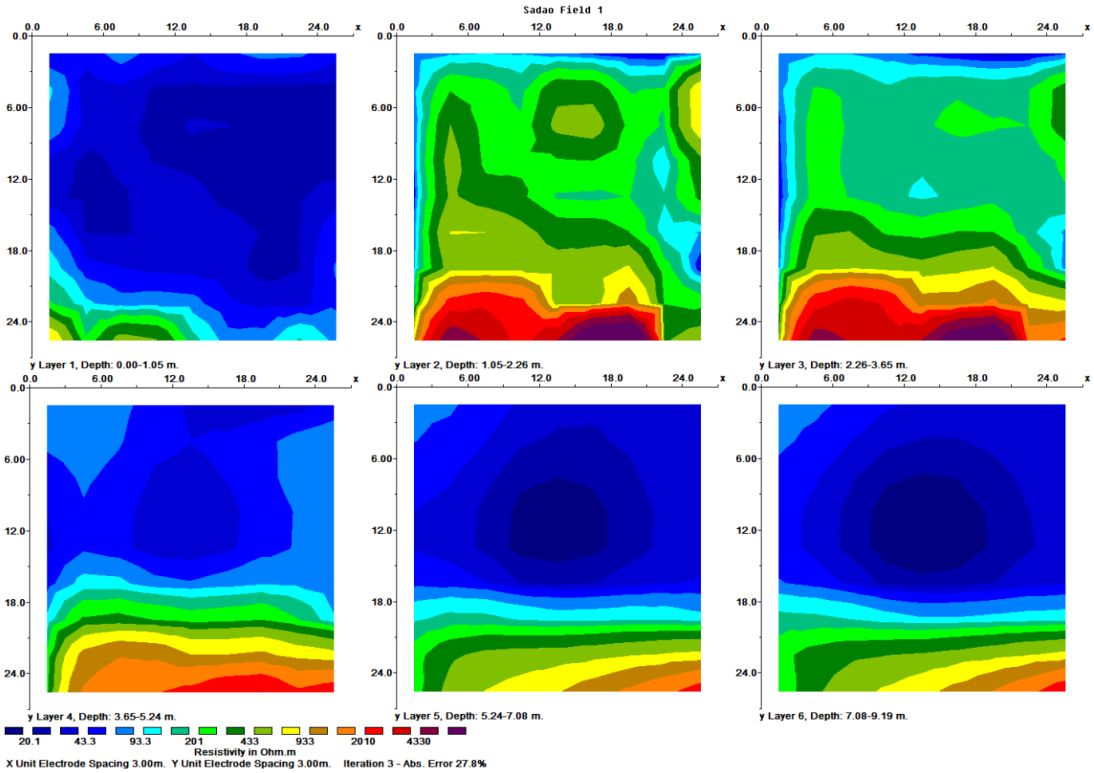

Figure 3.13 Horizontal section result of 10×10 grid with spacing 3 m on Area 2.

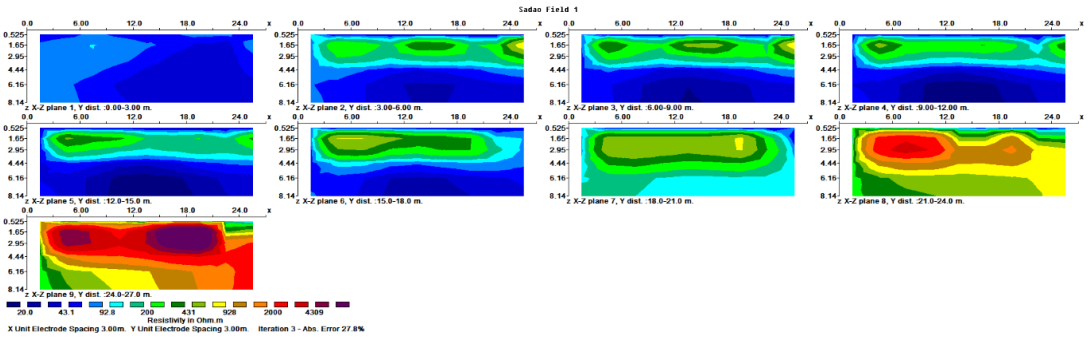

Figure 3.14 X-section result of 10×10 grid with spacing 3 m on Area 2.

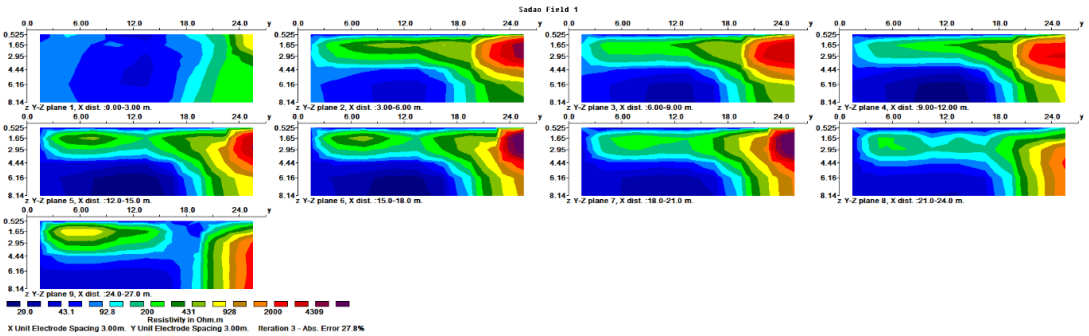

Figure 3.15 Y-section result of 10×10 grid with spacing 3 m on Area 2.

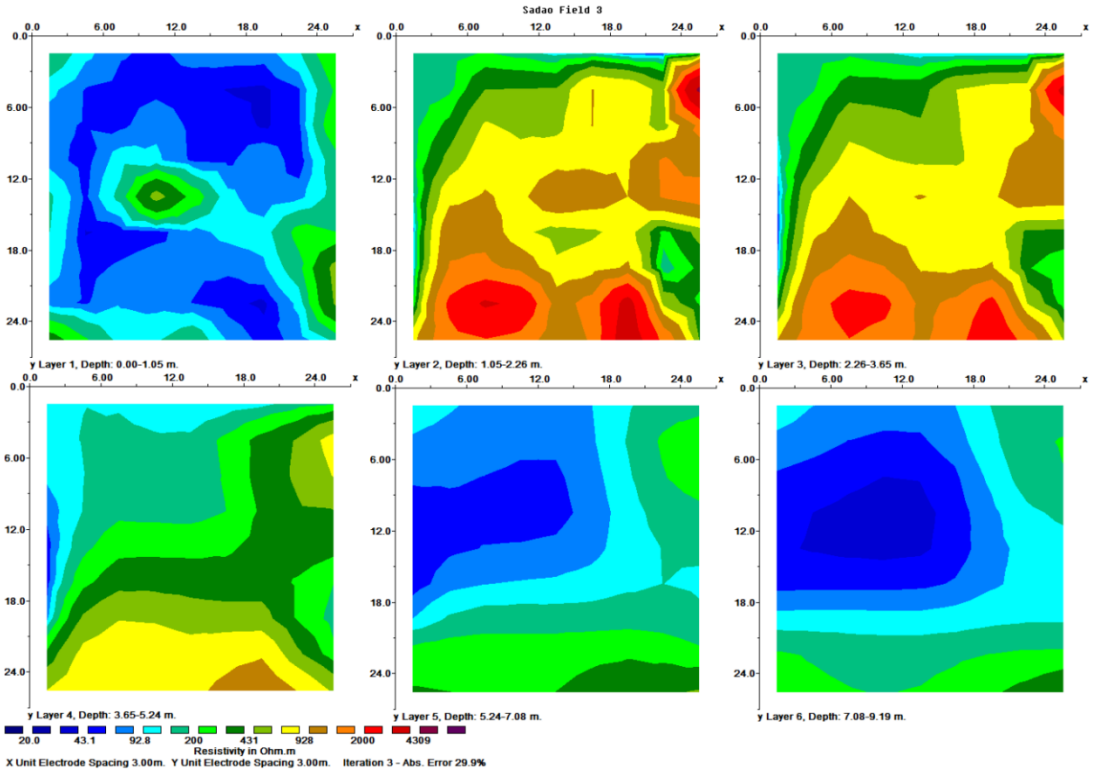

Figure 3.16 Horizontal section result of 10×10 grid with spacing 3 m on Area 3.

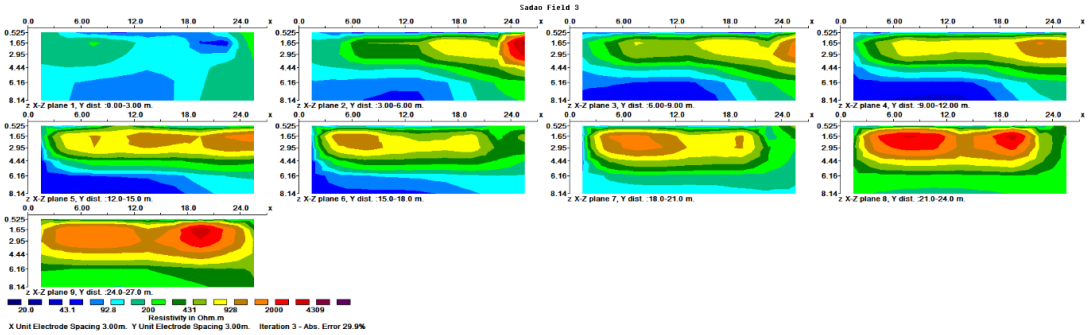

Figure 3.17 X-section result of 10×10 grid with spacing 3 m on Area 3.

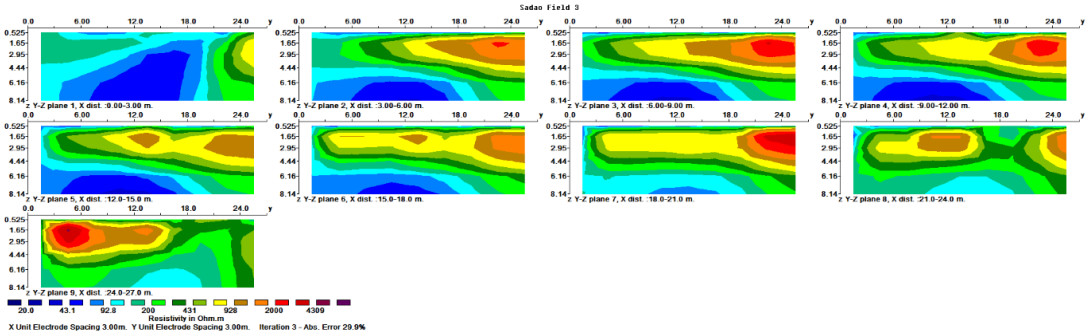

Figure 3.18 Y-section result of 10×10 grid with spacing 3 m on Area 3.

CHAPTER 4

DISCUSSION AND CONCLUSION

4.1 Discussion

The discussion part in this work consist of the identification of faults, identification of sedimentary layering, and a comparison between geology and resistivity data also including a forward modeling discussion.

4.1.1 Sedimentary layering

Sedimentary layer lines are drawn based on differences in resistivity values. From these results resistivity areas can be separated in three zones as show in Figure 4.1. A low resistivity area (L) with resistivity values varying from 20 to 200 ohm-m, indicated by blue colors, a medium resistivity area (M) that has a resistivity range of 200 to 1,500 ohm-m indicated by green and yellow colors, and a high resistivity area with resistivity values varying from 1,500 to 5,000 Ohm-m. Thus, there are three sedimentary layers in this study, as show in Figure 4.2, 4.3, and 4.4. There are three types of layer boundaries in this study, low-medium layer boundary (LM), medium-high layer boundary (MH), and low-high layer boundary (LH).

Sedimentary layer lines are drawn in the horizontal, x-, and y-section results. Then, dip direction and dip angle of sedimentary layer line are measured. Dip directions were measured from horizontal result, and dip angles were measured from y-section results. Table 4.1 shows that the dip direction of the low-medium layer boundary is 320-330 degrees from north and dip angle is 12-28 degrees from surface. Dip direction of medium-high layer boundary is 326-330 degrees from north and dip angle is 20-29 degrees from surface, and dip angle of low-high layer boundary is 5-9 degrees from surface, but the dip directions cannot be identified from these results. Generally, dip direction should be similar to other layers in same study area; therefore, dip directions of low-high layer boundaries are dipping into north-west direction.

4.1.2 Faults

The consideration of fault lines in this area is based on the discontinuity of resistivity values. As faults are crack-like planes in the subsurface that can separate sedimentary layers and by this they create discontinuities in resistivity values. Similar to the discussion on sedimentary layering, dip direction and dip angle of fault lines are measured. Dip directions of fault lines are measured from horizontal section results and dip angles of fault are measured from x-section results.

Result show that there are four fault planes in the study area. First fault (F1) line located at Area 1 with dip direction 219-220 degrees from north and dip angle 62-65 degrees from surface. Second and third fault are located in Area 2. Dip direction of

second fault (F2) is 220-222 degrees from north and dip angle is 58-63 degrees from surface. Dip direction of third fault (F3) is 227-228 degrees from north and dip angle is 79-82 degrees from surface. Finally, the forth fault (F4) is located in Area 3 with a dip direction of 70-73 degrees from north and dip angle is 82-84 degrees from surface, as show in Table 4.2.

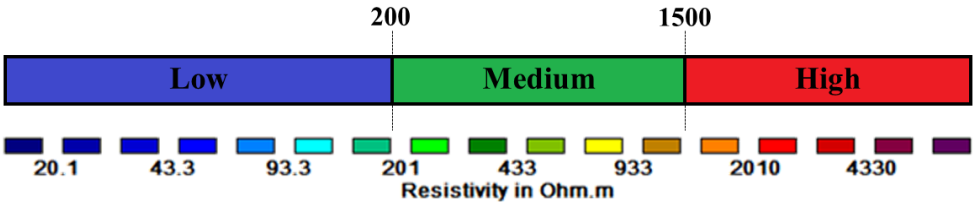

Figure 4.1 Resistivity range is separated into three zones. Low resistivity area (L) with resistivity values varying from 20 to 200 ohm-m, indicated by blue colors. A medium resistivity area (M) that has a resistivity range of 200 to 1,500 ohm-m, indicated by green and yellow colors, and a high resistivity area with resistivity value varying from 1,500 to 5,000 Ohm-m.

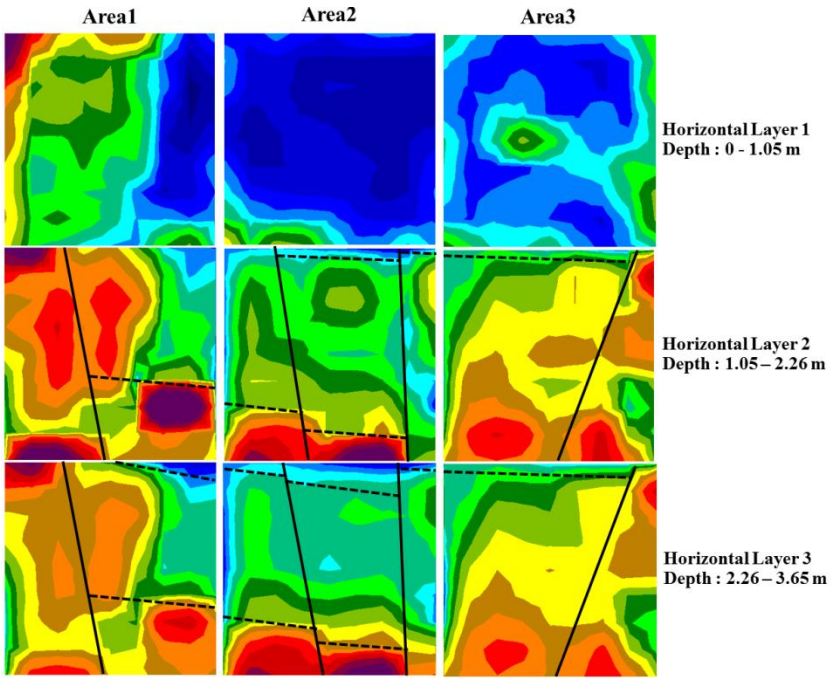

Figure 4.2-1 Horizontal section result Layer 1, 2, and 3. Black solid lines are fault lines and dotted lines are sedimentary layers.

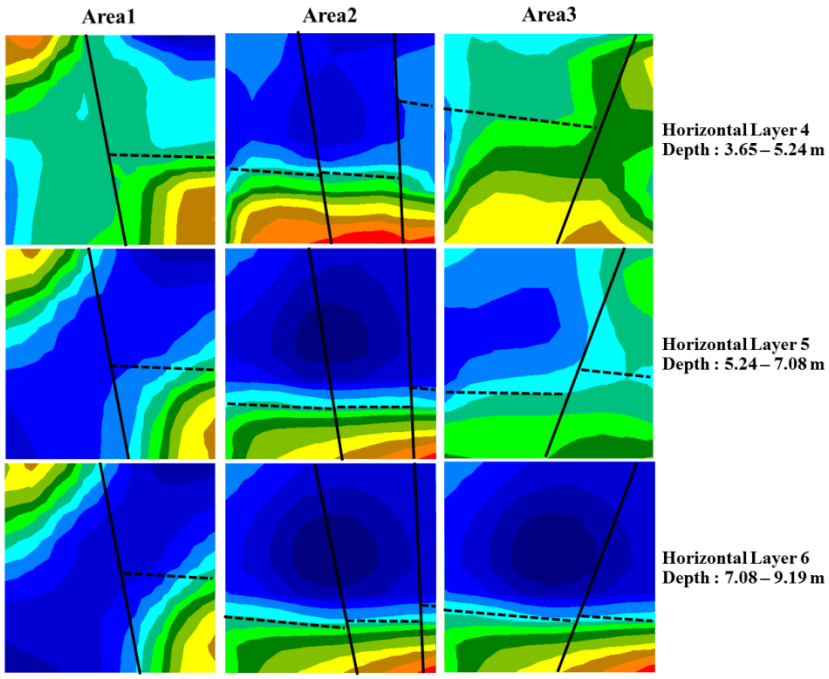

Figure 4.2-2 Horizontal section result Layer 4, 5, and 6. Black solid lines are fault lines and dotted lines are sedimentary layers.

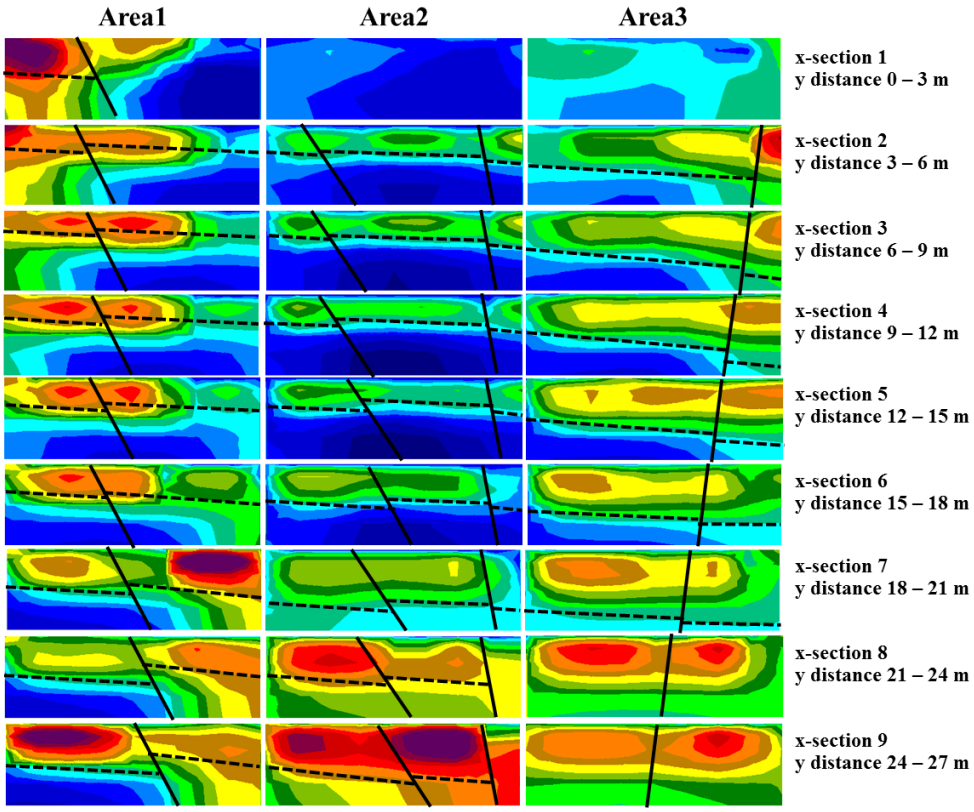

Figure 4.3 X-section result of section 1 to 9. Black solid lines are fault lines and dotted lines are sedimentary layers.

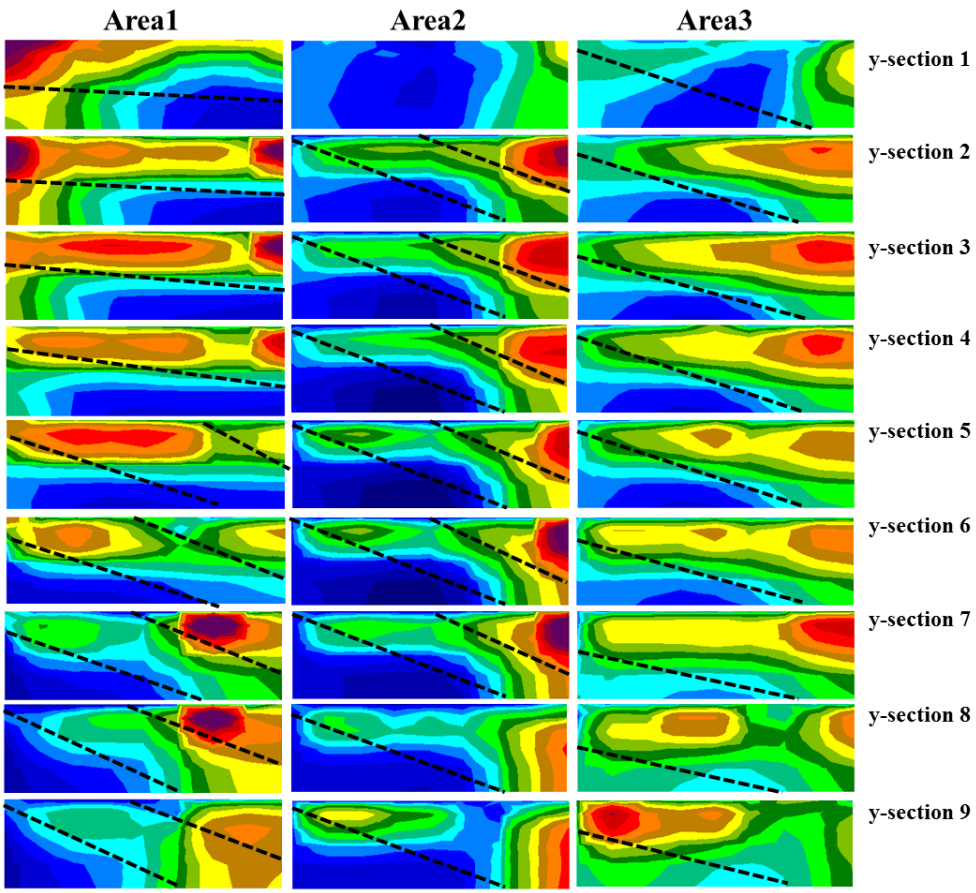

Figure 4.4 Y-section results of section 1 to 9. Black lines are fault lines and dotted lines are sedimentary layers.

Table 4.1 Dip direction and dip angle of sedimentary layer boundary.

Boundary	Low-Medium (LM)	Medium-high (MH)	Low-high (LH)
Dip direction	320-330	326-330	N/A
Dip angle	22-28	20-29	5-9

Table 4.2 Dip direction and dip angle of fault lines.

Fault	Fault1 (F1)	Fault2 (F2)	Fault3 (F3)	Fault4 (F4)
Dip direction	219-220	220-222	227-228	70-73
Dip angle	62-65	58-63	79-82	82-84

4.1.3 Comparison between geology and resistivity data

Based on the geological information the low resistivity layer can be considered to be siltstone mixed with sandstone, the medium resistivity layer is sandstone, and the high resistivity layer is conglomerate, because the porosity and permeability of these sedimentary rocks from low to high are siltstone, sandstone, and conglomerate, respectively. Figure 4.5 shows the data correlation between geological and resistivity.

Figure 4.6 show that the measurements of dip angle and dip direction of sedimentary layer from resistivity data correlates with data from geological surveys. Fault 2 (F2) identified from resistivity data can be correlated with the expected fault that was measured from geological survey station S1. Moreover, Fault 4 (F4) can be correlated to the fault plane measured at geological survey station S2.

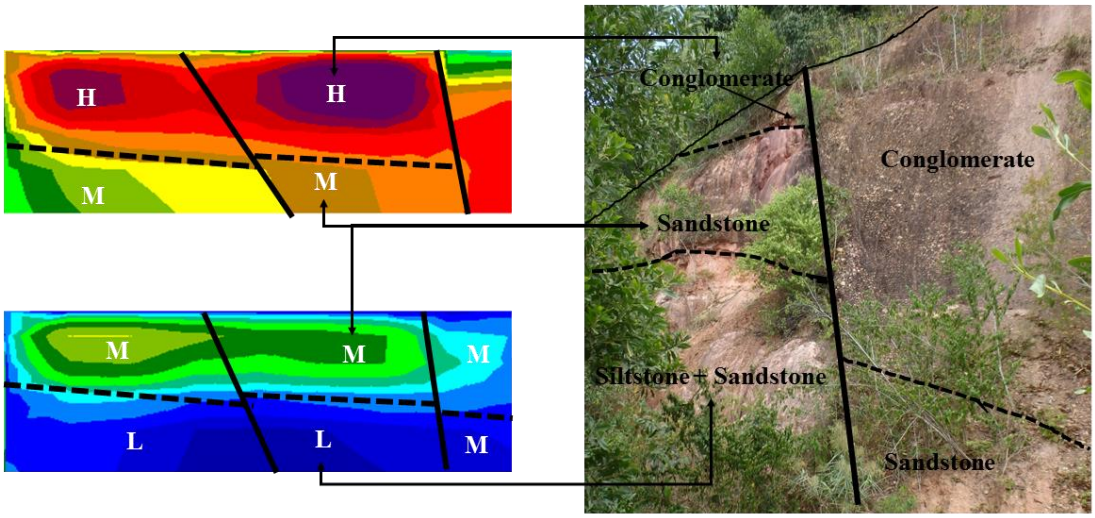

Figure 4.5 Data correlation between geological and resistivity: Low resistivity is siltstone mixed with sandstone, medium resistivity is sandstone, and high resistivity is conglomerate.

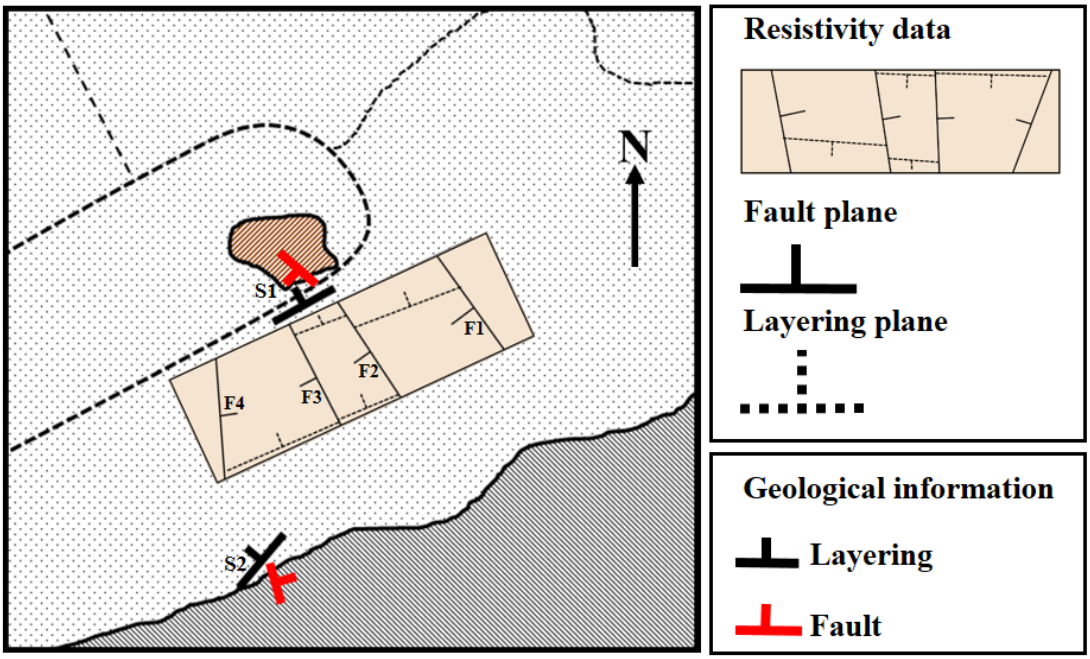

Figure 4.6 Overview map of the study area including geological information and resistivity data.

4.1.4 Comparison to large scale geological structures

The study area is located in the southern part of Hat Yai basin. Hat Yai Basin is a sedimentary basin in peninsular Thailand. The approximately location of Hat Yai basin is between UTM 640000 E and 680000 E and between UTM 740000 N and 810000 N. Geologically, Hat Yai basin is flanked to the east and west by granitic rocks intruding into Carboniferous and Triassic sedimentary and metamorphic rocks, which form the basement of the basin. Carboniferous rocks in this basin consist of sandstone, siltstone, shale, mudstone, cherts, and argillite, while Triassic rocks consist of sandstone, siltstone, mudstone, conglomerate, massive limestone and cherts. The granites in this basin are late Triassic-early Jurassic and late Cretaceous-early Quaternary. Figure 4.7a shows the structure of the horst and graben structure of Hat Yai basin. Generally, the structure of Hat Yai basin is considered to be a graben, while the hill ranges and the small basins in eastern of the graben are parts of a horst (Lohawijarn, 2005).

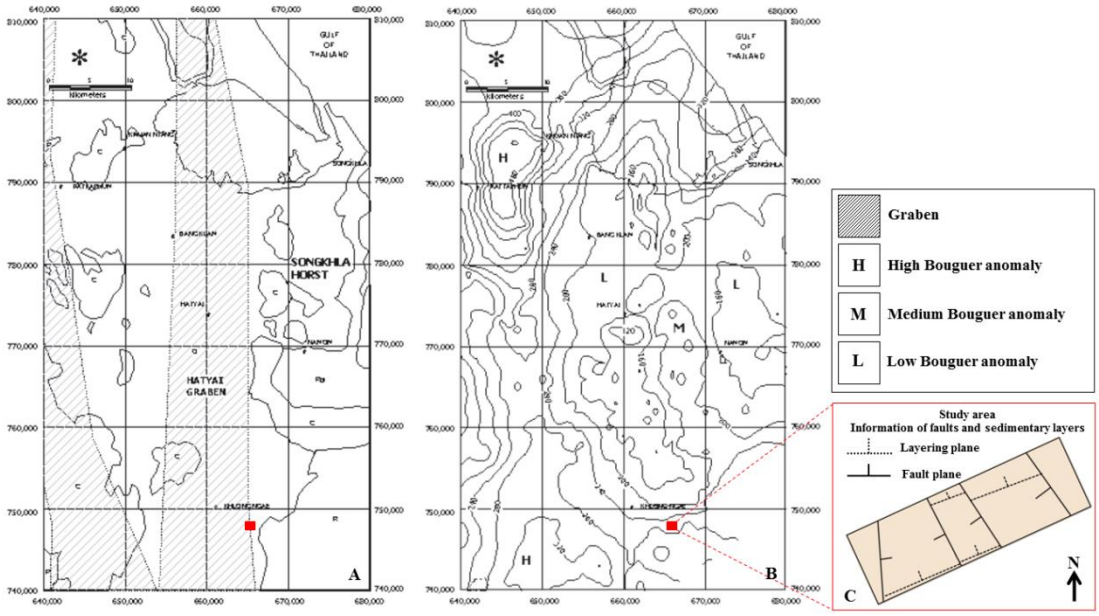

Figure 4.7 Geological structure of Hat Yai basin with horst and graben, A; Bouguer anomaly contour map in $\mu m/s^2$, B; and C shows the information of sedimentary layers and faults in the study area.

Figure 4.7b presents the Bouguer anomaly contour map in $\mu m/s^2$ while Figure 4.7c provides information of sedimentary layers and faults in the study area, based on results from resistivity surveys of this study. Results show that the study area where the 3D resistivity surveys were carried out is located in on a high-low anomaly boundary which is considered to be the southern boundary of the basin. This area is also the area of a horst and graben boundary. Results show that faults in the study area arrange in north-south and northwest-southeast direction correlated with the horst and

graben boundary, which in general is arranged in north-south direction. Dip direction of sedimentary layers, which are dipping to the north is possible because the center of basin located in northern part of the study area.

4.1.5 Forward Modeling

In this work, forward modeling is made to support the interpretation of the measures results. Figure 4.8 shows the procedures of forward modeling, starting with the design of a resistivity model. In general, a resistivity model consists of several horizontal sections of different depth. Each horizontal section is sub-divided into several blocks. A defined resistivity value is added into every block in every section. After that this resistivity model is saved in MOD file. MOD file format and then processed by RES3DMOD modeling software. The apparent resistivity values of the defined resistivity model are calculated from RES3DMOD. After that, these apparent resistivity data are exported in DAT file format. Finally, the DAT file is processed to create an inversion model to see the resistivity model from the original defined resistivity model by RES3DINV software.

In this work, two resistivity models are used to study. The structures of the resistivity models are designed to be similar with structures of the study area. The first model shown in Figure 4.9 is a resistivity model of two dipping layers. Resistivity of the top layer is 500 Ohm-m and resistivity of bottom layer is 50 Ohm-m. Layers are dipping into y-axis direction. The second model shown in Figure 4.10 is a resistivity model of two dipping layers including a fault. Resistivity of each layer is similar to the first model. The fault is designed to dip into x-axis direction. The fault separated the model into two plates, a left side plate and a right plate. The right side plate is designed to a move a short distance up with respect to the x-axis.

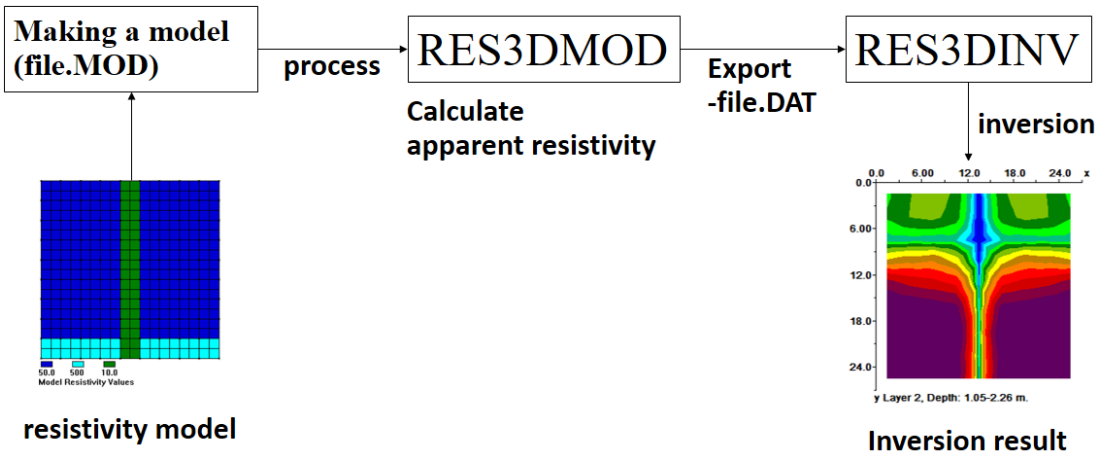

Figure 4.8 Procedures of forward modeling, consisting of making a resistivity model, calculate apparent resistivity, and export file to operate with inversion software.

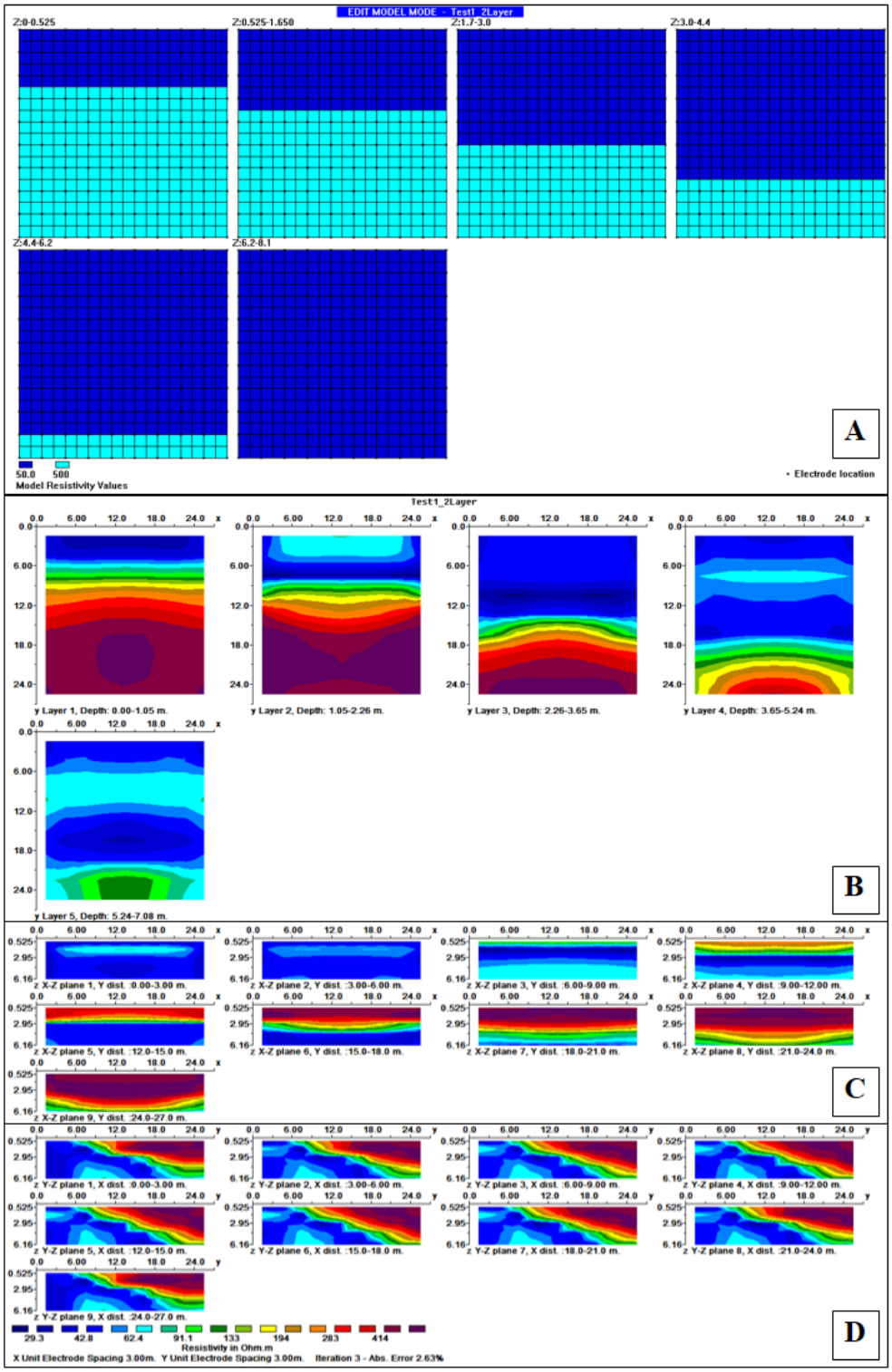

Figure 4.9 (A) resistivity model of two dipping layers; (B) inversion results displayed in horizontal section; (C) inversion result displayed in x-section, and (D) inversion result displayed in y-section

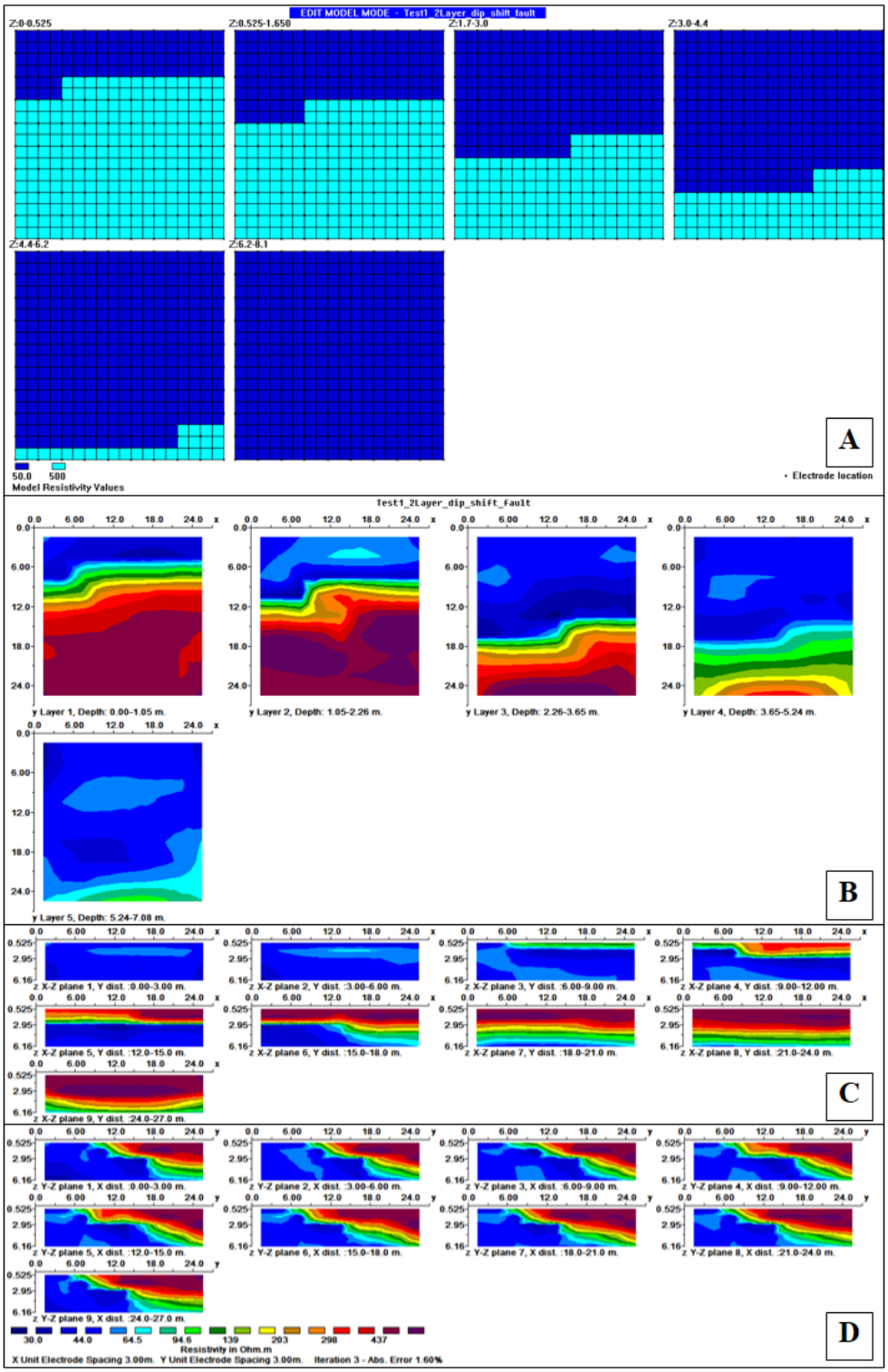

Figure 4.10 (A) resistivity model of two dipping layers including one fault; (B) inversion result displayed in horizontal section; (C) inversion result displayed in x-section, and (D) inversion result displayed in y-section.

The inversion results of these models show that the dipping layers can be found from the y-section. The dip direction and dip angle of the layers can be measured from the horizontal section and y-section, respectively. In the second model, the fault and plate shift can be found in the horizontal section and in the x-section. Considering the horizontal section, the fault can create a discontinuity in resistivity values. Thus, dip direction and plate shift can be identified from the horizontal section. Dip angle can be measured from x-direction. Finally, results of forward modeling are similar to results from the field survey. Thus, the identification of layers and faults based-on these forward modeling can be used for interpreting result from study area in this work.

4.1.6 Error of inversion results

Error of inversion results of test area for Test1, Test2 and Test3 is 9.31%, 5.93%, and 12.1%, respectively. And error of inversion results of study area for Area 1, Area 2 and Area 3 is 40.4%, 27.8%, and 29.9%, respectively. The results show that the errors of the inversion results from test area are lower than results from study area. In this work, the increase of error values is assumed from two possible factors. First, the size of the study area increased with area versus test results. Second, the complexity of the area, because the geological structures of study area show more complexity than in the test area, thus results from the study area have a higher error value than the test area.

4.2 Conclusions

4.2.1 Modeling of geological structure

Resistivity results show that there is a thin layer of low resistivity on the top of the subsurface. The approximate depth of this thin layer is 0.7 m. In this study, a thin layer of low resistivity is considered to be top soil. There are many grasses and bushes covering the surfaces in the study area. Grasses and bushes over subsurface can keep the moisture in the top soil. This process can cause a thin layer of low resistivity in the upper part of the subsurface. Figure 4.11 shows a comparison between surface conditions and first layer of horizontal resistivity result. The comparison shows that the boundary of the low resistivity layer can be correlated with the slope on the surface. This correlation can be considered that the sedimentary layer is already found on the left side of the slope.

Figure 4.12 is structural model of the subsurface of the study area. Sedimentary layers and faults are identified from resistivity results show in Figure 4.12a and b. The resistivity model of the subsurface which consists of sedimentary layers and fault information was interpreted including geological data as show in Figure 4.12b and c. Finally, a structural model of the subsurface is created as show in Figure 4.12c.

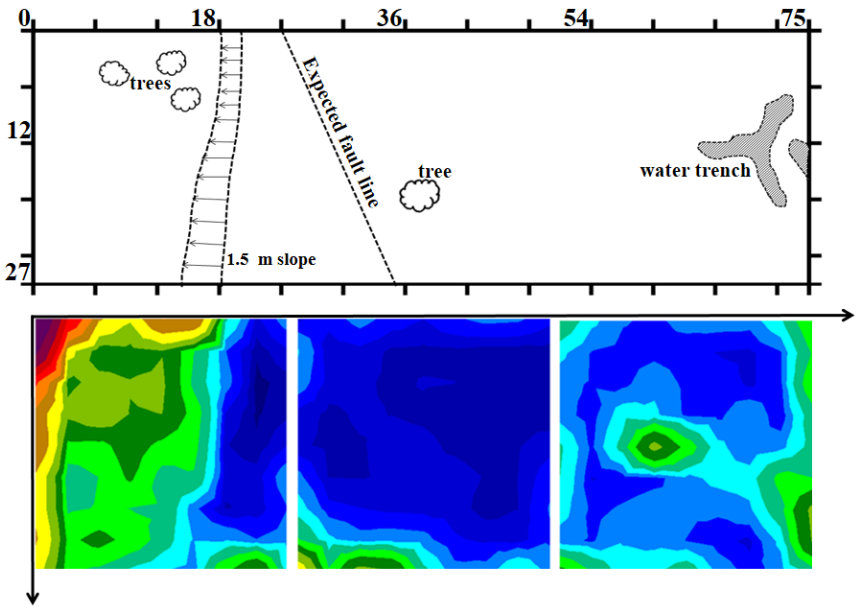

Figure 4.11 Comparison between surface conditions and first layer of horizontal resistivity result.

The structural model contains information of sedimentary layering and faults. Sedimentary layers in this area are dipping into north-west direction; the approximate dip direction is 325 degrees from north. Dip angle of the sedimentary layers is 25 degrees from surface. High resistivity layer is considered to be conglomerate, medium resistivity layer is sandstone and low resistivity is siltstone mixed with sandstone. Result show that the information of layering can be well correlated with geological data. There are four faults in this study. From the results, two faults have similar geological data, F2 and F4. Moreover, two more faults are found and identified from resistivity results, F1 and F3. Detecting F1 and F3 proves that a 3D resistivity survey can be used to determine geological structures in the subsurface beyond geological surface mapping (Figure 4.13).

4.2.2 Data acquisition system

Conclusion also can be drawn regarding the 3D resistivity acquisition system. Results presented here show that it is possible to make a 3D resistivity survey by using a single-channel resistivity meter with a switch box and cable assembly instead of a multi-channel resistivity meter that still requires high survey costs nowadays. From this work, the data acquisition system can measure 840 data points in one to two days depending on survey area environment and the survey costs are actually lower than using a multi-channel resistivity meter.

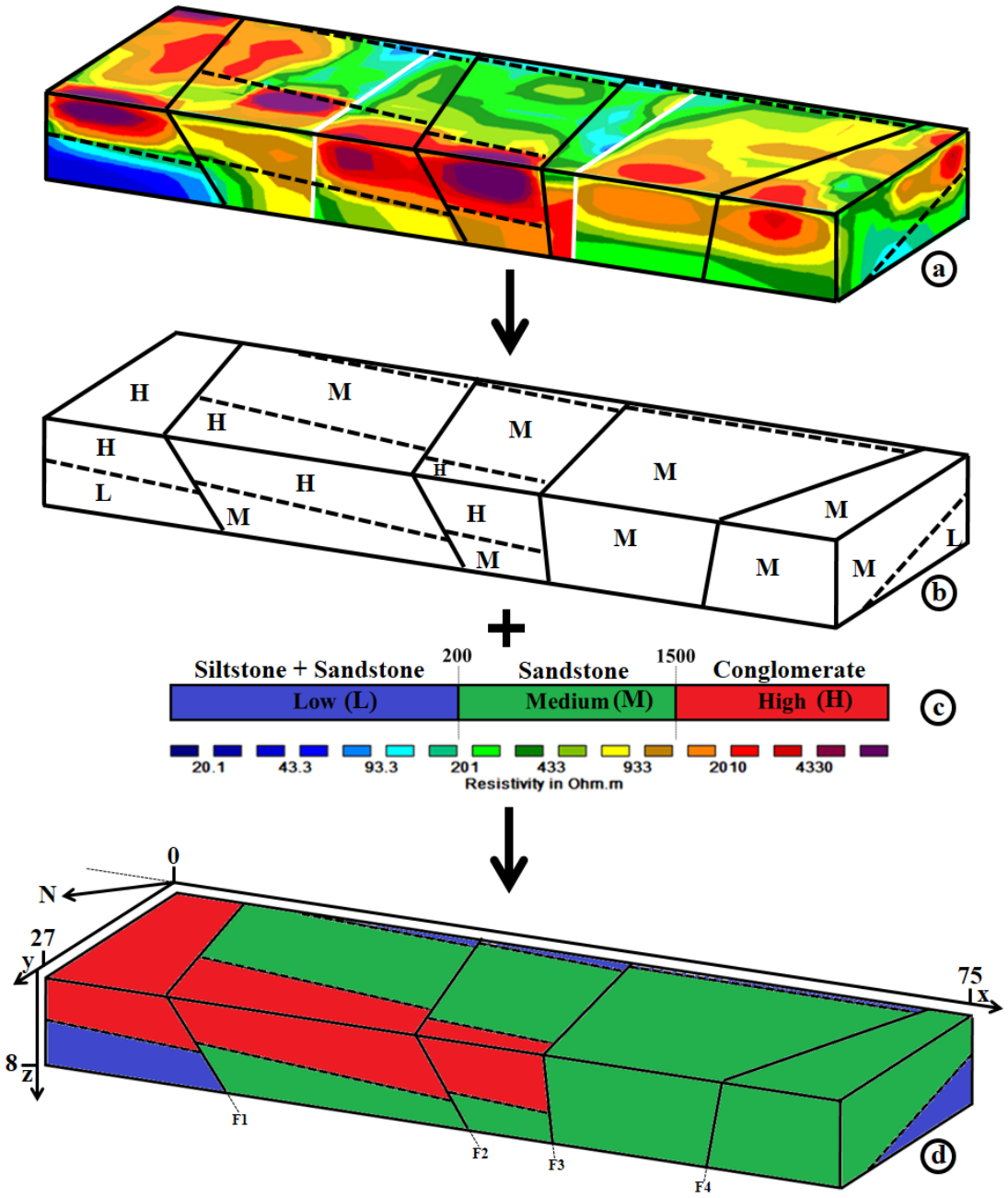

Figure 4.12 Co-interpretation between resistivity data and geological data (a), and (b) identification of sedimentary layers and faults from resistivity results, (c) resistivity range including geological information, and (d) model of subsurface structure in study area.

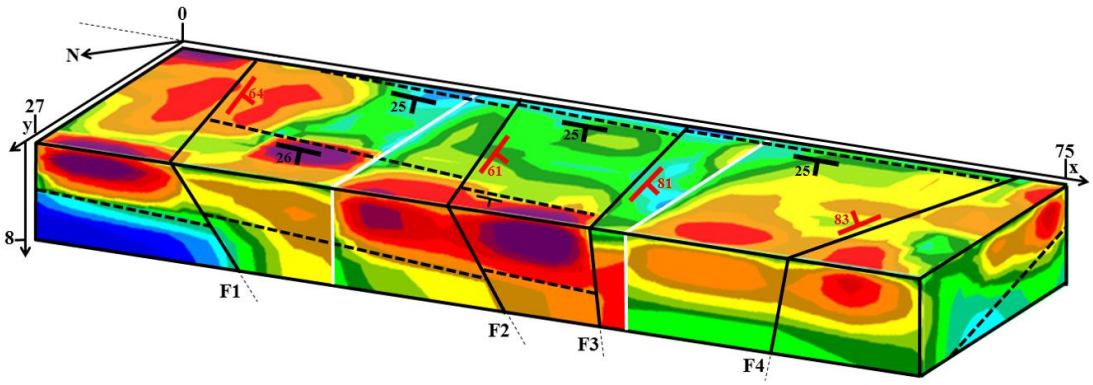

Figure 4.13 Resistivity model of the study area including information of sedimentary layers and faults, sedimentary layers indicated by black strike-dip symbols and faults indicated by red strike-dip symbols.

REFERENCES

Amato, M., Bitella, G., Rossi, R., Gomez, J.A., Lovelli, S., Gomes, J.J.F. (2009). Multi-electrode 3D resistivity imaging of alfalfa root zone. European Journal of Agronomy, 312-222.

Anomohanran , O., Ofomola, M.O., Okocha, F.O. (2017). Investigation of groundwater in parts of Ndokwa District in Nigeria using geophysical logging and electrical resistivity methods: Implications for groundwater exploration. African Earth Sciences, 108-116

Asfahani, J. (2016). Hydraulic parameters estimation by using an approach based on vertical electrical soundings (VES) in the semi-arid Khanasser valley region, Syria. African Earth Sciences, 196-204.

Ayolabi, E.A., Folorunso, A.F., Jegede, O.E. (2012). An application of 2D electrical resistivity tomography in geotechnical investigations of foundation defects: A case study. Geology and Mining Research, 142-151.

Badmus,.B.S., Akinyemi, O.D., Olowofela.J.A., Folarin, G.M. (2012). 3D Electrical Resistivity Tomography Survey for the Basement of the Abeokuta Terrain of Southwestern Nigeria. Geology Society of India, 845-854.

Bermejo, L., Ortega, A.I., Guerin, R., Benito-Calvo, A., Perez-Gonzalez, A., Pares, J.M., Aracil, E., Bermúdez, J.M., Carbonell, E. (2016). 2D and 3D ERT imaging for identifying karst morphologies in the archaeological sites of Gran Dolina and Galería Complex (Sierra de Atapuerca, Burgos, Spain). Quaternary International, 1-9.

Bichet, V., Grisey, E., Aleya, L. (2016). Spatial characterization of leachate plume using electrical resistivity tomography in a landfill composed of old and new cells (Belfort, France). Engineering Geology, 61-73.

Boaga, J., Rossi, M., Cassiani, G. (2013). Monitoring soil-plant interactions in an apple orchard using 3D electrical resistivity tomography. Procedia Environmental Sciences, 394-402.

Bowen, R. 1986. Groundwater 2nd ed., Elsevier science publishing, New York, U.S.A., pp 50-51.

Cardarelli, E., De Donno, G. (2017). Multidimensional electrical resistivity survey for bedrock detection at the Rieti Plain (Central Italy). Applied Geophysics, 77-87.

Chabaane, A., Redhaounia, B., Gabtni, H. (2017). Combined application of vertical electrical sounding and 2D electrical resistivity imaging for geothermal groundwater characterization: Hammam Sayala hot spring case study (NW Tunisia). Journal of African Earth Sciences, 292-298.

Chambers, J.E., Gunn, D.A., Wilkinson, W.B., Meldrum, P.I., Haslam, E., Holyoake, S., Kuras, O., Kirkham, M., Merrit, A., Wragg, J. (2014). 4D electrical resistivity tomography monitoring of soil moisture dynamics in an operational railway embankment. Near Surface Geophysics, 61-72.

Chambers, J.E., Wilkinson, W.B., Kuras, O., Ford, J.R., Gunn, D.A., Meldrum, P.I., Pennington, C.V.L., Weller, A.L., Hobbs, P.R.N., Ogilvy, R.D. (2011). Geomorphology, 472-482.

Chernicoff, S. 1999. Geology 2nd ed., Houghton Mifflin Company, Massachusetts, U.S.A., pp 152-179.

Christopher, P., Jason, I.G., Marios, K., Panagiotis, T., Antonios, G. (2014) Evaluating four-dimensional time-lapse electrical resistivity tomography for monitoring DNAPL source zone remediation. Contaminant Hydrology, 27-46.

Denke, S., Dürrast, H. (2010). Determining the location of shallow fault using geoelectric profiling. BSc Project, Department of Physics, Prince of Songkla University, Thailand.

Di Maio, R., Fais, S., Ligas, P., Piegari, E., Raga, R., Cossu, S. (2018). 3D geophysical imaging for site-specific characterization plan of an old landfill. Waste Management, 629-642.

Earle, S. 2015. Physical Geology, BC Open Textbook Project, British Columbia, Canada, pp 335-354.

Gance, J., Malet, J, P., Supper, R., Sailhac, P., Ottowitz, D., Jochum, B. (2016). Permanent electrical resistivity measurements for monitoring water circulation in clayey landslides. Applied Geophysics, 98-115.

Giampaolo, V., Capozzoli, L., Grimaldi, S., Rizzo, E. (2016). Sinkhole risk assessment by ERT: The case study of Sirino Lake (Basilicata, Italy). Geomorphology, 1-9.

Kearey, P., Brooks, M. and Hill, I. 2002. An introduction to geophysics exploration 3rd ed., Blackwell science Ltd., Oxford, England, pp 183-185.

Khalil, M.A., Santos, F.A.M. (2013). 2D and 3D resistivity inversion of Schlumberger vertical electrical soundings in Wadi El Natrun, Egypt: A case study. Applied Geophysics, 116-124.

Kneisel, C., Emmert, A., Kästl, J. (2014). Application of 3D electrical resistivity imaging for mapping frozen ground conditions exemplified by three case studies. Geomorphology, 71-82.

Lebourg, T., Hernandez, M., Zerathe, S., El Bedoui, S., Jomard, H., Fresia, B. (2010). Landslides triggered factors analysed by time lapse electrical survey and multidimensional statistical approach. Engineering Geology, 238-250.

Ling, C., Xu, Q., Zhang, Q., Ran, J. Hongbin, L.V. (2016) Application of electrical resistivity tomography for investigating the internal structure of a translational landslide and characterizing its groundwater circulation (Kualiangzi landslide, Southwest China). Applied Geophysics, 154-162.

Lohawijarn, W. (2005). Potential ground water resources of Hat Yai Basin in Peninsular Thailand by gravity study. Songklanakarin journal of science and technology, 633-647.

Loke, M.H. 2000, Electrical imaging surveys for environmental and engineering studies.

Loke, M.H. 2012, Tutorial : 2-D and 3-D electrical imaging surveys.

Loke, M.H. 2015, Tutorial : 2-D and 3-D electrical imaging surveys.

Manzur, S.R., Hossain, M.S., Kemler, V., Khan, M.S. (2016). Monitoring extent of moisture variations due to leachate recirculation in an ELR/bioreactor landfill using resistivity imaging. Waste Management, 38-48.

Maurya, P.K., Rønde, V.K., Fiandaca, G., Balbarini, N., Auken, E., Bjerk, P.L., Christiansen, A.V. (2017). Detailed landfill leachate plume mapping using 2D and 3D electrical resistivity tomography - with correlation to ionic strength measured in screens. Applied Geophysics, 1-8.

Mohamaden, M.I.I., Ehab, D. (2017). Application of electrical resistivity for groundwater exploration in Wadi Rahaba, Shalateen, Egypt. Astronomy and Geophysics, 201-209.

Monroe, S.J., Wicander, R., Hazlett, R. 2007. Physical geology 6th ed., Thomson Brooke/Cole, California, U.S.A., pp 198-229.

Muchingami, I., Hlatywayo, D.J., Nel, J.M., Chuma, C. (2012). Electrical resistivity survey for groundwater investigations and shallow subsurface evaluation of the basaltic-greenstone formation of the urban Bulawayo aquifer. Physics and Chemistry of the Earth, 44-51.

Papadopoulos, N.G., Myeong-Jong, Y., Jung-Ho, K., Tsourlos, P., Tsokas, G.N. (2010). Geophysical investigation of tumuli by means of surface 3D Electrical Resistivity Tomography. Applied Geophysics, 192-205.

Park, S., Yi, M.J., Kim, J.H., Shin, S.W. (2016). Electrical resistivity imaging (ERI) monitoring for groundwater contamination in an uncontrolled landfill, South Korea. Applied Geophysics, 1-7.

Perrone, A., Lapenna, V., Piscitelli, S. (2014). Electrical resistivity tomography technique for landslide investigation: A review. Earth-Science Reviews, 65-83.

Pringle, J.K., Jervis, J.R., Hansen, J.D., Jones, G.M., Cassidy, N.J., Cassella, J.P. (2012). Geophysical Monitoring of Simulated Clandestine Graves Using Electrical and Ground-Penetrating Radar Methods: 0–3 Years after Burial. Forensic Sciences, 1467-1486.

Schön J (1996). Physical properties of rocks. Handbook of geophysical exploration. Vol 18. Pergamon, Oxford, New York

Sebastian, U., Paul, B.W., Jonathan, E.C., Hansruedi, M., Andrew, J.M., David, A.G., Philip, I.M. (2015). Interpolation of landslide movements to improve the accuracy of 4D geoelectrical monitoring. Applied Geophysics, 93-105.

Séger, M., Cousin, I., Frison, A., Boizard, H., Richard, G. (2009). Characterisation of the structural heterogeneity of the soil tilled layer by using in situ 2D and 3D electrical resistivity measurements. Soil & Tillage Research, 287-298.

Séger, M., Guérin, R., Frison, A., Bourennane, H., Richard, G., Richard, I. (2014). A 3D electrical resistivity tomography survey to characterise the structure of a albeluvic tonguing horizon composed of distinct elementary pedological volumes. Geoderma, 168-176.

Teerarungsikul, N., Chongariyakul, S. 2000. Geology map of Thiland 1: 50,000, Depart of mineral resources, Thailand

Tildy, P., Neducza, B., Nagy, P., Kanli, A.L., Hegymegi, C. (2017). Time lapse 3D geoelectric measurements for monitoring of in-situ remediation. Applied Geophysics, 99-113.

Travelletti, J., Malet, J.P. (2012). Charaterization of the 3D geometry of flow-like landslide: A methodology based on the integration of heterogeneous multi-source data. Engineering Geology, 30-48.

Wilkinson, W.B., Jonathan, C., Sebastian, U., Philip, M., Alister, S., Neil, D., Meng, H.L. (2016). Reconstruction of landslide movements by inversion of 4D electrical resistivity tomography monitoring data. American Geophysical Union.

Youssef, A.M., El-Kaliouby, H.M., Zabramawi, Y.A. (2012). Integration of remote sensing and electrical resistivity methods in sinkhole investigation in Saudi Arabia. Applied Geophysics, 28-39.

Zeyen, H., Pessel, M., Ledésert, B., Hébert, R., Bartier, D., Sabin, M., Lallemant, S. (2011). 3D electrical resistivity imaging of the near-surface structure of mud-volcano vents. Tectonophysics, 181-190.

APPENDIX

Appendix A
Raw data

C2		C1		P1		P2		Resistivity (Ohm-m)		
x	y	x	y	x	y	x	y	Area 1	Area 2	Area 3
0	0	3	0	6	0	9	0	4766.5	71.4	159.2
0	0	3	0	9	0	12	0	1330.0	50.9	110.8
0	0	3	0	12	0	15	0	1032.1	52.7	55.9
0	0	3	0	15	0	18	0	689.4	45.7	72.3
0	0	3	0	18	0	21	0	193.1	32.9	70.1
0	0	3	0	21	0	24	0	97.5	30.8	75.5
0	0	3	0	24	0	27	0	91.8	28.5	106.4
3	0	6	0	9	0	12	0	1705.0	88.5	143.3
3	0	6	0	12	0	15	0	1039.4	79.0	98.6
3	0	6	0	15	0	18	0	682.5	64.1	71.1
3	0	6	0	18	0	21	0	215.5	44.7	64.3
3	0	6	0	21	0	24	0	93.9	41.3	65.7
3	0	6	0	24	0	27	0	88.1	37.4	91.5
6	0	9	0	12	0	15	0	1123.7	101.7	155.0
6	0	9	0	15	0	18	0	640.4	72.7	97.2
6	0	9	0	18	0	21	0	176.7	48.8	79.8
6	0	9	0	21	0	24	0	85.2	42.6	75.4
6	0	9	0	24	0	27	0	80.8	38.1	105.4
9	0	12	0	15	0	18	0	1215.8	102.5	140.3
9	0	12	0	18	0	21	0	187.1	61.1	96.6
9	0	12	0	21	0	24	0	74.7	48.9	81.2
9	0	12	0	24	0	27	0	62.4	41.5	98.3
12	0	15	0	18	0	21	0	619.0	104.4	155.3
12	0	15	0	21	0	24	0	186.6	72.6	106.8
12	0	15	0	24	0	27	0	138.5	58.1	122.8
15	0	18	0	21	0	24	0	137.4	99.9	145.0
15	0	18	0	24	0	27	0	101.8	69.7	134.7
18	0	21	0	24	0	27	0	65.2	84.1	189.0
0	3	3	3	6	3	9	3	2575.5	108.6	132.5
0	3	3	3	9	3	12	3	1392.1	55.2	94.8
0	3	3	3	12	3	15	3	1193.0	59.5	95.5
0	3	3	3	15	3	18	3	627.6	54.0	80.3
0	3	3	3	18	3	21	3	191.2	44.2	74.0
0	3	3	3	21	3	24	3	83.6	38.1	61.3
0	3	3	3	24	3	27	3	84.8	33.6	100.3
3	3	6	3	9	3	12	3	1130.5	72.1	145.5
3	3	6	3	12	3	15	3	834.3	67.3	129.0
3	3	6	3	15	3	18	3	419.5	62.0	103.5

3	3	6	3	18	3	21	3	125.8	49.9	92.9
3	3	6	3	21	3	24	3	54.6	41.6	74.7
3	3	6	3	24	3	27	3	53.0	35.6	123.0
6	3	9	3	12	3	15	3	1132.9	103.4	150.4
6	3	9	3	15	3	18	3	446.3	80.3	116.9
6	3	9	3	18	3	21	3	116.0	62.4	102.7
6	3	9	3	21	3	24	3	51.9	51.1	80.8
6	3	9	3	24	3	27	3	47.7	42.9	126.3
9	3	12	3	15	3	18	3	2320.5	95.7	145.2
9	3	12	3	18	3	21	3	310.5	61.2	117.1
9	3	12	3	21	3	24	3	99.7	46.8	88.8
9	3	12	3	24	3	27	3	81.6	65.3	131.0
12	3	15	3	18	3	21	3	629.9	108.9	181.9
12	3	15	3	21	3	24	3	176.4	74.5	123.9
12	3	15	3	24	3	27	3	140.9	55.8	166.9
15	3	18	3	21	3	24	3	105.2	108.4	152.8
15	3	18	3	24	3	27	3	81.4	72.6	180.5
18	3	21	3	24	3	27	3	71.7	93.8	224.7
0	6	3	6	6	6	9	6	1273.7	110.7	118.9
0	6	3	6	9	6	12	6	787.0	59.4	114.3
0	6	3	6	12	6	15	6	782.7	55.2	77.6
0	6	3	6	15	6	18	6	417.5	54.3	83.4
0	6	3	6	18	6	21	6	205.7	50.1	63.5
0	6	3	6	21	6	24	6	35.5	42.9	64.3
0	6	3	6	24	6	27	6	45.7	35.3	118.3
3	6	6	6	9	6	12	6	914.0	79.5	199.5
3	6	6	6	12	6	15	6	591.5	69.5	119.8
3	6	6	6	15	6	18	6	295.2	65.6	120.8
3	6	6	6	18	6	21	6	142.0	60.8	91.6
3	6	6	6	21	6	24	6	22.2	51.7	93.1
3	6	6	6	24	6	27	6	29.3	42.7	162.5
6	6	9	6	12	6	15	6	2599.5	93.3	145.8
6	6	9	6	15	6	18	6	670.6	71.0	127.7
6	6	9	6	18	6	21	6	240.3	61.4	97.2
6	6	9	6	21	6	24	6	32.2	52.1	100.0
6	6	9	6	24	6	27	6	39.1	41.8	168.4
9	6	12	6	15	6	18	6	2091.9	84.2	220.2
9	6	12	6	18	6	21	6	554.3	63.1	153.0
9	6	12	6	21	6	24	6	58.0	50.0	155.3
9	6	12	6	24	6	27	6	58.2	39.3	243.3
12	6	15	6	18	6	21	6	1054.4	96.8	129.4
12	6	15	6	21	6	24	6	91.0	66.6	121.9
12	6	15	6	24	6	27	6	87.4	48.6	180.0

15	6	18	6	21	6	24	6	76.2	104.1	194.4
15	6	18	6	24	6	27	6	55.0	68.6	234.9
18	6	21	6	24	6	27	6	80.6	94.9	234.3
0	9	3	9	6	9	9	9	2533.1	99.6	165.5
0	9	3	9	9	9	12	9	620.0	24.1	155.4
0	9	3	9	12	9	15	9	486.5	53.8	114.0
0	9	3	9	15	9	18	9	294.9	46.8	95.0
0	9	3	9	18	9	21	9	89.7	50.1	77.9
0	9	3	9	21	9	24	9	32.7	41.4	61.2
0	9	3	9	24	9	27	9	40.2	31.9	148.1
3	9	6	9	9	9	12	9	2256.7	26.8	183.2
3	9	6	9	12	9	15	9	758.2	78.2	129.4
3	9	6	9	15	9	18	9	311.9	65.9	109.0
3	9	6	9	18	9	21	9	84.6	68.1	88.9
3	9	6	9	21	9	24	9	26.3	55.8	70.3
3	9	6	9	24	9	27	9	35.4	43.1	164.7
6	9	9	9	12	9	15	9	3894.7	18.5	266.8
6	9	9	9	15	9	18	9	989.6	30.5	204.3
6	9	9	9	18	9	21	9	211.4	37.5	168.0
6	9	9	9	21	9	24	9	54.7	26.8	124.1
6	9	9	9	24	9	27	9	51.2	21.3	283.1
9	9	12	9	15	9	18	9	2208.3	99.6	226.3
9	9	12	9	18	9	21	9	402.2	88.9	182.8
9	9	12	9	21	9	24	9	85.2	65.3	137.0
9	9	12	9	24	9	27	9	78.0	48.7	314.8
12	9	15	9	18	9	21	9	674.6	92.8	179.0
12	9	15	9	21	9	24	9	126.7	60.0	114.8
12	9	15	9	24	9	27	9	98.6	43.0	254.2
15	9	18	9	21	9	24	9	129.7	84.1	144.2
15	9	18	9	24	9	27	9	94.3	52.6	276.3
18	9	21	9	24	9	27	9	49.8	81.4	313.7
0	12	3	12	6	12	9	12	1605.1	85.0	233.4
0	12	3	12	9	12	12	12	793.9	72.4	203.8
0	12	3	12	12	12	15	12	507.4	65.9	126.4
0	12	3	12	15	12	18	12	276.0	55.5	106.0
0	12	3	12	18	12	21	12	47.4	50.3	74.4
0	12	3	12	21	12	24	12	44.2	45.5	58.8
0	12	3	12	24	12	27	12	45.8	42.1	157.5
3	12	6	12	9	12	12	12	1837.5	96.6	253.6
3	12	6	12	12	12	15	12	791.4	80.8	139.4
3	12	6	12	15	12	18	12	320.9	66.1	114.4
3	12	6	12	18	12	21	12	46.0	59.5	72.3
3	12	6	12	21	12	24	12	35.3	54.4	54.3

3	12	6	12	24	12	27	12	35.3	51.1	145.5
6	12	9	12	12	12	15	12	2719.2	88.5	428.8
6	12	9	12	15	12	18	12	909.2	61.3	337.7
6	12	9	12	18	12	21	12	111.9	51.4	181.1
6	12	9	12	21	12	24	12	75.8	45.8	119.7
6	12	9	12	24	12	27	12	74.5	42.5	339.3
9	12	12	12	15	12	18	12	1727.3	89.7	404.2
9	12	12	12	18	12	21	12	184.4	65.4	197.0
9	12	12	12	21	12	24	12	107.3	55.3	130.1
9	12	12	12	24	12	27	12	101.9	49.8	362.9
12	12	15	12	18	12	21	12	308.2	82.3	245.0
12	12	15	12	21	12	24	12	138.5	63.3	141.8
12	12	15	12	24	12	27	12	127.3	54.7	350.6
15	12	18	12	21	12	24	12	131.2	82.5	201.7
15	12	18	12	24	12	27	12	104.7	64.9	398.1
18	12	21	12	24	12	27	12	40.6	88.2	414.5
0	15	3	15	6	15	9	15	1189.5	107.7	208.5
0	15	3	15	9	15	12	15	670.8	100.9	203.8
0	15	3	15	12	15	15	15	453.4	85.6	216.7
0	15	3	15	15	15	18	15	236.3	73.0	164.0
0	15	3	15	18	15	21	15	39.0	61.3	125.3
0	15	3	15	21	15	24	15	54.3	57.9	93.4
0	15	3	15	24	15	27	15	54.4	569.2	102.7
3	15	6	15	9	15	12	15	853.3	120.8	313.1
3	15	6	15	12	15	15	15	450.3	96.4	301.7
3	15	6	15	15	15	18	15	209.9	81.9	224.9
3	15	6	15	18	15	21	15	31.9	68.6	164.3
3	15	6	15	21	15	24	15	42.2	65.9	111.6
3	15	6	15	24	15	27	15	40.9	66.0	119.6
6	15	9	15	12	15	15	15	1768.6	98.1	602.8
6	15	9	15	15	15	18	15	701.0	71.6	401.8
6	15	9	15	18	15	21	15	91.3	56.8	269.7
6	15	9	15	21	15	24	15	109.0	54.0	157.8
6	15	9	15	24	15	27	15	104.5	54.7	167.5
9	15	12	15	15	15	18	15	1203.0	107.0	416.6
9	15	12	15	18	15	21	15	140.6	73.1	234.1
9	15	12	15	21	15	24	15	153.7	64.0	151.4
9	15	12	15	24	15	27	15	147.1	63.6	164.0
12	15	15	15	18	15	21	15	188.1	91.4	370.4
12	15	15	15	21	15	24	15	168.6	66.0	237.6
12	15	15	15	24	15	27	15	109.6	61.3	236.2
15	15	18	15	21	15	24	15	137.9	88.7	271.5
15	15	18	15	24	15	27	15	114.6	69.3	263.4

18	15	21	15	24	15	27	15	46.6	105.9	539.0
0	18	3	18	6	18	9	18	903.1	218.2	260.7
0	18	3	18	9	18	12	18	537.3	128.8	248.8
0	18	3	18	12	18	15	18	357.9	123.7	239.8
0	18	3	18	15	18	18	18	139.4	107.4	192.6
0	18	3	18	18	18	21	18	48.3	83.3	196.4
0	18	3	18	21	18	24	18	67.7	78.9	241.6
0	18	3	18	24	18	27	18	66.7	63.2	201.2
3	18	6	18	9	18	12	18	936.8	156.0	275.8
3	18	6	18	12	18	15	18	394.4	137.4	254.7
3	18	6	18	15	18	18	18	142.0	118.3	210.6
3	18	6	18	18	18	21	18	48.3	92.2	216.1
3	18	6	18	21	18	24	18	66.6	87.5	265.6
3	18	6	18	24	18	27	18	63.8	70.2	221.9
6	18	9	18	12	18	15	18	1290.7	165.8	318.0
6	18	9	18	15	18	18	18	377.3	130.3	258.8
6	18	9	18	18	18	21	18	113.0	97.4	264.5
6	18	9	18	21	18	24	18	152.9	91.6	322.4
6	18	9	18	24	18	27	18	144.9	72.9	271.9
9	18	12	18	15	18	18	18	582.6	136.1	271.3
9	18	12	18	18	18	21	18	152.4	89.4	262.2
9	18	12	18	21	18	24	18	208.5	79.7	308.6
9	18	12	18	24	18	27	18	197.5	62.9	261.4
12	18	15	18	18	18	21	18	204.1	108.0	275.3
12	18	15	18	21	18	24	18	259.1	88.0	276.8
12	18	15	18	24	18	27	18	241.8	68.9	221.3
15	18	18	18	21	18	24	18	139.3	109.5	256.1
15	18	18	18	24	18	27	18	120.8	77.1	162.6
18	18	21	18	24	18	27	18	99.4	101.4	332.7
0	21	3	21	6	21	9	21	1010.5	408.0	264.5
0	21	3	21	9	21	12	21	426.4	311.5	265.2
0	21	3	21	12	21	15	21	261.8	234.9	255.4
0	21	3	21	15	21	18	21	103.7	151.0	210.8
0	21	3	21	18	21	21	21	74.0	109.7	165.3
0	21	3	21	21	21	24	21	64.3	99.9	234.5
0	21	3	21	24	21	27	21	74.1	89.7	247.2
3	21	6	21	9	21	12	21	1234.3	416.0	327.1
3	21	6	21	12	21	15	21	500.0	313.2	291.6
3	21	6	21	15	21	18	21	162.7	202.3	244.0
3	21	6	21	18	21	21	21	117.6	143.9	194.8
3	21	6	21	21	21	24	21	97.3	130.7	279.9
3	21	6	21	24	21	27	21	103.5	115.9	298.4
6	21	9	21	12	21	15	21	1166.0	275.5	301.5

6	21	9	21	15	21	18	21	296.1	169.2	248.2
6	21	9	21	18	21	21	21	205.3	119.1	198.8
6	21	9	21	21	21	24	21	162.9	108.2	291.0
6	21	9	21	24	21	27	21	173.8	96.4	317.4
9	21	12	21	15	21	18	21	410.8	223.5	268.6
9	21	12	21	18	21	21	21	266.8	135.4	200.1
9	21	12	21	21	21	24	21	211.0	120.1	300.2
9	21	12	21	24	21	27	21	221.2	106.7	339.1
12	21	15	21	18	21	21	21	391.7	163.1	173.3
12	21	15	21	21	21	24	21	293.9	136.4	238.9
12	21	15	21	24	21	27	21	298.8	121.4	280.6
15	21	18	21	21	21	24	21	224.2	146.1	202.7
15	21	18	21	24	21	27	21	197.7	119.3	228.5
18	21	21	21	24	21	27	21	355.2	128.6	246.2
0	24	3	24	6	24	9	24	1131.2	1025.5	377.6
0	24	3	24	9	24	12	24	471.9	568.2	404.9
0	24	3	24	12	24	15	24	253.4	315.7	299.4
0	24	3	24	15	24	18	24	149.7	189.2	189.2
0	24	3	24	18	24	21	24	151.6	158.3	154.4
0	24	3	24	21	24	24	24	105.6	114.2	237.2
0	24	3	24	24	24	27	24	78.5	106.0	204.2
3	24	6	24	9	24	12	24	1265.5	817.8	513.8
3	24	6	24	12	24	15	24	532.8	431.9	329.4
3	24	6	24	15	24	18	24	294.7	239.9	193.8
3	24	6	24	18	24	21	24	278.8	196.8	155.4
3	24	6	24	21	24	24	24	197.6	145.6	240.6
3	24	6	24	24	24	27	24	149.2	143.4	213.3
6	24	9	24	12	24	15	24	775.6	598.8	426.3
6	24	9	24	15	24	18	24	378.9	301.5	206.2
6	24	9	24	18	24	21	24	319.8	227.6	152.2
6	24	9	24	21	24	24	24	223.2	153.2	244.9
6	24	9	24	24	24	27	24	170.3	141.9	216.9
9	24	12	24	15	24	18	24	515.5	453.4	445.3
9	24	12	24	18	24	21	24	352.7	322.0	254.0
9	24	12	24	21	24	24	24	237.4	202.0	351.8
9	24	12	24	24	24	27	24	191.8	178.3	312.3
12	24	15	24	18	24	21	24	456.1	354.8	322.5
12	24	15	24	21	24	24	24	251.2	216.2	329.2
12	24	15	24	24	24	27	24	174.0	186.7	289.4
15	24	18	24	21	24	24	24	770.4	235.5	255.3
15	24	18	24	24	24	27	24	293.9	193.8	202.1
18	24	21	24	24	24	27	24	1166.3	256.9	204.9
0	27	3	27	6	27	9	27	1478.3	1720.4	466.2

0	27	3	27	9	27	12	27	560.9	711.3	262.8
0	27	3	27	12	27	15	27	334.8	549.9	379.9
0	27	3	27	15	27	18	27	121.6	344.4	263.9
0	27	3	27	18	27	21	27	219.5	228.1	255.2
0	27	3	27	21	27	24	27	232.6	180.7	170.0
0	27	3	27	24	27	27	27	175.3	104.7	173.7
3	27	6	27	9	27	12	27	1009.1	1615.5	531.8
3	27	6	27	12	27	15	27	547.9	955.3	378.5
3	27	6	27	15	27	18	27	187.8	575.6	225.4
3	27	6	27	18	27	21	27	327.3	364.5	200.9
3	27	6	27	21	27	24	27	345.7	283.1	165.9
3	27	6	27	24	27	27	27	250.8	156.5	179.7
6	27	9	27	12	27	15	27	770.1	1451.9	751.7
6	27	9	27	15	27	18	27	236.8	800.2	283.8
6	27	9	27	18	27	21	27	405.5	464.0	240.1
6	27	9	27	21	27	24	27	430.2	334.2	161.0
6	27	9	27	24	27	27	27	299.3	194.2	167.2
9	27	12	27	15	27	18	27	299.2	661.8	912.1
9	27	12	27	18	27	21	27	472.5	385.7	458.7
9	27	12	27	21	27	24	27	511.5	282.4	266.9
9	27	12	27	24	27	27	27	340.8	171.8	265.3
12	27	15	27	18	27	21	27	1051.6	640.7	665.2
12	27	15	27	21	27	24	27	1089.3	398.7	371.6
12	27	15	27	24	27	27	27	628.8	250.0	372.5
15	27	18	27	21	27	24	27	912.8	770.9	395.6
15	27	18	27	24	27	27	27	515.5	370.7	303.2
18	27	21	27	24	27	27	27	2103.1	586.2	433.3
0	0	0	3	0	6	0	9	2695.0	62.1	141.9
0	0	0	3	0	9	0	12	1753.1	55.0	103.2
0	0	0	3	0	12	0	15	1357.0	45.7	114.0
0	0	0	3	0	15	0	18	697.8	48.1	76.9
0	0	0	3	0	18	0	21	565.0	44.7	69.0
0	0	0	3	0	21	0	24	404.9	92.8	54.8
0	0	0	3	0	24	0	27	379.1	223.1	196.1
0	3	0	6	0	9	0	12	1909.4	71.6	153.2
0	3	0	6	0	12	0	15	1382.5	56.2	139.3
0	3	0	6	0	15	0	18	700.7	58.0	87.8
0	3	0	6	0	18	0	21	563.8	54.5	77.6
0	3	0	6	0	21	0	24	406.3	113.2	59.8
0	3	0	6	0	24	0	27	368.5	275.4	209.6
0	6	0	9	0	12	0	15	1546.8	63.0	152.3
0	6	0	9	0	15	0	18	632.9	51.5	84.2
0	6	0	9	0	18	0	21	471.2	45.4	71.8

0	6	0	9	0	21	0	24	329.2	87.3	54.3
0	6	0	9	0	24	0	27	297.5	219.2	185.6
0	9	0	12	0	15	0	18	1264.9	82.6	154.1
0	9	0	12	0	18	0	21	850.1	60.4	110.7
0	9	0	12	0	21	0	24	587.8	96.3	74.9
0	9	0	12	0	24	0	27	548.2	241.6	238.6
0	12	0	15	0	18	0	21	1024.1	98.5	258.1
0	12	0	15	0	21	0	24	614.8	110.4	155.5
0	12	0	15	0	24	0	27	561.4	269.6	451.2
0	15	0	18	0	21	0	24	644.9	194.8	175.9
0	15	0	18	0	24	0	27	516.6	432.0	408.2
0	18	0	21	0	24	0	27	597.7	730.5	448.2
3	0	3	3	3	6	3	9	1747.9	71.6	157.8
3	0	3	3	3	9	3	12	1314.7	44.9	99.0
3	0	3	3	3	12	3	15	766.0	40.9	155.8
3	0	3	3	3	15	3	18	575.1	35.9	88.8
3	0	3	3	3	18	3	21	550.7	39.9	92.7
3	0	3	3	3	21	3	24	410.1	74.4	58.1
3	0	3	3	3	24	3	27	374.6	162.8	208.9
3	3	3	6	3	9	3	12	1033.9	102.8	133.2
3	3	3	6	3	12	3	15	549.4	77.7	131.7
3	3	3	6	3	15	3	18	412.8	62.4	95.8
3	3	3	6	3	18	3	21	390.0	64.2	103.4
3	3	3	6	3	21	3	24	252.4	113.2	60.6
3	3	3	6	3	24	3	27	272.8	241.6	209.9
3	6	3	9	3	12	3	15	1134.0	90.9	177.3
3	6	3	9	3	15	3	18	557.7	60.4	120.5
3	6	3	9	3	18	3	21	484.4	59.2	131.4
3	6	3	9	3	21	3	24	340.8	91.3	73.5
3	6	3	9	3	24	3	27	329.4	192.3	246.4
3	9	3	12	3	15	3	18	935.6	80.6	169.3
3	9	3	12	3	18	3	21	764.7	69.3	168.2
3	9	3	12	3	21	3	24	528.1	94.2	90.2
3	9	3	12	3	24	3	27	521.7	187.4	289.0
3	12	3	15	3	18	3	21	673.1	130.6	293.1
3	12	3	15	3	21	3	24	252.8	144.7	143.8
3	12	3	15	3	24	3	27	352.3	263.7	434.8
3	15	3	18	3	21	3	24	556.9	267.3	117.4
3	15	3	18	3	24	3	27	357.5	410.0	379.5
3	18	3	21	3	24	3	27	783.6	797.7	539.9
6	0	6	3	6	6	6	9	1326.6	97.0	125.0
6	0	6	3	6	9	6	12	948.8	63.9	108.2
6	0	6	3	6	12	6	15	549.9	50.7	120.3

6	0	6	3	6	15	6	18	443.1	43.8	82.9
6	0	6	3	6	18	6	21	404.9	56.2	90.5
6	0	6	3	6	21	6	24	358.2	57.0	62.7
6	0	6	3	6	24	6	27	251.2	234.7	160.1
6	3	6	6	6	9	6	12	1250.4	91.1	186.4
6	3	6	6	6	12	6	15	379.9	63.4	173.0
6	3	6	6	6	15	6	18	279.9	50.1	119.9
6	3	6	6	6	18	6	21	255.9	63.0	126.7
6	3	6	6	6	21	6	24	229.1	59.7	83.2
6	3	6	6	6	24	6	27	160.1	237.4	205.5
6	6	6	9	6	12	6	15	1842.9	89.6	189.2
6	6	6	9	6	15	6	18	661.8	62.7	135.2
6	6	6	9	6	18	6	21	458.2	76.1	142.5
6	6	6	9	6	21	6	24	386.5	67.8	91.2
6	6	6	9	6	24	6	27	266.7	257.2	218.5
6	9	6	12	6	15	6	18	1267.2	78.0	247.3
6	9	6	12	6	18	6	21	664.6	87.8	242.2
6	9	6	12	6	21	6	24	531.3	57.1	152.8
6	9	6	12	6	24	6	27	365.1	256.0	316.1
6	12	6	15	6	18	6	21	705.0	131.4	365.5
6	12	6	15	6	21	6	24	447.5	94.7	224.6
6	12	6	15	6	24	6	27	286.2	307.5	463.9
6	15	6	18	6	21	6	24	803.7	195.2	180.4
6	15	6	18	6	24	6	27	356.6	507.5	314.8
6	18	6	21	6	24	6	27	1193.0	1039.6	483.6
9	0	9	3	9	6	9	9	1071.8	83.0	131.6
9	0	9	3	9	9	9	12	714.1	66.0	109.1
9	0	9	3	9	12	9	15	412.6	61.4	204.5
9	0	9	3	9	15	9	18	344.2	49.2	40.4
9	0	9	3	9	18	9	21	288.8	49.1	70.7
9	0	9	3	9	21	9	24	224.4	51.1	56.2
9	0	9	3	9	24	9	27	145.2	236.7	161.5
9	3	9	6	9	9	9	12	2819.5	86.7	191.8
9	3	9	6	9	12	9	15	637.5	71.4	278.4
9	3	9	6	9	15	9	18	349.1	60.5	53.2
9	3	9	6	9	18	9	21	252.4	53.8	88.8
9	3	9	6	9	21	9	24	176.0	52.8	66.1
9	3	9	6	9	24	9	27	115.7	235.5	188.3
9	6	9	9	9	12	9	15	2770.9	90.2	507.5
9	6	9	9	9	15	9	18	976.9	64.7	77.0
9	6	9	9	9	18	9	21	470.2	58.4	122.5
9	6	9	9	9	21	9	24	283.7	55.3	89.8
9	6	9	9	9	24	9	27	166.9	235.4	236.4

9	9	9	12	9	15	9	18	2244.8	79.7	150.8
9	9	9	12	9	18	9	21	855.6	66.7	183.9
9	9	9	12	9	21	9	24	433.8	60.1	119.2
9	9	9	12	9	24	9	27	238.6	243.6	292.3
9	12	9	15	9	18	9	21	1290.2	107.6	740.2
9	12	9	15	9	21	9	24	516.3	86.8	397.1
9	12	9	15	9	24	9	27	227.0	320.7	898.2
9	15	9	18	9	21	9	24	1235.3	147.3	139.4
9	15	9	18	9	24	9	27	407.3	450.5	254.4
9	18	9	21	9	24	9	27	1000.3	789.5	559.8
12	0	12	3	12	6	12	9	2034.2	79.5	129.6
12	0	12	3	12	9	12	12	769.1	66.2	100.7
12	0	12	3	12	12	12	15	321.4	59.8	267.1
12	0	12	3	12	15	12	18	228.5	42.8	51.9
12	0	12	3	12	18	12	21	133.0	42.7	76.7
12	0	12	3	12	21	12	24	107.4	51.3	65.3
12	0	12	3	12	24	12	27	89.5	171.3	192.7
12	3	12	6	12	9	12	12	2688.1	89.1	169.3
12	3	12	6	12	12	12	15	694.5	67.2	372.8
12	3	12	6	12	15	12	18	355.3	45.8	66.1
12	3	12	6	12	18	12	21	172.8	43.7	100.5
12	3	12	6	12	21	12	24	123.9	48.7	79.7
12	3	12	6	12	24	12	27	97.7	164.8	239.6
12	6	12	9	12	12	12	15	2183.4	90.3	502.2
12	6	12	9	12	15	12	18	869.3	53.0	94.8
12	6	12	9	12	18	12	21	340.4	46.5	126.6
12	6	12	9	12	21	12	24	202.0	51.7	90.1
12	6	12	9	12	24	12	27	140.7	164.5	254.3
12	9	12	12	12	15	12	18	2086.6	82.8	158.3
12	9	12	12	12	18	12	21	720.6	60.7	191.6
12	9	12	12	12	21	12	24	373.4	63.3	116.9
12	9	12	12	12	24	12	27	219.7	182.5	324.2
12	12	12	15	12	18	12	21	1016.8	113.4	765.0
12	12	12	15	12	21	12	24	471.2	101.6	427.9
12	12	12	15	12	24	12	27	236.4	259.8	1079.7
12	15	12	18	12	21	12	24	705.9	140.7	130.7
12	15	12	18	12	24	12	27	368.0	295.0	276.0
12	18	12	21	12	24	12	27	739.9	564.6	591.9
15	0	15	3	15	6	15	9	1580.6	99.4	153.2
15	0	15	3	15	9	15	12	581.0	71.8	126.0
15	0	15	3	15	12	15	15	233.2	66.0	294.9
15	0	15	3	15	15	15	18	99.7	50.7	149.8
15	0	15	3	15	18	15	21	55.9	48.1	109.7

15	0	15	3	15	21	15	24	104.1	56.7	85.5
15	0	15	3	15	24	15	27	93.2	109.9	194.5
15	3	15	6	15	9	15	12	1490.6	99.3	156.0
15	3	15	6	15	12	15	15	523.4	75.6	310.0
15	3	15	6	15	15	15	18	192.6	54.8	153.6
15	3	15	6	15	18	15	21	76.5	49.4	109.1
15	3	15	6	15	21	15	24	108.2	55.7	84.6
15	3	15	6	15	24	15	27	109.1	103.3	192.5
15	6	15	9	15	12	15	15	1334.6	89.4	390.3
15	6	15	9	15	15	15	18	415.6	59.1	174.0
15	6	15	9	15	18	15	21	139.8	49.2	117.2
15	6	15	9	15	21	15	24	172.4	54.9	38.4
15	6	15	9	15	24	15	27	147.2	100.1	203.8
15	9	15	12	15	15	15	18	909.0	80.3	256.3
15	9	15	12	15	18	15	21	244.1	59.0	128.1
15	9	15	12	15	21	15	24	224.1	60.0	94.5
15	9	15	12	15	24	15	27	193.3	101.1	213.9
15	12	15	15	15	18	15	21	390.1	105.4	461.3
15	12	15	15	15	21	15	24	252.6	95.0	289.3
15	12	15	15	15	24	15	27	221.7	142.3	626.7
15	15	15	18	15	21	15	24	405.5	144.2	158.9
15	15	15	18	15	24	15	27	287.2	176.8	288.3
15	18	15	21	15	24	15	27	446.8	300.6	355.4
18	0	18	3	18	6	18	9	427.9	113.8	146.9
18	0	18	3	18	9	18	12	139.1	67.9	139.5
18	0	18	3	18	12	18	15	46.6	57.4	187.3
18	0	18	3	18	15	18	18	35.8	52.3	254.2
18	0	18	3	18	18	18	21	30.6	39.6	143.7
18	0	18	3	18	21	18	24	101.5	45.7	102.9
18	0	18	3	18	24	18	27	98.3	92.0	170.8
18	3	18	6	18	9	18	12	423.6	89.9	184.1
18	3	18	6	18	12	18	15	111.3	66.7	212.6
18	3	18	6	18	15	18	18	71.2	57.9	291.9
18	3	18	6	18	18	18	21	55.9	42.0	167.6
18	3	18	6	18	21	18	24	180.8	46.7	120.6
18	3	18	6	18	24	18	27	176.6	91.4	201.6
18	6	18	9	18	12	18	15	196.9	99.7	232.9
18	6	18	9	18	15	18	18	113.4	73.5	267.5
18	6	18	9	18	18	18	21	92.5	49.4	159.1
18	6	18	9	18	21	18	24	300.1	54.4	111.1
18	6	18	9	18	24	18	27	289.9	100.8	185.5
18	9	18	12	18	15	18	18	161.5	82.3	368.8
18	9	18	12	18	18	18	21	88.7	48.0	216.1

18	9	18	12	18	21	18	24	266.4	50.6	145.3
18	9	18	12	18	24	18	27	262.7	87.5	237.6
18	12	18	15	18	18	18	21	86.3	78.1	287.3
18	12	18	15	18	21	18	24	224.6	72.1	183.4
18	12	18	15	18	24	18	27	228.5	116.8	299.1
18	15	18	18	18	21	18	24	259.7	130.3	201.7
18	15	18	18	18	24	18	27	267.9	175.6	303.2
18	18	18	21	18	24	18	27	371.3	210.6	222.0
21	0	21	3	21	6	21	9	80.7	94.4	140.2
21	0	21	3	21	9	21	12	52.2	67.3	154.7
21	0	21	3	21	12	21	15	43.9	54.0	171.3
21	0	21	3	21	15	21	18	46.8	44.7	322.6
21	0	21	3	21	18	21	21	41.3	36.3	154.8
21	0	21	3	21	21	21	24	1290.8	38.5	97.1
21	0	21	3	21	24	21	27	192.1	98.8	144.8
21	3	21	6	21	9	21	12	105.4	106.7	222.4
21	3	21	6	21	12	21	15	78.4	70.5	219.2
21	3	21	6	21	15	21	18	83.1	56.3	427.7
21	3	21	6	21	18	21	21	74.5	44.1	213.1
21	3	21	6	21	21	21	24	227.4	46.0	132.6
21	3	21	6	21	24	21	27	347.1	113.7	201.5
21	6	21	9	21	12	21	15	62.1	89.6	182.6
21	6	21	9	21	15	21	18	61.4	60.5	346.7
21	6	21	9	21	18	21	21	56.4	45.3	168.8
21	6	21	9	21	21	21	24	169.2	45.1	104.4
21	6	21	9	21	24	21	27	257.2	106.9	155.9
21	9	21	12	21	15	21	18	66.8	77.2	449.9
21	9	21	12	21	18	21	21	58.6	52.3	207.7
21	9	21	12	21	21	21	24	170.2	48.9	120.6
21	9	21	12	21	24	21	27	261.1	108.3	181.6
21	12	21	15	21	18	21	21	64.2	93.0	399.3
21	12	21	15	21	21	21	24	157.8	76.8	145.8
21	12	21	15	21	24	21	27	244.1	149.5	188.3
21	15	21	18	21	21	21	24	218.5	116.1	307.5
21	15	21	18	21	24	21	27	327.9	181.8	366.5
21	18	21	21	21	24	21	27	562.3	194.2	231.3
24	0	24	3	24	6	24	9	64.8	97.4	271.6
24	0	24	3	24	9	24	12	56.5	62.5	180.4
24	0	24	3	24	12	24	15	46.4	63.8	258.3
24	0	24	3	24	15	24	18	51.6	45.4	256.2
24	0	24	3	24	18	24	21	52.9	43.1	174.7
24	0	24	3	24	21	24	24	117.5	39.7	117.4
24	0	24	3	24	24	24	27	235.2	91.4	122.3

24	3	24	6	24	9	24	12	66.5	84.1	289.1
24	3	24	6	24	12	24	15	52.3	77.0	364.1
24	3	24	6	24	15	24	18	58.1	53.4	364.7
24	3	24	6	24	18	24	21	60.2	49.2	258.9
24	3	24	6	24	21	24	24	135.1	45.2	172.0
24	3	24	6	24	24	24	27	276.4	102.3	181.2
24	6	24	9	24	12	24	15	58.7	97.8	401.9
24	6	24	9	24	15	24	18	52.3	60.7	343.7
24	6	24	9	24	18	24	21	50.5	55.4	251.9
24	6	24	9	24	21	24	24	107.3	49.4	163.0
24	6	24	9	24	24	24	27	225.6	106.0	172.7
24	9	24	12	24	15	24	18	84.1	81.6	314.2
24	9	24	12	24	18	24	21	64.7	63.0	213.5
24	9	24	12	24	21	24	24	115.4	51.6	128.5
24	9	24	12	24	24	24	27	243.0	105.8	135.5
24	12	24	15	24	18	24	21	105.9	123.4	593.1
24	12	24	15	24	21	24	24	130.5	87.7	263.7
24	12	24	15	24	24	24	27	270.7	154.7	250.8
24	15	24	18	24	21	24	24	241.9	104.9	344.1
24	15	24	18	24	24	24	27	466.8	143.1	276.4
24	18	24	21	24	24	24	27	848.1	184.7	279.9
27	0	27	3	27	6	27	9	64.3	104.3	868.1
27	0	27	3	27	9	27	12	44.7	61.9	437.5
27	0	27	3	27	12	27	15	37.1	75.1	393.1
27	0	27	3	27	15	27	18	38.2	61.7	315.4
27	0	27	3	27	18	27	21	44.7	44.8	280.8
27	0	27	3	27	21	27	24	103.3	52.1	201.1
27	0	27	3	27	24	27	27	155.0	112.9	197.1
27	3	27	6	27	9	27	12	98.5	79.9	865.5
27	3	27	6	27	12	27	15	69.2	81.5	616.5
27	3	27	6	27	15	27	18	64.5	66.2	470.8
27	3	27	6	27	18	27	21	72.6	56.0	417.3
27	3	27	6	27	21	27	24	157.9	54.4	291.2
27	3	27	6	27	24	27	27	232.3	114.2	276.8
27	6	27	9	27	12	27	15	79.0	115.0	735.6
27	6	27	9	27	15	27	18	63.9	83.0	536.7
27	6	27	9	27	18	27	21	61.2	68.6	475.5
27	6	27	9	27	21	27	24	118.3	57.5	328.9
27	6	27	9	27	24	27	27	173.1	133.3	302.3
27	9	27	12	27	15	27	18	96.2	91.9	525.7
27	9	27	12	27	18	27	21	80.6	70.3	456.3
27	9	27	12	27	21	27	24	132.6	65.3	311.7
27	9	27	12	27	24	27	27	186.6	126.8	273.0

27	12	27	15	27	18	27	21	149.1	112.9	611.0
27	12	27	15	27	21	27	24	187.1	94.3	401.2
27	12	27	15	27	24	27	27	244.3	170.9	345.2
27	15	27	18	27	21	27	24	366.3	110.2	346.0
27	15	27	18	27	24	27	27	429.2	155.5	276.3
27	18	27	21	27	24	27	27	809.4	185.8	295.2
9	0	6	3	3	6	0	9	1747.7	125.1	163.2
12	0	9	3	6	6	3	9	1491.3	109.2	195.4
12	0	9	3	3	9	0	12	1099.0	60.1	138.2
9	3	6	6	3	9	0	12	1242.6	104.0	201.7
15	0	12	3	9	6	6	9	1623.2	119.5	217.0
15	0	12	3	6	9	3	12	919.7	94.8	163.5
15	0	12	3	3	12	0	15	571.2	66.6	164.4
12	3	9	6	6	9	3	12	1506.3	117.8	237.8
12	3	9	6	3	12	0	15	540.5	71.3	213.0
9	6	6	9	3	12	0	15	1301.5	113.2	286.8
18	0	15	3	12	6	9	9	1549.5	93.1	250.1
18	0	15	3	9	9	6	12	641.7	92.8	232.5
18	0	15	3	6	12	3	15	314.4	79.9	158.0
18	0	15	3	3	15	0	18	232.5	74.2	119.4
15	3	12	6	9	9	6	12	2910.6	139.0	268.4
15	3	12	6	6	12	3	15	744.9	95.7	170.3
15	3	12	6	3	15	0	18	516.1	82.5	120.9
12	6	9	9	6	12	3	15	1696.4	107.0	333.5
12	6	9	9	3	15	0	18	545.9	84.3	207.2
9	9	6	12	3	15	0	18	1216.9	125.3	304.1
21	0	18	3	15	6	12	9	614.4	117.2	202.2
21	0	18	3	12	9	9	12	259.3	88.8	231.4
21	0	18	3	9	12	6	15	131.0	64.7	285.0
21	0	18	3	6	15	3	18	75.6	68.9	106.9
21	0	18	3	3	18	0	21	78.5	85.1	115.2
18	3	15	6	12	9	9	12	1843.9	135.1	311.3
18	3	15	6	9	12	6	15	601.8	83.4	369.3
18	3	15	6	6	15	3	18	260.9	83.0	119.7
18	3	15	6	3	18	0	21	258.1	99.4	123.9
15	6	12	9	9	12	6	15	2831.2	95.9	533.0
15	6	12	9	6	15	3	18	610.0	84.5	139.5
15	6	12	9	3	18	0	21	496.0	95.9	136.4
12	9	9	12	6	15	3	18	1300.7	138.7	259.2
12	9	9	12	3	18	0	21	683.1	143.4	233.9
9	12	6	15	3	18	0	21	967.4	187.4	465.1
24	0	21	3	18	6	15	9	167.5	150.8	228.5
24	0	21	3	15	9	12	12	151.4	80.5	190.0

24	0	21	3	12	12	9	15	91.6	69.4	369.6
24	0	21	3	9	15	6	18	73.4	50.8	123.9
24	0	21	3	6	18	3	21	56.6	82.9	139.7
24	0	21	3	3	21	0	24	47.5	102.2	106.1
21	3	18	6	15	9	12	12	804.1	110.7	236.6
21	3	18	6	12	12	9	15	3271.0	83.0	439.9
21	3	18	6	9	15	6	18	163.5	57.7	140.2
21	3	18	6	6	18	3	21	122.9	90.5	150.5
21	3	18	6	3	21	0	24	94.8	112.8	117.2
18	6	15	9	12	12	9	15	1524.7	121.3	564.2
18	6	15	9	9	15	6	18	537.6	72.2	119.2
18	6	15	9	6	18	3	21	278.6	106.7	132.5
18	6	15	9	3	21	0	24	198.8	129.2	92.2
15	9	12	12	9	15	6	18	2229.1	101.2	190.0
15	9	12	12	6	18	3	21	693.2	125.5	181.4
15	9	12	12	3	21	0	24	424.1	143.6	129.5
12	12	9	15	6	18	3	21	1026.1	194.6	724.8
12	12	9	15	3	21	0	24	495.6	198.1	471.7
9	15	6	18	3	21	0	24	679.0	362.1	212.5
27	0	24	3	21	6	18	9	125.5	142.4	305.5
27	0	24	3	18	9	15	12	145.7	87.0	290.9
27	0	24	3	15	12	12	15	160.3	69.8	527.9
27	0	24	3	12	15	9	18	139.0	53.5	203.6
27	0	24	3	9	18	6	21	110.1	71.3	229.3
27	0	24	3	6	21	3	24	85.2	120.7	199.7
27	0	24	3	3	24	0	27	70.5	174.5	289.6
24	3	21	6	18	9	15	12	174.8	121.9	303.3
24	3	21	6	15	12	12	15	164.7	81.0	474.6
24	3	21	6	12	15	9	18	136.8	59.2	198.4
24	3	21	6	9	18	6	21	103.2	73.6	218.3
24	3	21	6	6	21	3	24	76.7	124.5	194.5
24	3	21	6	3	24	0	27	63.6	185.0	230.1
21	6	18	9	15	12	12	15	565.3	121.0	464.2
21	6	18	9	12	15	9	18	253.4	78.6	146.6
21	6	18	9	9	18	6	21	147.8	88.7	159.6
21	6	18	9	6	21	3	24	107.6	146.2	138.2
21	6	18	9	3	24	0	27	91.5	213.3	169.4
18	9	15	12	12	15	9	18	1487.1	104.9	174.6
18	9	15	12	9	18	6	21	570.5	94.9	173.6
18	9	15	12	6	21	3	24	294.8	146.8	131.2
18	9	15	12	3	24	0	27	228.8	209.1	185.7
15	12	12	15	9	18	6	21	1468.9	162.6	914.2
15	12	12	15	6	21	3	24	533.9	213.4	628.2

15	12	12	15	3	24	0	27	374.9	285.4	734.5
12	15	9	18	6	21	3	24	1011.1	314.2	241.9
12	15	9	18	3	24	0	27	472.3	375.8	363.9
9	18	6	21	3	24	0	27	949.6	985.7	609.5
27	3	24	6	21	9	18	12	109.4	127.2	497.5
27	3	24	6	18	12	15	15	188.9	78.9	645.8
27	3	24	6	15	15	12	18	206.1	61.4	468.0
27	3	24	6	12	18	9	21	196.4	66.5	403.6
27	3	24	6	9	21	6	24	149.2	94.6	398.4
27	3	24	6	6	24	3	27	112.2	203.3	453.2
24	6	21	9	18	12	15	15	184.0	103.2	341.5
24	6	21	9	15	15	12	18	175.8	73.1	244.2
24	6	21	9	12	18	9	21	165.5	76.9	207.8
24	6	21	9	9	21	6	24	125.1	105.4	206.5
24	6	21	9	6	24	3	27	93.5	213.5	217.4
21	9	18	12	15	15	12	18	309.9	106.8	328.0
21	9	18	12	12	18	9	21	217.3	89.5	246.9
21	9	18	12	9	21	6	24	147.5	113.5	244.3
21	9	18	12	6	24	3	27	108.7	262.6	250.1
18	12	15	15	12	18	9	21	1079.8	153.5	670.1
18	12	15	15	9	21	6	24	479.6	157.8	531.2
18	12	15	15	6	24	3	27	284.8	312.2	580.0
15	15	12	18	9	21	6	24	1102.0	232.4	363.7
15	15	12	18	6	24	3	27	460.8	436.2	472.5
12	18	9	21	6	24	3	27	1220.2	1027.0	619.1
27	6	24	9	21	12	18	15	81.5	123.9	516.3
27	6	24	9	18	15	15	18	147.3	81.9	530.0
27	6	24	9	15	18	12	21	243.3	72.6	302.5
27	6	24	9	12	21	9	24	192.4	92.0	336.6
27	6	24	9	9	24	6	27	124.2	231.8	392.0
24	9	21	12	18	15	15	18	161.1	104.3	393.0
24	9	21	12	15	18	12	21	255.4	81.0	233.9
24	9	21	12	12	21	9	24	119.4	95.2	268.3
24	9	21	12	9	24	6	27	134.9	242.7	269.1
21	12	18	15	15	18	12	21	296.4	128.9	419.9
21	12	18	15	12	21	9	24	238.8	129.2	426.9
21	12	18	15	9	24	6	27	152.5	287.8	461.7
18	15	15	18	12	21	9	24	590.4	216.9	414.8
18	15	15	18	9	24	6	27	299.3	401.7	529.0
15	18	12	21	9	24	6	27	925.5	816.5	583.5
27	9	24	12	21	15	18	18	90.5	103.8	682.1
27	9	24	12	18	18	15	21	177.4	81.7	247.0
27	9	24	12	15	21	12	24	342.7	86.0	230.2

27	9	24	12	12	24	9	27	204.1	214.0	427.0
24	12	21	15	18	18	15	21	181.3	139.5	210.0
24	12	21	15	15	21	12	24	360.5	124.5	258.6
24	12	21	15	12	24	9	27	221.3	268.1	462.4
21	15	18	18	15	21	12	24	415.8	176.5	439.3
21	15	18	18	12	24	9	27	260.8	308.0	777.5
18	18	15	21	12	24	9	27	598.7	608.4	540.8
27	12	24	15	21	18	18	21	139.9	134.5	371.2
27	12	24	15	18	21	15	24	372.6	129.8	210.8
27	12	24	15	15	24	12	27	236.2	230.4	504.1
24	15	21	18	18	21	15	24	399.2	180.9	397.9
24	15	21	18	15	24	12	27	255.6	280.3	831.4
21	18	18	21	15	24	12	27	349.9	377.4	487.5
27	15	24	18	21	21	18	24	450.9	158.1	384.5
27	15	24	18	18	24	15	27	372.2	225.9	433.3
24	18	21	21	18	24	15	27	408.7	304.3	397.8
27	18	24	21	21	24	18	27	1123.5	293.9	351.4
18	0	21	3	24	6	27	9	104.0	129.9	417.3
15	0	18	3	21	6	24	9	109.0	149.0	224.2
15	0	18	3	24	9	27	12	111.0	82.3	379.2
18	3	21	6	24	9	27	12	156.0	107.9	468.0
12	0	15	3	18	6	21	9	895.6	156.0	203.7
12	0	15	3	21	9	24	12	121.1	66.9	205.1
12	0	15	3	24	12	27	15	131.2	78.2	438.6
15	3	18	6	21	9	24	12	116.8	90.3	282.0
15	3	18	6	24	12	27	15	112.9	89.9	547.6
18	6	21	9	24	12	27	15	136.8	162.3	543.3
9	0	12	3	15	6	18	9	1288.3	124.4	210.4
9	0	12	3	18	9	21	12	199.4	87.9	182.9
9	0	12	3	21	12	24	15	49.3	67.7	244.5
9	0	12	3	24	15	27	18	73.2	73.0	272.6
12	3	15	6	18	9	21	12	707.4	120.3	247.5
12	3	15	6	21	12	24	15	124.1	79.3	314.3
12	3	15	6	24	15	27	18	162.7	79.6	367.5
15	6	18	9	21	12	24	15	155.1	111.0	360.8
15	6	18	9	24	15	27	18	193.3	94.3	437.2
18	9	21	12	24	15	27	18	127.8	130.4	548.6
6	0	9	3	12	6	15	9	1299.0	145.3	190.9
6	0	9	3	15	9	18	12	410.0	93.9	192.5
6	0	9	3	18	12	21	15	58.9	80.3	177.1
6	0	9	3	21	15	24	18	48.4	76.8	261.0
6	0	9	3	24	18	27	21	89.5	73.3	174.1
9	3	12	6	15	9	18	12	1258.8	87.1	309.0

9	3	12	6	18	12	21	15	110.9	69.4	264.4
9	3	12	6	21	15	24	18	66.0	66.2	375.6
9	3	12	6	24	18	27	21	108.4	60.3	244.4
12	6	15	9	18	12	21	15	378.1	129.0	315.3
12	6	15	9	21	15	24	18	167.4	98.7	384.2
12	6	15	9	24	18	27	21	253.9	85.3	259.4
15	9	18	12	21	15	24	18	185.9	112.0	537.6
15	9	18	12	24	18	27	21	254.7	81.9	345.5
18	12	21	15	24	18	27	21	139.2	124.6	501.9
3	0	6	3	9	6	12	9	1607.1	112.4	193.8
3	0	6	3	12	9	15	12	1042.2	84.5	145.4
3	0	6	3	15	12	18	15	388.5	76.2	203.2
3	0	6	3	18	15	21	18	57.9	68.2	159.3
3	0	6	3	21	18	24	21	93.6	64.6	143.8
3	0	6	3	24	21	27	24	253.0	80.2	136.7
6	3	9	6	12	9	15	12	1821.4	112.9	229.9
6	3	9	6	15	12	18	15	312.4	90.5	273.8
6	3	9	6	18	15	21	18	36.2	77.2	189.8
6	3	9	6	21	18	24	21	48.3	73.1	166.3
6	3	9	6	24	21	27	24	123.9	90.0	157.4
9	6	12	9	15	12	18	15	1270.8	123.9	516.3
9	6	12	9	18	15	21	18	100.5	89.2	322.5
9	6	12	9	21	18	24	21	109.1	78.7	262.5
9	6	12	9	24	21	27	24	275.2	94.0	242.7
12	9	15	12	18	15	21	18	241.8	111.3	377.7
12	9	15	12	21	18	24	21	204.8	84.2	274.3
12	9	15	12	24	21	27	24	503.3	97.7	249.7
15	12	18	15	21	18	24	21	188.3	120.8	434.3
15	12	18	15	24	21	27	24	419.9	123.2	375.6
18	15	21	18	24	21	27	24	319.4	190.9	444.3
0	0	3	3	6	6	9	9	2522.5	118.3	180.0
0	0	3	3	9	9	12	12	1364.8	80.4	328.2
0	0	3	3	12	12	15	15	969.1	71.9	208.6
0	0	3	3	15	15	18	18	354.6	64.5	148.5
0	0	3	3	18	18	21	21	85.8	57.2	122.0
0	0	3	3	21	21	24	24	214.7	70.5	146.9
0	0	3	3	24	24	27	27	390.1	124.6	163.5
3	3	6	6	9	9	12	12	888.5	132.8	237.5
3	3	6	6	12	12	15	15	452.5	103.8	263.3
3	3	6	6	15	15	18	18	159.5	87.7	121.2
3	3	6	6	18	18	21	21	37.2	76.4	125.5
3	3	6	6	21	21	24	24	88.1	94.0	148.3
3	3	6	6	24	24	27	27	175.3	162.8	167.0

6	6	9	9	12	12	15	15	2682.4	117.0	525.5
6	6	9	9	15	15	18	18	443.3	85.5	190.0
6	6	9	9	18	18	21	21	69.9	71.6	170.3
6	6	9	9	21	21	24	24	147.3	87.9	192.4
6	6	9	9	24	24	27	27	254.5	149.0	218.5
9	9	12	12	15	15	18	18	1149.0	119.1	347.4
9	9	12	12	18	18	21	21	136.3	84.9	244.4
9	9	12	12	21	21	24	24	257.8	101.1	269.7
9	9	12	12	24	24	27	27	389.0	168.0	309.7
12	12	15	15	18	18	21	21	232.1	125.0	556.3
12	12	15	15	21	21	24	24	399.9	131.9	571.4
12	12	15	15	24	24	27	27	611.6	202.4	627.7
15	15	18	18	21	21	24	24	329.6	195.8	366.3
15	15	18	18	24	24	27	27	464.5	266.3	377.6
18	18	21	21	24	24	27	27	737.2	299.6	353.2
0	3	3	6	6	9	9	12	1600.7	111.4	201.7
0	3	3	6	9	12	12	15	802.7	99.4	234.6
0	3	3	6	12	15	15	18	597.3	86.8	113.5
0	3	3	6	15	18	18	21	135.7	90.5	110.5
0	3	3	6	18	21	21	24	141.2	82.9	101.0
0	3	3	6	21	24	24	27	227.7	132.5	166.3
3	6	6	9	9	12	12	15	1263.2	136.9	346.2
3	6	6	9	12	15	15	18	490.0	103.7	128.1
3	6	6	9	15	18	18	21	97.6	102.4	123.7
3	6	6	9	18	21	21	24	73.0	94.1	112.6
3	6	6	9	21	24	24	27	104.9	151.5	188.2
6	9	9	12	12	15	15	18	2180.3	115.4	249.9
6	9	9	12	15	18	18	21	273.1	103.6	214.5
6	9	9	12	18	21	21	24	197.6	92.1	179.6
6	9	9	12	21	24	24	27	246.9	138.0	309.2
9	12	12	15	15	18	18	21	500.0	159.9	693.2
9	12	12	15	18	21	21	24	314.8	128.2	494.2
9	12	12	15	21	24	24	27	525.2	183.5	825.3
12	15	15	18	18	21	21	24	115.5	186.0	258.2
12	15	15	18	21	24	24	27	1123.4	233.6	426.1
15	18	18	21	21	24	24	27	561.6	335.3	424.3
0	6	3	9	6	12	9	15	1319.6	106.7	308.3
0	6	3	9	9	15	12	18	612.3	111.0	164.1
0	6	3	9	12	18	15	21	370.1	90.5	160.4
0	6	3	9	15	21	18	24	89.6	91.5	139.6
0	6	3	9	18	24	21	27	119.3	126.2	166.1
3	9	6	12	9	15	12	18	1475.3	165.5	252.1
3	9	6	12	12	18	15	21	561.2	123.8	231.5

3	9	6	12	15	21	18	24	107.3	125.3	197.4
3	9	6	12	18	24	21	27	127.4	169.9	229.7
6	12	9	15	12	18	15	21	1328.8	139.0	750.9
6	12	9	15	15	21	18	24	214.4	133.8	538.7
6	12	9	15	18	24	21	27	237.8	167.1	618.9
9	15	12	18	15	21	18	24	395.6	246.7	299.8
9	15	12	18	18	24	21	27	388.8	268.8	373.8
12	18	15	21	18	24	21	27	648.2	406.8	395.6
0	9	3	12	6	15	9	18	1401.2	140.8	295.2
0	9	3	12	9	18	12	21	822.2	111.6	270.9
0	9	3	12	12	21	15	24	423.9	136.9	234.6
0	9	3	12	15	24	18	27	146.2	134.6	247.5
3	12	6	15	9	18	12	21	862.8	152.7	509.8
3	12	6	15	12	21	15	24	349.3	179.0	410.9
3	12	6	15	15	24	18	27	120.7	173.7	435.4
6	15	9	18	12	21	15	24	1048.1	318.1	383.7
6	15	9	18	15	24	18	27	270.3	281.6	481.5
9	18	12	21	15	24	18	27	525.3	476.3	552.4
0	12	3	15	6	18	9	21	929.0	166.8	389.0
0	12	3	15	9	21	12	24	536.6	158.6	357.3
0	12	3	15	12	24	15	27	271.6	199.5	487.0
3	15	6	18	9	21	12	24	787.5	340.8	380.8
3	15	6	18	12	24	15	27	279.7	395.1	548.0
6	18	9	21	12	24	15	27	918.1	723.8	680.6
0	15	3	18	6	21	9	24	779.7	348.2	307.9
0	15	3	18	9	24	12	27	359.5	499.1	634.0
3	18	6	21	9	24	12	27	1040.9	1143.9	832.4
0	18	3	21	6	24	9	27	830.0	1024.6	686.2

Appendix B
Publication

E3S Web of Conferences **34**, 01007 (2018) https://doi.org/10.1051/e3sconf/20183401007
CENVIRON 2017

3D resistivity survey for shallow subsurface fault investigations

Kraipat Petrit[1], *Poonnapa* Klamthim[1], and *Helmut* Duerrast[1,2,*]

[1]Geophysics Research Center, Prince of Songkla University, 90112 Hatyai, Songkhla, Thailand
[2]Dept. of Physics, Fac. of Science, Prince of Songkla University, 90112 Hatyai, Songkhla, Thailand

Abstract. The shallow subsurface is subject to various human activities, and the place of occurrence of geohazards, e.g. shallow active faults. The identification of the location and orientation of such faults can be vital for infrastructure development. The aim of this study was to develop a low-cost 3D resistivity survey system, with reasonable survey time for shallow fault investigations. The study area in Songkhla Province, Thailand is located in an old quarry where faults could be identified in outcrops. The study area was designed to cover the expected fault with 100 electrodes arranged in a 10×10 square grid with an electrode spacing of 3 meters in x and y axis. Each electrode in turn was used as a current and potential electrode using a dipole-dipole array. Field data have been processed and interpreted using 3DResINV. Results, presented in horizontal depth slices and vertical xz- and yz-cross sections, revealed through differences in resistivity down to 8 m depths a complex structural setting with two shallow faults and dipping sedimentary rock layers. In conclusion, this study has shown that a 3D resistivity survey can imagine complex tectonic structures, thus providing a far more insight into the shallow subsurface.

1 Introduction

The shallow subsurface, the first few hundred meters below the Earth's surface, is subject to various human activities, e.g., building foundations, groundwater drilling, but also the place of occurrence of potential geohazards, e.g., landslides and shallow active faults. The identification of the location and orientation of shallow faults can be vital for infrastructure development, thus mitigating the impact of potential earthquakes. Various types of geophysical methods can be used to identify and locate faults in the shallow subsurface, e.g. 2D resistivity, seismic reflection, and ground penetrating radar; however these techniques produce only a 2D cross section of the subsurface. In order to get more information about a more complex subsurface either several 2D surveys have to be conducted or real 3D ones. Among the latter ones is the 3D resistivity method. It is a relatively fast and easy method to do in comparison to a real 3D seismic reflection survey, which is commonly applied in petroleum exploration and deeper depths.

* Corresponding author: helmut.j@psu.ac.th

E3S Web of Conferences **34**, 01007 (2018) https://doi.org/10.1051/e3sconf/20183401007
CENVIRON 2017

The objective of this work is to develop a fully functioning system for 3D resistivity measurements using the available technology at the department and then testing the system and subsequent data processing and interpretation for a study site where the subsurface structures were known from geological field observations.

2 Theories

2.1 Resistivity of rock and material

Resistivity of a material is defined as the resistance in ohms between the opposite face of a unit cube of material. For a cylinder of resistance δR, length δL, and cross-section area δA, the resistivity ρ is given by equation 1 with resistivity is ohm-meter [1].

$$\rho = (\delta R \delta A)/\delta L \quad (1)$$

Resistivity is one of the physical properties with the largest variation (Fig. 1). Metallic minerals in igneous rocks, for example, conduct electrical currents by their free electrons. For porous sediments and sedimentary rocks, which make up most of the shallow subsurface, the electrical current is carried by ions in the pore fluid; thus the resistivity of shallow subsurface materials depend mainly on the type of pore fluid, saturation, and porosity. This process is called electrolytic conductivity. Resistivity for this kind of material is defined by equation 2, Archie's law [1, 2],

$$\rho = (a\, \rho_w)/(S_w^n\, \emptyset^m) \quad (2)$$

where a is a constant, ρ_w is the resistivity of the pore fluid, S_w is the water saturation, n is saturation exponent, $\emptyset$ is the porosity, and m is the cementation exponent.

For clay material the situation is different as their surface is electrical charged resulting in colloidal conductivity. Therefore, resistivity values for clay are usually very low (see Fig. 1).

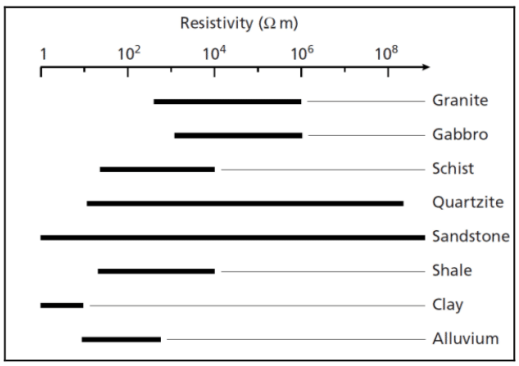

Fig. 1. Resistivity range of some common rock and sediment types, after [2].

Porosity is one of the most important rock properties in describing porous media. It is defined as the ratio of pore volume to bulk volume of a rock sample. This factor is a dimensionless quantity, expressed either in decimal or percentage. Fluid inside the pores of the shallow subsurface is mainly water and air [3]. The permeability of a rock is a measure

E3S Web of Conferences **34**, 01007 (2018) https://doi.org/10.1051/e3sconf/20183401007
CENVIRON 2017

of the ease with which the rock will permit the passage of fluids. If fluid passes through the rock easily, it has high permeability, and opposite.

2.2 Resistivity survey

Resistivity survey is one type of geophysics method wildly used for shallow subsurface investigations. Here, a source current is injected into the subsurface via two electrodes, with the resulting potential of the subsurface measured by two other electrodes [2]. Measured values of this method are 'apparent resistivity' values, which are calculated from the current, potential, and distance arrangement of the electrodes as shown in equation 3 [2],

$$\rho_a = k(\Delta V/I) = kR \tag{3}$$

where ρ_a is the apparent resistivity, R is the resistance measured with a resistivity meter and k is the geometric factor, which depends on the overall arrangement and distance of the four current and potential electrodes.

A 3D resistivity survey is used to study the resistivity distribution in three dimensions; x, y and z (depth) dimension. Generally, electrodes are set on the ground surface of the study area in a rectangular or square grid. All electrodes are connected to a resistivity meter and also used to inject electrical current as well as to measure the potential [4].

2.3 Inversion method

Inversion method is used to estimate a possible physical model of the subsurface structure from the observed data. In this case, the observed data are apparent resistivity values from field survey and the model parameter are 'true' resistivity values of the subsurface. 3DResINV is available resistivity inversion software, which is used in this work. Inversion routine is based on the smoothness-constrained least-square method shown in equation 4. Procedures of this software make rectangular blocks where the model resistivity values are allowed to vary in all three directions; then try to reduce the difference between calculated data and measured apparent resistivity values by adjusting the resistivity of the model blocks. A measure of this difference is given by the root-mean-square (RMS) error [4, 5].

$$(J^TJ + \lambda F)\, \Delta\, \boldsymbol{q_k} = J^Tg - \lambda F\, \boldsymbol{q_k} \tag{4}$$

where J is the Jacobian matrix of the partial derivative, J^T is the transpose of J, λ is a damping factor, q_k is the model perturbation vector, g is a misfit data, and F is a roughness filter.

3 Field survey

3.1 Study area

The study area was in an old quarry located in the northern part of Sadao district, Songkhla province, Southern Thailand (Fig. 2a). The northern part is a flat area because rocks and soils have been taken out. In the southern part still remained the part of a hill and sediment layer can be seen from cliffs marking the quarry boundary. All formations in the quarry are sedimentary rocks with conglomerates, conglomeratic sandstone, and sandstone. In some parts of the area sandstone interbedded with siltstone occurred (Fig. 2b and 3).

E3S Web of Conferences **34**, 01007 (2018) https://doi.org/10.1051/e3sconf/20183401007
CENVIRON 2017

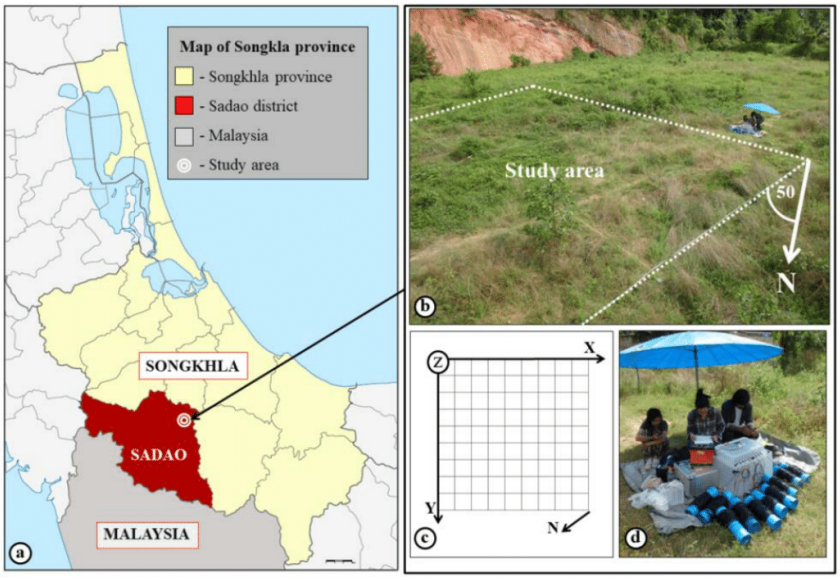

Fig. 2. Study area: (a) Location of study area in northern part of Sadao district, Songkhla province, southern Thailand, (b) Boundaries of the survey area with the direction of the x-axis 50 degrees from north over west, (c) Square grid of 10×10 electrodes with x-, y- and z-direction, and (d) Equipment set up consisting of resistivity meter, 12 V battery, switch box, and cable assembly.

3.2 Structural geology

Structural geological surface investigations in the study area revealed dipping sedimentary layers and faults (Fig. 3). Fig. 3d shows sediment layers dipping into north-west direction (288, dip direction) with dip angles of 15-20 degrees. The upper layer is conglomerate and the lower layer is sandstone and siltstone. Fig. 3a and 3e show a fault that can be found in this area. Measurements of the fault plane show that the fault is dipping into south direction with a dip angle of 64 degrees (dip direction/dip angle, 222/64).

3.3 Data acquisition and processing

To prove that 3D resistivity survey can be used to determine the structure of the subsurface, the study area is designed to cover the expected fault line show in Fig. 3. From Fig. 2b and 2c, the study area is a square grid of x- and y-axis. Direction of x-axis is 50 degree from north over west. Fig. 4 shows that 100 electrodes are set in a square grid with an inline spacing of 3 m for both x- and y-axis. Therefore, the size of the study area is 10×10 electrodes with 27×27 m (Fig. 4c).

Electrode configuration used to determine resistivity values in this work is dipole-dipole array; it consists of one of current electrode pair and one of potential electrode pair, show in Fig. 4b. From the 10×10 square of electrodes, 840 values of apparent resistivity have been measured from all directions; 10 lines in x-direction, 10 lines in y-direction, and 26 lines in both diagonal directions.

E3S Web of Conferences **34**, 01007 (2018) https://doi.org/10.1051/e3sconf/20183401007
CENVIRON 2017

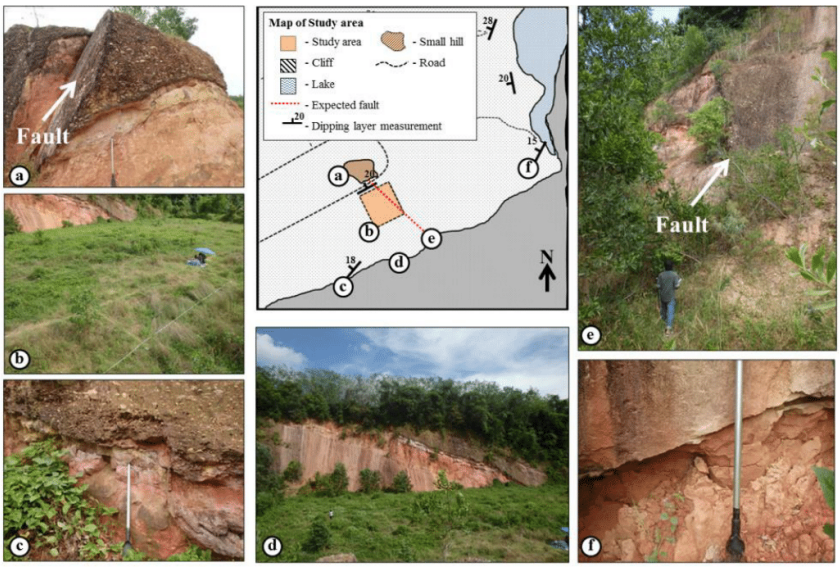

Fig. 3. Structural geology of study area (a) Fault, looking into NW, dip direction/dip angle of the fault plane is 222/64 and of the sedimentary layering 333/20, (b) Study area, looking into SE, (c) Sedimentary layer in the quarry nearby the study area, looking into SE, and measurement of sedimentary layering is 310/18, (d) Sedimentary layering seen at the cliff locate in the southern part of the study area, (e) Fault, looking into SE, with an orientation of 222/64, and (f) Sedimentary layering near the study area, looking into NW; measurement of layering plane gives 288/15.

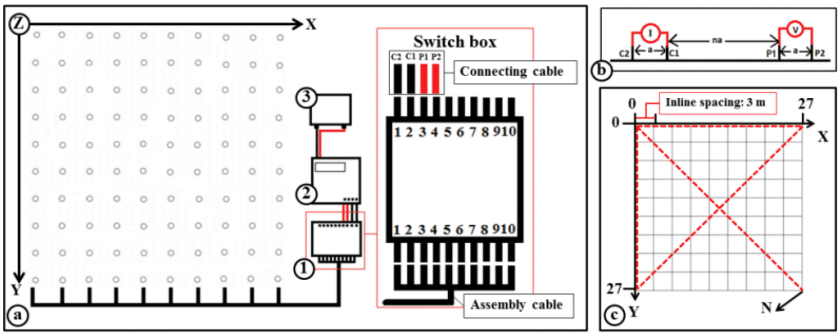

Fig. 4. Survey design and equipment: (a) Diagram of equipment set up consisting of 100 electrodes arranged in a 10×10 square grid, cable, switch box (1), resistivity meter (2) and 12 V battery (3), (b) Arrangement of electrodes in dipole-dipole array, C1-C2 is current electrode pair, P1-P2 is potential electrode pair, a is 3 m inline spacing and n is the ratio varied from 1 to 7 for 10 nodes of electrodes, and (c) Measurement lines, x, y, and both diagonal directions.

Equipment used to measure the apparent resistivity values is a Terrameter SAS 1000, single-channel resistivity meter. The main difference from a multi-channel resistivity meter that is actually used for a 3D resistivity survey is the limitation of a single-channel. Therefore, the resistivity meter cannot measure more than one data point at the same time

E3S Web of Conferences **34**, 01007 (2018) https://doi.org/10.1051/e3sconf/20183401007
CENVIRON 2017

of injecting current. In this work, a switch box was developed to use with a single-channel resistivity meter. Fig. 4a shows a diagram of the equipment set up with 10 electrodes in one line connected to the switch box by a cable assembly. The switch box is connected to the single-channel resistivity meter by two pairs of cables; a current cable pair and a potential cable pair. By this way, all data points in one line can be measured by moving the current cable pair and the potential cable pair on the switch box.

After data acquisition, the 3DResINV software processes the apparent resistivity values. Results from the software are images of resistivity distribution in horizontal sections (*xy* plane), x-sections (*xz* plane), and y-sections (*yz* plane).

4 Results and discussions

Fig. 5 and 6 present the inversion results of the resistivity model of the study area. From these results resistivity areas can be separated in two zones: A low resistivity (L) area with resistivity values varying from 10 to 2,000 ohm m, indicated by blue and green colors; and a higher resistivity area (H) that has a resistivity range of 2,000 to 5,000 ohm m, indicated by red and purple colors.

Including the geological information, low resistivity area can be considered to be siltstone and sandstone, whereas the high resistivity areas can be considered to be conglomerate. As the porosity and permeability of the conglomerate is lower than siltstone and sandstone, the resistivity of the conglomerate is higher than of the siltstone and sandstone.

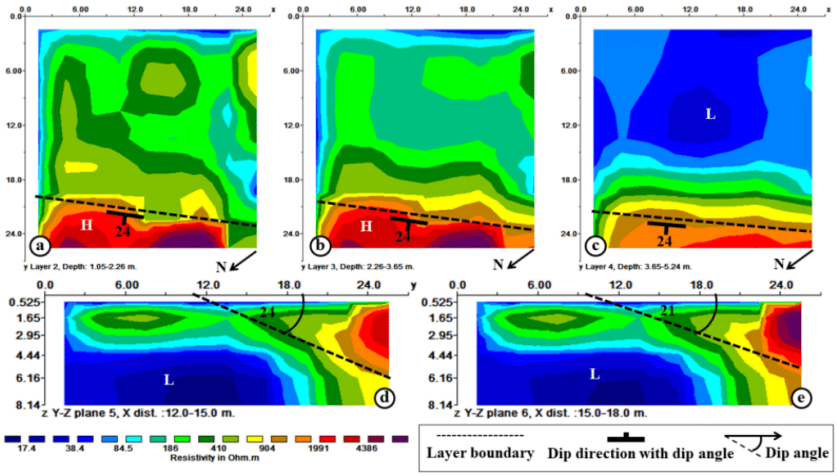

Fig. 5. Structural geology discussion, sedimentary layering: (a), (b), and (c), results of resistivity model in horizontal section of difference depth intervals with an interpretation of dip direction of the sedimentary layers, and (d) and (e) results of resistivity model in y-section with interpretation of dip angle of the layers. L = low resistivity, H = high resistivity.

E3S Web of Conferences **34**, 01007 (2018) https://doi.org/10.1051/e3sconf/20183401007
CENVIRON 2017

4.1 Dipping sedimentary layers

Fig. 5a-c presents the resistivity models of the horizontal sections for different depth intervals. Results show that layers of higher resistivity indicated to be conglomerate layers dipping into northwest direction, 225-230 degrees from north. From Fig. 5d and 5e, the dip angle is 20-25 degrees from the surface.

4.2 Faults

The consideration of fault lines in this area is based on discontinuity of resistivity values. As faults are cracks in the subsurface that can separate sedimentary layers they create discontinuities in the resistivity values. Fig. 6 shows that there are two fault lines in the study area; Fault 1 dipping into south direction, with a dip direction of 210 degrees from north and a dip angle of 68 degrees. Fault 2 is dipping in south direction with a dip direction of 215-220 degrees from north and a dip angle of 74 degrees.

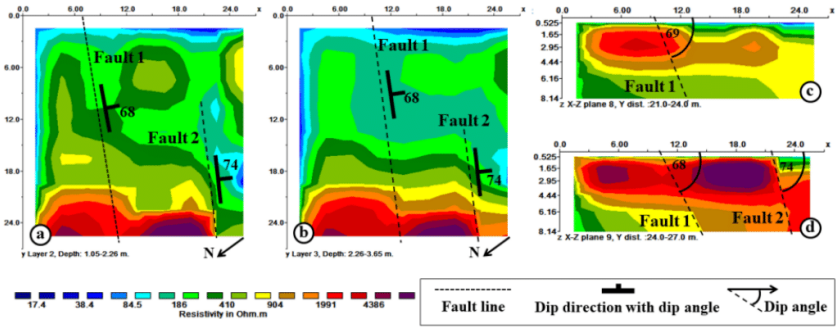

Fig. 6. Structural geology discussion, faults: (a) and (b) results of resistivity model in horizontal section with interpretation of dip direction of faults, and (c) and (d) results of resistivity model in x-section with interpretation of dip angle of the faults. L = low resistivity, H = high resistivity.

5 Conclusions

5.1 Subsurface model

From the resistivity survey, the result shows that the sedimentary layers dipping into northwest direction with a dip angle 20-25 degrees. Information of dipping sedimentary layers correlates with the geology data (see Fig. 3). The upper layer with higher resistivity should be conglomerate and the lower layer with lower resistivity should be siltstone and sandstone, as shown in Fig. 7.

From geological data, Fault 1 correlates with the expected fault line because both have similar dip direction and dip angle. From the results Fault 2 cannot be seen and identified from the surface. Detecting Fault 2 proves that a 3D resistivity survey can be used to determine geological structures in the subsurface that cannot be seen from surface investigations.

E3S Web of Conferences **34**, 01007 (2018) https://doi.org/10.1051/e3sconf/20183401007
CENVIRON 2017

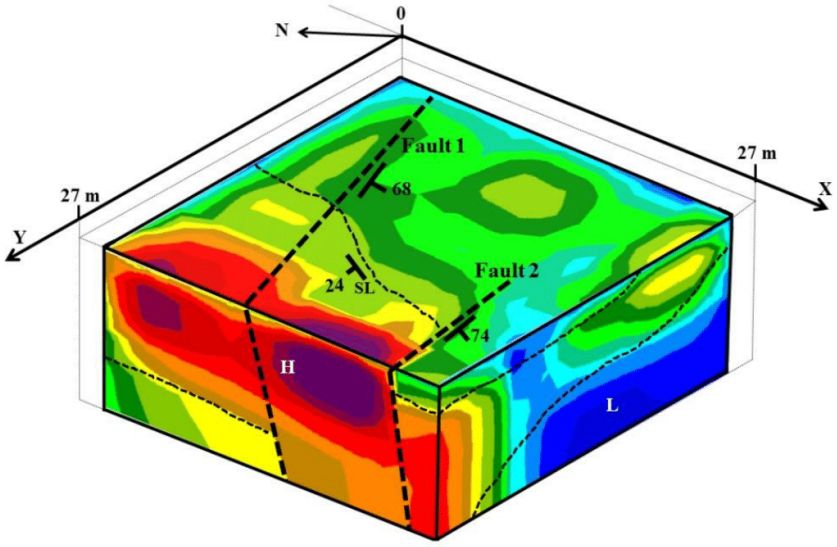

Fig. 7. Subsurface model from 3D resistivity survey: Fault information; Fault 1 is dipping into south direction with 68 degrees dip angle and Fault 2 is dipping into south direction with 74 degrees dip angle. Sedimentary layering (SL) shows dipping into northwest direction with a dip angle of 24 degrees. L = low resistivity, H = high resistivity.

5.2 Acquisition system

Conclusion also can be drawn regarding the 3D resistivity acquisition system. Results presented here show that it is possible to make a 3D resistivity survey by using a single-channel resistivity meter with a switch box and cable assembly instead of a multi-channel resistivity meter that still requires high survey costs nowadays. From this work, the data acquisition system can measure 840 data points in one to two days depending on survey area environment and the survey costs are actually lower than using a multi-channel resistivity meter.

References

1. P. Kearey, M. Brooks, I. Hill, *Introduction to Geophysical Exploration*, 3rd ed. (Blackwell Science Ltd, Oxford, 2002)
2. W.M. Telford, L.P. Geldart, R.E. Sheriff, *Applied Geophysics*, 2nd ed. (Cambridge University Press, New York, 1990)
3. R. Bowen, *Groundwater*, 2nd ed. (Elsevier Applied Science Publisher, Essex, 1986)
4. M.H. Loke, Tutorial: 2-D and 3-D electrical imaging surveys (2015)
5. M.K. Sen, P.L. Stoffa, *Globle Optimization Methods in Geophysics Inversion*, 2nd ed. (Cambridge University Press, New York, 2013)

VITAE

Name Mr. Kraipat Petrit
Student ID 5810220022
Educational Attainment

Degree	Name of Institution	Year of Graduation
Bachelor of Science (Physics)	Prince of Songkla University	2014

Scholarship Awards during Enrolment

2011-Present	Science Achievement Scholarship of Thailand
2015-2018	Teaching Assistant of department of physics, the Faculty of Science, Prince of Songkla University

List of Publication and Proceeding

Petrit, K., Klamtim, P. and Duerrast, H., 2017. 3D resistivity survey for shallow subsurface fault investigations. Proceeding of CENVIRON 2017 International Conference on Civil & Environmental Engineering (University of Malaysia Perlis), 28-29 NOV 2017, Penang, Malaysia, 1-8.

Phalakarn, M., Petrit, K., Ngansom, W. and Dürrast, H. (2016). Geoscientific Investigations of Geothermal Systems Case Study Khlongthom, Krabi. Proceeding of the 12th Conference on Energy Network of Thailand, Phitsanulok, Thailand, 1263-1268.